

University of Nebraska - Lincoln

DigitalCommons@University of Nebraska - Lincoln

Theses, Dissertations, and Student Research from
Electrical & Computer Engineering

Electrical & Computer Engineering, Department of

Spring 5-2015

Generalized Ellipsometry Analysis of Anisotropic Nanoporous Media: Polymer-infiltrated Nanocolumnar and Inverse-column Polymeric Films

Dan Liang

University of Nebraska-Lincoln, liangdan1984@gmail.com

Follow this and additional works at: <http://digitalcommons.unl.edu/elecengtheses>

 Part of the [Nanoscience and Nanotechnology Commons](#), [Other Electrical and Computer Engineering Commons](#), and the [Semiconductor and Optical Materials Commons](#)

Liang, Dan, "Generalized Ellipsometry Analysis of Anisotropic Nanoporous Media: Polymer-infiltrated Nanocolumnar and Inverse-column Polymeric Films" (2015). *Theses, Dissertations, and Student Research from Electrical & Computer Engineering*. 61.
<http://digitalcommons.unl.edu/elecengtheses/61>

This Article is brought to you for free and open access by the Electrical & Computer Engineering, Department of at DigitalCommons@University of Nebraska - Lincoln. It has been accepted for inclusion in Theses, Dissertations, and Student Research from Electrical & Computer Engineering by an authorized administrator of DigitalCommons@University of Nebraska - Lincoln.

GENERALIZED ELLIPSOmetry ANALYSIS OF ANISOTROPIC
NANOPOROUS MEDIA: POLYMER-INFILTRATED NANOCOLUMNAR
AND INVERSE-COLUMN POLYMERIC FILMS

by

Dan Liang

A DISSERTATION

Presented to the Faculty of

The Graduate College at the University of Nebraska

In Partial Fulfillment of Requirements

For the Degree of Doctor of Philosophy

Major: Electrical Engineering

Under the Supervision of Professor Eva Schubert

Lincoln, Nebraska

May, 2015

GENERALIZED ELLIPSOMETRY ANALYSIS OF ANISOTROPIC
NANOPOROUS MEDIA: POLYMER-INFILTRATED NANOCOLUMNAR
AND INVERSE-COLUMN POLYMERIC FILMS

Dan Liang, Ph.D.

University of Nebraska, 2015

Advisor: Eva Schubert

Characterization of the structural and optical properties is a subject of significance for nanoporous material research. However, it remains a challenge to find non-destructive methods for investigating the anisotropy of porous thin films with three-dimensional nanostructures. In this thesis, a generalized ellipsometry (GE) analysis approach is employed to study two types of anisotropic nanoporous media: slanted columnar thin films (SCTFs) with polymer infiltration and inverse-SCTF polymeric films. The thesis presents the physical properties obtained from GE analysis, including porosity, columnar shape, principal optical constants, birefringence, *etc.*

The thesis reports on using a GE analysis approach, combining the homogeneous biaxial layer approach (HBLA) and anisotropic Bruggeman effective medium approximation (AB-EMA), to determine the changes in structural and optical properties of highly porous SCTFs upon polymer infiltration. Via spin-coating, poly(-methyl methacrylate) (PMMA) was infiltrated into the permalloy SCTFs prepared by glancing angle deposition (GLAD). The Mueller matrix GE measurements were conducted on the SCTFs before and after PMMA infiltration. The obtained film thickness and columnar slanting angle show changes due to infiltration which are in good agreement with scanning electron microscopy (SEM) analysis. The method effectively identifies the changes in birefringence and dichroism upon infiltration, and provides constituent fractions consistent with the performed experiments.

GE analysis is further utilized to characterize the biaxial optical responses of the porous polymer thin films. The porous polymer films with inverse columnar structure (PMMA iSCTFs) were prepared via infiltrating polymer into the voids

of the SCTF templates and selectively removing the columns. The AB-EMA was employed to analyze the GE data of the porous polymer films and SCTF templates to determine the structural and anisotropic optical properties. The structural parameters are highly consistent with SEM results. The classification and structure of optical anisotropy are found to be identical for the samples. Our GE results demonstrate that the anisotropic optical behaviors for the two complementary structures follow the reciprocity principle in electrodynamics.

ACKNOWLEDGMENTS

First of all, I am deeply grateful to my adviser Dr. Eva Schubert for supporting and advising me during my study at UNL. I would like to thank her for the discussion and suggestion on my research work. With her kind help and wise advise, I am able to make progress in my research work, improve and finish this PhD thesis.

Secondly, I would like to give special thanks to Dr. Jinsong Huang, Dr. Mathias Schubert and Dr. Paul Snyder for serving on my doctorate supervisory committee. Especially, I would like to express my gratitude to Dr. Mathias Schubert for his valuable suggestion during my research work.

Thirdly, I would like to thank all my colleagues in this wonderful group for not only the valuable suggestions on my research, but also the precious time we spent together.

Last but not least, I would like to thank my parents and grandparents in China for their love, encouragement and support all the time.

Contents

Abstract	ii
Acknowledgements	iv
Table of Contents	v
List of Figures	ix
List of Tables	xii
1 Introduction	1
1.1 Background and Reviews	1
1.1.1 Hybridization of Porous STFs	2
1.1.2 Fabrication and Optical Application of Porous Polymers	3
1.1.3 Characterization of Porous Materials	4
1.1.3.1 Characterization of Porous Properties	4
1.1.3.2 Characterization of Structural and Optical Properties for Porous STFs	5
1.2 Thesis Motivation	7
1.3 Thesis Outline	9
2 Fabrication Methods	11
2.1 Glancing Angle Deposition	11
2.1.1 Growth Mechanism	11
2.1.2 Glancing Angle Deposition System	13
2.2 Polymer Infiltration	16

2.3	Etching	18
2.4	Atomic Layer Deposition	19
3	Characterization Methods	22
3.1	Scanning Electron Microscopy	22
3.2	Energy Dispersive X-ray Spectroscopy	25
3.3	Spectroscopic Ellipsometry	27
3.3.1	General Description	27
3.3.2	Jones Matrix and Mueller Matrix	28
3.3.2.1	Jones Matrix	28
3.3.2.2	Generalized Ellipsometry	29
3.3.2.3	Mueller Matrix	30
3.3.3	Anisotropic Dielectric Function Tensor	32
3.3.3.1	Dielectric Function Tensor	32
3.3.3.2	Rotation Matrix	32
3.3.3.3	Bond Polarizability Model	33
3.3.4	Generalized Ellipsometry Modeling Approaches for Sculptured Thin Films	36
3.3.4.1	Homogeneous Biaxial Layer Approach	36
3.3.4.2	Anisotropic Bruggeman Effective Medium Approximation	38
3.3.5	Ellipsometry Data Analysis	40
3.3.5.1	Wavelength-by-Wavelength Analysis	40
3.3.5.2	Parameterized Model Dielectric Function Analysis	41
3.3.5.3	Ellipsometry Test Functions	41
4	Experiment	44
4.1	Material Fabrication	44
4.1.1	Fabrication of Permalloy SCTFs Infiltrated with Polymer	44
4.1.2	Fabrication of Porous PMMA Thin Films with Inverse SCTF Structure	45
4.2	Material Characterization	47
4.2.1	GE Measurements	47

4.2.2	SEM Measurements	47
4.2.3	EDS Measurements	48
5	Generalized Ellipsometry Analysis Approach for Porous Slanted Columnar Thin Films Infiltrated with Polymer	49
5.1	GE Data Analysis Procedure	49
5.2	SEM Analysis	51
5.3	Homogeneous Biaxial Layer Approach Analysis	53
5.3.1	Experimental and Best-model Calculated Mueller Matrix Data (1st Procedure)	53
5.3.2	Structural properties	57
5.3.3	Anisotropic Optical Properties	58
5.3.4	Discussion	60
5.4	Anisotropic Bruggeman Effective Medium Approximation Analysis	61
5.4.1	Use of Effective Optical Constants from the HBLA as Target Data	61
5.4.2	Use of Mueller Matrix Elements as Target Data (2nd Procedure)	64
5.4.3	Discussion	70
5.5	Conclusion	73
6	Optical Anisotropy of Porous Polymer Film Revealed via Generalized Ellipsometry	75
6.1	GE Data Analysis Procedure	75
6.2	SEM and EDX Analysis	77
6.3	TAB-EMA Analysis	79
6.3.1	Experimental and Best-model Calculated Mueller Matrix Data	79
6.3.2	Structural Properties	84
6.3.3	Anisotropic Optical Properties	86
6.3.4	Discussion	88
6.4	RAB-EMA Analysis	90
6.5	Conclusion	92

7 Summary and Outlook	94
References	108

List of Figures

1.1	Schematic for the as-deposited SCTF, SCTF infiltrated with polymer and porous polymer with inverse columnar structure	8
2.1	Scheme of the deposition process of STFs	12
2.2	Photograph of the UHV GLAD system	14
2.3	Scheme of GLAD process	15
2.4	The cross-section SEM image of STFs	16
2.5	Photograph of the ALD system indicative of main components . .	20
3.1	Diagram of several signals generated from electron-specimen interactions	24
3.2	Energy diagram for an atom	26
3.3	The scheme of ellipsometry measurement	28
3.4	Definition of the Euler angles	33
3.5	Definition of α , β and γ	35
3.6	Scheme of AB-EMA	38
4.1	The scheme for the preparation process for porous PMMA thin films with inverse SCTF structure	45
5.1	Optical Models for the as-deposited permalloy SCTF and permalloy SCTF infiltrated with PMMA	50
5.2	The cross-section SEM images of the permalloy SCTF and SCTF infiltrated with PMMA	52

5.3	Mueller matrix elements of the permalloy SCTF and SCTF infiltrated with PMMA	54
5.4	Off-diagonal Mueller matrix elements of the permalloy SCTF and SCTF infiltrated with PMMA	55
5.5	Mueller matrix elements of permalloy SCTF and SCTF infiltrated with PMMA within spectral range from 400 to 1650 nm	56
5.6	Effective optical constants of the permalloy SCTF and SCTF infiltrated with PMMA obtained from HBLA	58
5.7	The birefringence and dichroism obtained from the HBLA for the permalloy SCTF and SCTF infiltrated with PMMA	59
5.8	Effective optical constants along the major axes determined by the HBLA, TAB-EMA and RAB-EMA in the 1st procedure	62
5.9	Bulk optical constants of permalloy determined by TAB-EMA (dashed lines) and RAB-EMA (dotted lines) in the 1st procedure	64
5.10	Best-model calculated off-diagonal Mueller matrix elements obtained from TAB-EMA and RAB-EMA in the 2nd procedure	65
5.11	Effective optical constants along the major axes determined by the HBLA, TAB-EMA and RAB-EMA in the 2nd procedure	68
5.12	Bulk optical constants of permalloy determined by TAB-EMA (dashed lines) and RAB-EMA (dotted lines) in the 2nd procedure	69
6.1	Optical Models for the as-deposited Co SCTF, Co SCTF infiltrated with PMMA, Co SCTF infiltrated with PMMA after RIE and PMMA iSCTF film.	76
6.2	The cross-section SEM images of the as-deposited Co SCTF and PMMA iSCTF	77
6.3	EDX spectra of the as-deposited Co SCTF and PMMA iSCTF.	78
6.4	Experimental and best-model calculated off-diagonal Mueller matrix elements for the samples at different preparation steps	80
6.5	Off-diagonal Mueller matrix elements of the Co SCTF and PMMA iSCTF	81
6.6	Mueller matrix elements of the Co SCTF and PMMA iSCTF	82

6.7	Effective optical constants of Co SCTF and PMMA iSCTF obtained from TAB-EMA	87
6.8	The birefringence and dichroism obtained from the TAB-EMA for the as-deposited Co SCTF and PMMA iSCTF	88
6.9	Effective optical constants of the PMMA iSCTF obtained from the RAB-EMA and TAB-EMA	92

List of Tables

3.1	Symmetries and dielectric tensor properties of symmetrically dielectric materials	37
5.1	The best-model parameters for the permalloy SCTF and SCTF infiltrated with PMMA obtained from the HBLA	57
5.2	The best-model parameters for the permalloy SCTF and SCTF infiltrated with PMMA obtained from TAB-EMA and RAB-EMA in the 1st procedure	63
5.3	The best-model parameters for the permalloy SCTF and SCTF infiltrated with PMMA obtained from TAB-EMA and RAB-EMA in the 2nd procedure	66
5.4	Comparison between the best-model parameters in the 2nd procedure with the calculated values	71
6.1	The structural parameters for the Co SCTF and PMMA iSCTF from SEM analysis	78
6.2	The best-model parameters obtained from TAB-EMA: (a) as-deposited Co SCTF; (b) Co SCTF infiltrated with PMMA; (c) Co SCTF infiltrated with PMMA after RIE; (d) PMMA iSCTF.	84
6.3	The best-model parameters obtained from RAB-EMA and TAB-EMA for the PMMA iSCTF.	91

Chapter 1

Introduction

1.1 Background and Reviews

Porous materials are solid materials containing ordered or disordered pores (voids) within the matrix media which could be made of organic or inorganic materials. Porous materials have become a subject of significance for academic and industry research since porosity can lead to a variety of new properties, functions and applications. For instance, high porosity can result in large surface areas providing tremendous active sites for adsorption or reactions which benefit applications such as catalysis and electrochemical supercapacitors^(1,2). Porosity also leads to effective optical properties within materials which can be tuned by controlling the pore size, shape and distribution. Tunable optical properties contribute to the use of porous materials in photonic crystals and antireflection coating^(3,4). In addition, the porous regions allow for material infiltration and functional group attachment, which offers great opportunities to obtain composite materials or incorporate additional functions.

Due to the enormous value in porous materials, great research efforts have been undertaken on fabricating porous materials in different forms, such as monoliths, thin films, powders and solutions. The fabrication of porous thin films has received much attention because of the potential applications of porous films in particular areas, such as coating technology and microelectronic system⁽⁵⁻⁷⁾. Recently, glancing angle deposition (GLAD), a bottom-up and one-step method,

has been utilized to prepare highly porous sculptured thin films (STFs) from inorganic and organic materials⁽⁸⁻¹¹⁾. Various nanocolumnar structures, such as slanted columns, chevron and spiral, can be easily obtained by manipulating deposition conditions, such as substrate rotation. The large interspacing between individual columns defines the pore regions within STFs. STFs contain ensembles of three-dimensional (3-D) nanostructures and possess strong form-induced optical anisotropy. The porous STFs have been employed in many fields of application such as sensor devices⁽¹²⁻¹⁴⁾, antireflection⁽¹⁵⁾ and engineered optical materials⁽¹⁶⁻¹⁹⁾.

1.1.1 Hybridization of Porous STFs

Hybridization of STFs is achieved by infiltrating other materials into the porous regions of STFs. Hybridized STFs with functional materials such as conjugated polymers and liquid crystals have attracted intense research interests, since the applications of hybridized STFs can extend to various areas, such as hybrid organic-nanocolumnar solar cells and sensing devices^(9,17,20-22). For instance, filling porous metal oxide nanocolumnar thin films with conjugated polymers has been utilized to prepare organic-inorganic hybrid materials with optimal photovoltaic performances^(20,23,24). The optical anisotropy of STFs is highly sensitive to material infiltration, which can be exploited for sensing applications^(9,21). For example, since the dielectric constants of the infiltration materials affect the optical response of the helix STFs, a circular polarization filter can be prepared from helix columns to sense the fluid concentrations in the porous regions^(9,21). Many researchers have reported on the optical property changes of STFs upon polymer or fluid infiltration using different methods^(21,22,25-27). Robbie *et al.* found that the transmission difference between right-handed and left-handed circular polarized light can be enhanced by chiral STFs infiltrated with nematic liquid crystals (LCs), compared to pure LCs⁽²²⁾. In another study, tungsten nanocolumns grown via GLAD were impregnated with poly(p-phenylene vinylene) (PPV) and the photoluminescence emission and absorption of the polymer were improved due to the increased PPV surface areas, excitation and emission cross sections⁽²⁵⁾. Steele *et*

al. fabricated optical interference filters composed of porous titanium oxide STFs with a sinusoidal refractive index profile. The filter exhibits fast bandpass spectral shifts upon water vapor adsorption and desorption in the porous regions.

1.1.2 Fabrication and Optical Application of Porous Polymers

Introduction of porosity into polymers has been demonstrated to be an effective and facile manner to create new polymeric systems, adding more functionalities to the bulk materials. A key issue is the methodology by which the porosity is created in bulk polymers with desired characteristics, such as pore size, morphology, *etc.* Recently, a variety of methodologies for fabricating porous polymers have been extensively researched, mainly including templating synthesis, block copolymer self-assembly and direct synthesis⁽²⁸⁻³²⁾. In templating synthesis, nanoscale porosity is generated by filling polymer into the voids of a nanostructured template and subsequently removing the template. In the second method, self-assembly of block copolymers (BCPs) causes a phase separation between two or more chemically immiscible homopolymers, then sacrificing one homopolymer segment generally leads to a highly ordered porous system⁽³³⁻³⁶⁾. Finally, direct synthesis employs chemical reactions to generate pores directly or induce phase separation within polymers during the polymerization. Many researchers have used nanostructured templates in conjunction with atomic layer deposition to obtain porous thin films⁽⁵⁻⁷⁾. Among the approaches, no method is superior than another in all respects, the goal is to find facile and effective routes allowing for good control over the properties such as pore size, morphology, surface condition, *etc.*

Templating synthesis is essentially a molding and casting methodology to produce porous polymers with inverse structure of the templates⁽²⁸⁾. The synthesis procedure mainly includes the following steps⁽²⁸⁾: (1) design and preparation of the templates with desired nanostructures; (2) infiltration or adsorption of raw materials (polymer melts, polymer solutions, polymer precursors, or monomers) into the void regions or on the surface of the templates; (3) solidification or polymerization of polymers; (4) selective removal of the templates using etching techniques.

The common templates used in this method include colloidal crystals of silica or polymers (PMMA, polystyrene, *etc.*)⁽³⁷⁻³⁹⁾, spherical nanoparticles of organic or inorganic materials⁽⁴⁰⁻⁴³⁾, porous membranes with cylindrical pores⁽⁴⁴⁻⁴⁷⁾. To fulfill a precise duplication of the template structures, the templates should possess well-defined and tunable nanostructures such that the pore morphology can be controlled, and excellent infiltration of the raw materials into the templates must be reached such that void defects in polymer framework could be avoided.

Research efforts have been devoted to using porous polymers in various application areas including templates for nanostructured materials, low-dielectric constant materials and so on⁽⁴⁸⁻⁵⁰⁾. In particular, it has been a research focus to tailor the optical properties by introducing pores with variable sizes and shapes to the solid films, because such tunable optical properties allow for the applications of porous polymer films in many areas, such as optical sensing and antireflection coatings⁽⁵¹⁻⁵⁴⁾. For instance, porous polymer films with tuneable porosity have been prepared with different phase-separation approaches to achieve desired low refractive indices or gradient refractive indices and demonstrated to be excellent candidates for polymeric antireflection coatings^(52,55-57). With optically induced alignment, elongated pores were uniaxially aligned within liquid crystal polymer films which could produce strong birefringence⁽⁵³⁾. Harris *et al.* fabricated porous photoresist films with inverse helical pore structure which cause large optical rotation to the incident polarized light due to the large difference of refractive index between pores and polymers⁽⁵⁴⁾. Many researchers reported the application of porous polymeric photonic crystals for organic vapor, humidity or drug sensing⁽⁵⁸⁻⁶²⁾. The sensing mostly depends on the stopband changes of the porous polymers which occur when the vapor analytes permeate into the pores and change the porous volume or refractive index^(51,58,62).

1.1.3 Characterization of Porous Materials

1.1.3.1 Characterization of Porous Properties

A crucial task for porous material research is to characterize the multiple properties and performances. Void fraction (porosity), surface area and pore size dis-

tribution (PSD) are unique properties to be evaluated for porous materials. One of the common methods is using gas adsorption isotherm to obtain porous properties of monoliths and powders^(29,63,64). Top-down scanning electron microscopy (SEM) and atomic force microscopy (AFM) are widely used to study the porosity, pore size and surface morphologies for porous films.^(65–67) The non-destructive techniques, including X-ray reflectometry (XRR), small angle X-ray scattering (SAXS), small angle neutron scattering (SANS) and so on, have been used to determine the porous properties of thin films.^(68–71)

Ellipsometry has been extensively used as a non-destructive optical method to determine the thickness, porosity, pore shape, pore size distribution (PSD) and optical constants of porous polymeric films^(72–77). In particular, ellipsometry porosimetry (EP), which combines adsorption/desorption technique and spectroscopic ellipsometry, provides access to the PSD of porous polymer thin films^(72,73,77–82). In EP, the adsorption/desorption of organic vapors in the pores induces the changes of refractive index and thickness of the samples which are determined by ellipsometry⁽⁸³⁾. The volume fractions of the pore and vapors are generally determined using the Lorentz-Lorentz equation or Bruggeman effective medium approximation (BEMA)^(73,78,83). The dependence of the vapor volume fraction on vapor relative pressure is an adsorption/desorption isotherm, which is used to calculate the PSD with the Kelvin equation⁽⁸³⁾. Vayer *et al.* used EP to characterize porous poly(-styrene) films with cylindrical pores. Their results from adsorption/desorption isotherm and PSD suggest that the cylindrical pores were open at both ends and some adjacent pores are interconnected at the substrate/film interface⁽⁷³⁾.

1.1.3.2 Characterization of Structural and Optical Properties for Porous STFs

Many conventional techniques are not suitable to characterize the porous STFs with complex three-dimensional (3-D) nanostructures. For instance, the top-down SEM analysis can only determine the porosity for vertically aligned nanocolumns^(84–86). It is difficult to apply the gas adsorption isotherm involving nitrogen or argon

to STF films with thickness of only hundreds of nanometers, because this technique is not sensitive to detect the small mass changes on the films to gas adsorption^(83,87,88). Krause *et al.* showed that the gas adsorption using krypton is not applicable to vertically aligned nanocolumns deposited at high oblique angles ($> 65^\circ$), since complete pore filling is difficult to reach due to bulk solidification⁽⁸⁸⁾. SAXS and SANS have difficulty in determining the film thickness and need to be combined with other techniques to obtain the film porosity^(80,87).

In addition to the porous structures, the anisotropic optical behaviors of the STFs are also important for investigation. However, because of the complex 3-D structure of the films, it is difficult to find an optical analysis technique which fully characterizes the anisotropic optical properties. Transmittance or reflectance spectra are generally used to investigate the optical properties, such as birefringence and photonic stop bands^(9,89–91). Unfortunately, the biaxial optical properties of STFs with three principal optical axes can hardly be obtained with such methods. Besides, the optical analysis with those methods provides limited access to studying the structural properties. Last but not least, effective methods are lacking to evaluate the constituent fractions of hybridized STFs consisting of multiple components. Material infiltration could also induce changes in the columnar structure of STFs. The characterization of STF structural properties, such as column dimension and tilt angle, is mainly dependent on SEM^(92,93). But SEM can only reflect the localized morphology of certain areas in STFs, rather than an average property. Besides the sample preparation for SEM could be destructive to organic STF structures.

Previously, Mueller matrix generalized ellipsometry (MMGE) has proven to be an effective tool to investigate the intrinsic structural parameters and biaxial optical properties of porous slanted columnar thin films (SCTFs)^(94–96). The changes in optical anisotropy of SCTFs upon infiltration can be also monitored by GE^(97,98). For example, May *et al.* discovered a change in the anisotropic optical response of TiO_2 SCTFs due to molecule adsorption and found that individual Mueller matrix elements respond to the adsorption differently⁽⁹⁸⁾. Nevertheless, in order to precisely identify the changes in structural parameters and effective optical constants, appropriate physical models are required to analyze the GE

experimental data measured on SCTFs before and after infiltration. Recently, the homogeneous biaxial layer approach (HBLA) has been employed to model the GE data to obtain film thickness, columnar slanting angle and the effective optical constants of SCTFs^(97,99,100). In order to gain quantitative information about constituent fractions of porous SCTFs, the anisotropic Bruggeman effective medium approximation (AB-EMA) has been utilized^(94,96,101–105). Hofmann *et al.* employed an AB-EMA model to describe the dielectric and structural anisotropy of cobalt SCTFs at terahertz frequencies and indicated that the optical response varies depending on the ambient surrounding the nanostructures^(102,104). Rodenhäuser *et al.* showed that GE can be used to dynamically detect the amount of protein adsorption into the voids of SCTFs⁽¹⁰⁵⁾. However, limited research is conducted on using GE data analysis approaches to study how the infiltration affects the structure, birefringence and dichroism of SCTFs.

1.2 Thesis Motivation

The high porosity in STF provides a platform to hybridize with functional materials. Hybridized STFs are created by infiltrating materials into the open pores of STFs. The infiltration materials can thereby add functionality and alter the physical properties of STFs. Particularly, the optical properties of the STFs are highly sensitive to the infiltration materials in the porous regions. However, due to the complexity of anisotropic nanostructures within the films, it is difficult for optical analysis approach to characterize the changes in the optical properties of STFs upon material infiltration. In addition, accurate determination of porosity and structural changes due to infiltration remains a challenge for hybridized STFs.

STFs can also be employed as templates for preparation of inverse porous polymer thin films. Through hybridization of STFs with polymers and selective removal of STFs, porous polymeric systems with inverse STF structures (inverse-STF polymer films) can be obtained. The pore structures of the inverse-STF polymer films can be tuned by fabricating STF templates with various 3-D nanostructures. Since geometrical properties of porous polymer films, such as surface area and pore structure, are controlled by the STF morphology, the choice of templates

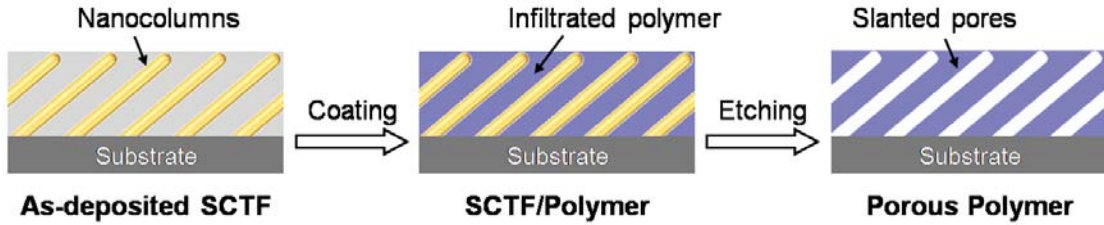


Figure 1.1: Schematic for the as-deposited SCTF, SCTF infiltrated with polymer and porous polymer with inverse columnar structure.

is a significant tool to design porous polymeric films towards their anticipated application. In particular, the optical properties of inverse-STF polymer films can be tailored by introducing different pore structures. For example, inclusion of nanopores with anisotropic STF shapes (*e.g.*, slanted nanocolumn) in isotropic media results in anisotropic optical behaviors of porous films. Determination of the anisotropic optical properties, such as anisotropy classes (*e.g.*, tetragonal, monoclinic) and structures (sequence of magnitude of principal optical constants, for example $n_a > n_b > n_c$, with n_a , n_b and n_c being the optical constants along each major polarizability axis), becomes crucial to improving the fabrication and design for inverse porous films with desired optical performances^(51–54).

In the present thesis, a non-destructive optical characterization method, generalized ellipsometry (GE), is employed to investigate the structural and optical properties of two anisotropic nanoporous media: (1) porous SCTFs with or without polymer infiltration; (2) porous polymer films with inverse columnar structure. First, GLAD was utilized to fabricate porous SCTFs and hybridized SCTFs were prepared by infiltrating polymers into the porous regions of the as-deposited SCTFs as shown in Fig. 1.1. GE analysis combining two modeling approaches, the HBLA and AB-EMA, is utilized to analyze the GE data of the SCTFs and hybridized SCTFs to identify the changes in structural and optical properties upon infiltration. Secondly, the porous polymer films with inverse SCTF structure were prepared by a selective etching on the SCTF templates after polymer infiltration as shown in Fig. 1.1. GE analysis with AB-EMA is employed to study the porosity, composition, pore shape and optical anisotropy of the porous polymer films.

The significance of results obtained from different physical models are compared to each other.

1.3 Thesis Outline

The present thesis is organized as follows: chapter 2 gives a brief introduction to the fabrication techniques and apparatus (*e.g.*, GLAD). Chapter 3 depicts the working principles for the employed characterization methods, particularly the theory of GE is briefly reviewed. Chapter 4 describes the experimental details on the preparation and characterization of porous SCTFs infiltrated with polymers and porous polymer films with inverse SCTF structure.

In chapter 5, a GE analysis approach, combining HBLA and AB-EMA, is used to determine the structural and anisotropic optical properties of multi-constitutional SCTFs. The Mueller matrix GE measurements are conducted on permalloy ($\text{Ni}_{80}\text{Fe}_{20}$) SCTFs before and after infiltration with poly(-methyl methacrylate) (PMMA). The SCTF thickness and nanocolumn slanting angle obtained from the HBLA analysis on the GE data are compared to SEM results. The changes in birefringence and dichroism upon infiltration are also identified by the HBLA modeling. Two AB-EMA formalisms are employed to evaluate constituent fraction changes. The effective optical constants obtained by the HBLA and the experimental Mueller matrix data are used as the target data for the AB-EMA modeling, respectively, in two different procedures.

In chapter 6, GE is utilized to investigate the anisotropic optical properties of porous PMMA thin films with inverse SCTF structure (PMMA iSCTFs). The PMMA iSCTFs were prepared via infiltration of PMMA into cobalt (Co) SCTFs and subsequent etching of SCTF templates. The Mueller matrix element data measured on PMMA iSCTFs and Co SCTFs are analyzed by the AB-EMA to determine the structural and biaxial optical properties. From the GE data analysis, it is revealed that the optical behaviors of PMMA iSCTFs and SCTFs follow the electromagnetism reciprocity theorem where time-harmonic electric current densities (polarizabilities) and resulting electromagnetic fields are interchangeable as response and source, respectively.

Chapter 7 summarizes the results and conclusions. A brief outlook is also presented in this chapter.

Chapter 2

Fabrication Methods

2.1 Glancing Angle Deposition

2.1.1 Growth Mechanism

GLAD is a recent innovation of oblique angle deposition (OAD) by introducing substrate rotation control⁽⁹⁾. In OAD, the trajectory of a highly directional vapor flux is oblique to the substrate normal, which can generate inherently anisotropic thin films. An atomic-scale self-shadowing effect, which becomes prominent with deposition angle higher than 65° , is the key to the deposition process. The competitive growth due to self-shadowing effect in combination with a reduced surface diffusion leads to a mechanism that the vapor can only condensate on nuclei which are initially formed on a substrate. The left scheme in Fig. 2.1 describes the phenomenon of self-shadowing during the fabrication of slanted columns. By adding substrate rotation to OAD, GLAD technique provides great opportunity to fabricate various types of nanostructures. The substrate rotation changes the direction of the incident vapor and the dynamics of self-shadowing during the deposition. Therefore, the column growth can be manipulated to form desired nanostructures by simply adjusting the manner of substrate rotation. The right scheme in Fig. 2.1 depicts the formation of helical nanostructure by rotating the substrate continuously.

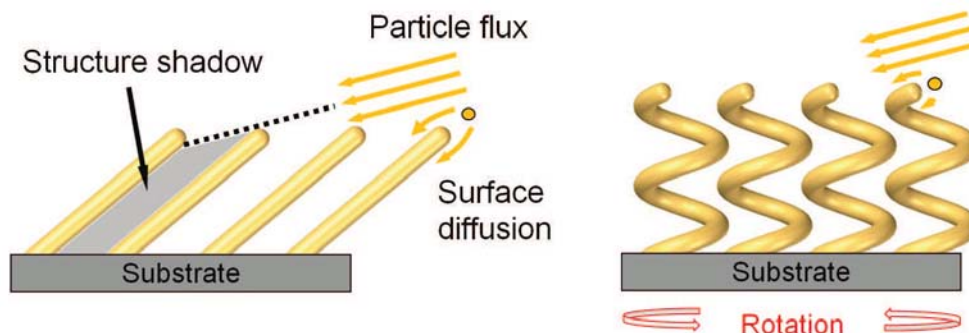


Figure 2.1: Diagram of the deposition process of typical STFs: slanted columnar thin films (left); helical thin film (right). Scheme adapted from Schmidt⁽¹⁰⁷⁾.

By using different substrate motions, a variety of 3-D nanostructures, including slanted columns, vertically aligned posts, zigzags, spirals and combined nanostructures, can be obtained. The 3-D nanostructures arrange in ensemble forming highly porous thin films, generally named sculptured thin films (STFs). The large porosity can be exploited by adding materials with different functionalities to create the class of nanohybrid functional materials. STFs can be grown from various materials, such as metals, alloy, oxides and semiconductors. Because of the self-shadowing growth mechanism, GLAD can be applied to arbitrary substrates in principle^(8-10,106).

GLAD with a stationary substrate can be used to fabricate slanted columnar thin films (SCTFs). At the initial stage of the deposition, a large number of nuclei are formed randomly on the substrate and become the nucleation centers for the subsequent nanostructure growth. As the deposition continues, the shadowing effect dominates the process such that the nuclei receive more vapor than the shadowed areas behind them and low temperatures minimize the surface diffusion. Eventually the nuclei develop into nanocolumns which are tilted towards the vapor flux source. The columns are initially symmetric with a typical diameter of 20 nm approximately. As the columns grow, fanning-out of the columns will occur in the direction perpendicular to the incident vapor direction, which results in a lateral broadening of the columns^(9,108). Much research work has been devoted to

establish the relation between flux incident angle and the tilt angle of the deposited columns⁽¹⁰⁹⁻¹¹⁴⁾. It was found that the tilt angle is a function of the surface energies of both substrate and deposited film, such that different combinations of substrate and thin film materials yield different inclination angles. Thus the prediction of the column tilt angle can be difficult especially if the knowledge about the specific surface energies is absent⁽⁹⁾.

With a continuous substrate rotation at a relatively slow rate, the nanocolumns have sufficient time to grow along the direction of the incoming flux, which leads to helical structure formation. The deposition parameters such as time interval of each rotation step and the deposition angle determine the fine structure of helical thin films including the perimeter of each loop, diameter of the nanocolumns, the number of the turns, pitch, etc⁽⁹⁾. Vertically aligned columnar thin films can be formed by fixing the deposition angle and controlling the in-plane substrate rotation at an appropriate speed. The speed of the rotation must be increased to a higher level than that used for growing helical structures. The zigzag structure can be grown by changing in-plane azimuth between $\pm 180^\circ$ at a constant deposition angle.

2.1.2 Glancing Angle Deposition System

The GLAD system used for STF fabrication is shown in Fig. 2.2. The system is composed of a load-lock chamber and a deposition chamber. The load-lock chamber functions as a transitional stage between atmospheric pressure and ultrahigh vacuum (UHV). The sample can be transferred from the load-lock chamber into the deposition chamber without interruption of UHV. The pressure is monitored with a Bayard-Alpert hot cathode ionization measurement system for pressure below 2×10^{-2} mbar and a Pirani gauge for pressure above 5.5×10^{-3} mbar⁽¹¹⁵⁾. A scroll vacuum pump and a turbomolecular pump attached to the load-lock chamber can produce a high vacuum within 5 minutes. The scroll vacuum pump is firstly used to reach a pressure of approximately 4×10^{-2} mbar and the turbomolecular pump is subsequently switched on to obtain a pressure of 10^{-6} mbar⁽¹¹⁵⁾. Once the vacuum condition of 10^{-6} mbar is reached, the gate valve connecting

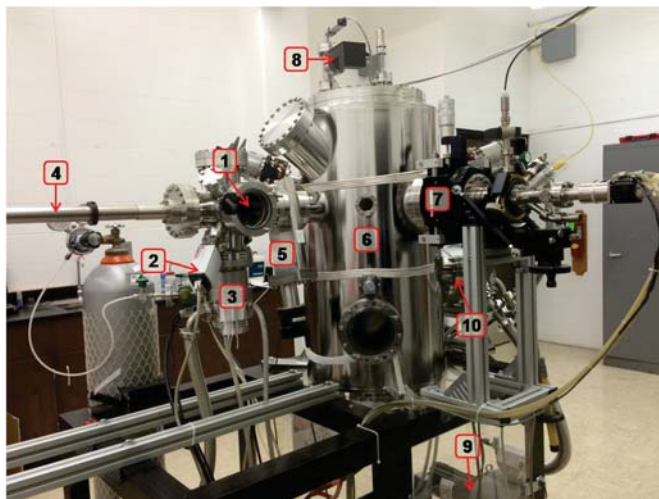


Figure 2.2: Photograph of the UHV GLAD system: (1) load-lock chamber, (2) vacuum gauge, (3) turbomolecular pump, (4) magnetically-coupled linear-rotary feedthrough, (5) gate valve, (6) deposition chamber, (7) sample manipulator, (8) vacuum gauges, (9) mechanical scroll pump, (10) turbomolecular pump. Items (1)-(4) are for the load-lock chamber whereas (6)-(10) for the deposition chamber.

the two chambers can be opened and the sample can be transferred to the sample manipulator in the deposition chamber with a magnetically-coupled linear-rotary feedthrough system.

The deposition chamber is an UHV system equipped mainly with an electron beam evaporator, a sample manipulator and quartz crystal microbalance (QCM) deposition controller. The gauge system comprises a transmitter (based on the Pirani thermal conductivity principle) for the pressure range from 5×10^{-4} to 1000 mbar and a Penning gauge for the range from 1×10^{-9} to 1×10^{-2} mbar⁽¹¹⁵⁾. A mechanical scroll pump and a turbomolecular pump are utilized to reach a pressure of 10^{-8} mbar regularly.

A general experimental setup for GLAD process in the deposition chamber is described schematically in Fig. 2.3. The electron beam evaporator system located at the bottom of the deposition chamber is used to provide a stable vapor flux for the deposition. The electron gun with tungsten filament emits the electrons

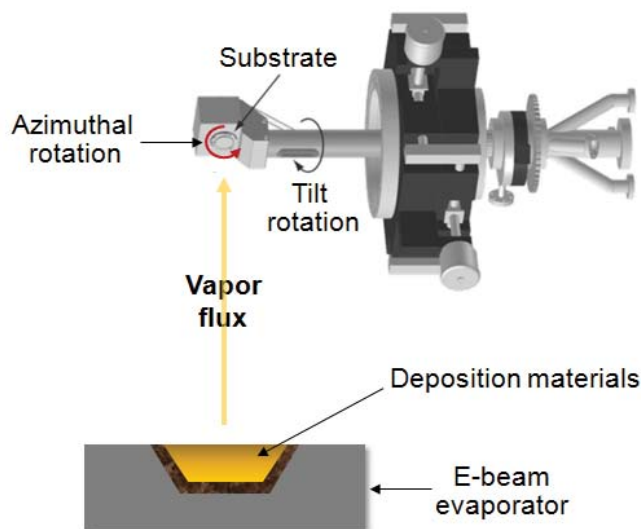


Figure 2.3: Scheme of GLAD process⁽¹¹⁶⁾.

which can be accelerated in an electrical field (potential difference up to 10 kV) and directed by a constant magnetic field to impinge the source material⁽¹¹⁵⁾. The material loaded in a pocket is heated by the electron beam with a maximum current of 800 mA to reach evaporation and generate vapor flux. The deposition rate can be adjusted by controlling the electron beam current. The QCM deposition controller is employed to monitor the deposition rate in the chamber. The controller located close to the substrate holder is installed with its surface normal to the incident vapor flux.

The sample manipulator is used to control the tilt rotation to adjust the angle (deposition angle) between incident flux and the substrate normal and the azimuthal (in-plane) rotation of the substrate with respect to the substrate normal. The tilt rotation is achieved with a differentially pumped rotary feedthrough by $\pm 180^\circ$. The azimuthal rotation is manipulated with a computer controlled stepper motor which enables precise control over rotating speed and direction.

Fig. 2.4 shows the cross-sectional images of STFs with different nanostructures grown via our GLAD system. Fig. 2.4(a) shows an image of permalloy SCTF deposited on Si substrate. The source material for deposition is composed of

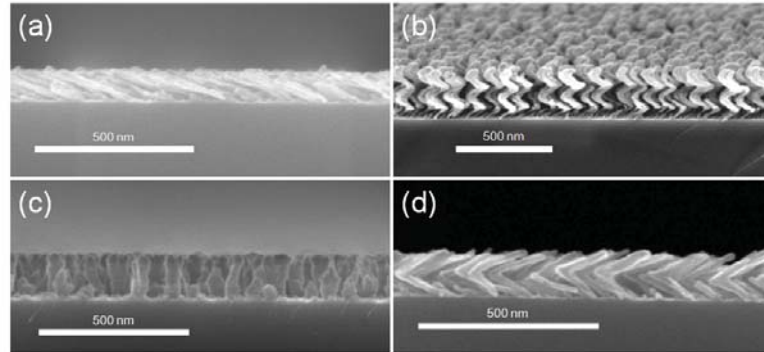


Figure 2.4: Cross-section SEM images of STF films with different nanostructures grown via GLAD: (a) permalloy slanted nanocolumns; (b) Si helical nanocolumns; (c) Co vertically-aligned nanocolumns; (d) Ti zigzag nanocolumns⁽⁹⁷⁾. Note the film plane in (b) is tilted. Scar bar: 500 nm.

81 wt% Ni and 19 wt% Fe (SCM, Inc.). The deposition was conducted at an oblique angle of 85° and the deposition rate is maintained constantly between 3 and 4 $\text{\AA}/\text{s}$ measured at normal incidence. The SEM image of a typical helical thin film prepared from Si is shown in Fig. 2.4(b). The film was deposited at a deposition angle of 85° with a counterclockwise substrate rotation of 0.1 rpm. The deposition rate was maintained at 4 $\text{\AA}/\text{s}$ for 22 min, which results in two complete 360° substrate rotations. Co vertically-aligned nanocolumns shown in Fig. 2.4(c) were deposited at a deposition angle of 85° with a counterclockwise substrate rotation of 5 rpm and a deposition rate of 4.7 $\text{\AA}/\text{s}$ for 8 min. For the zigzag structure shown in Fig. 2.4(d), the first layer was deposited at a deposition angle of 85° for 5 min, subsequently an in-plane rotation of 180° was conducted within 15 s, and the substrate position remained unchanged to grow the second layer for another 5 min⁽⁹⁷⁾.

2.2 Polymer Infiltration

Three methods are mainly utilized to achieve polymer infiltration into porous materials. First method involves use of elevated temperature above T_g (glass tran-

sition temperature) or T_m (melting temperature) of polymers. Under such high temperature conditions, solid polymers are transformed into their liquid form with low viscosity which enables the polymer to spread into the porous regions. In this method, no organic solution is needed and the solid polymer is in contact with the porous materials before increasing temperature. The second method utilizes the polymers in their solution forms for infiltration. In this method, two approaches are frequently used to perform the infiltration: direct submerging and spin-coating. In the first approach, the porous materials are submerged into the polymer solutions for certain time at room temperature. The second method employs external forces, such as vacuum and pressing, to achieve a good infiltration^(117,118). The infiltration is mostly determined by the viscosity of the polymer fluid rather than the wetting condition⁽¹¹⁷⁾. In the third approach, the polymer solutions are spin-coated onto the porous materials. After the infiltration, the solutions must be vaporized at elevated temperatures.

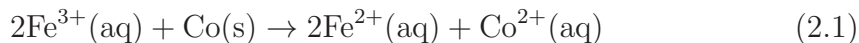
Spin-coating is a solution-based deposition technique which utilizes the centripetal force during the spinning to form a uniform thin film with a specific thickness. This technique is a simple, low-cost and effective way which has been broadly used for polymer thin film deposition (*e.g.*, photoresist for patterning wafers, organic solar cells) in industry production and academic research⁽¹¹⁹⁾. A spin-coating process generally includes four steps. First, the solution is dispensed onto the substrate. Secondly, the substrate spinning is accelerated and stabilised at a specific speed to spin off the extra solution. Thirdly, the solvent evaporates at the constant spinning speed and the film on the substrate becomes thinner. Finally, the obtained film is dried at specific temperature to further evaporate the solvent. The film thickness is mainly controlled by two factors^(119,120): (1) spin-coating conditions such as spinning speed and spinning time; (2) solution properties such as solution viscosity and solute concentration. Increasing spinning speed or spinning time leads to thinner films, while increasing solution viscosity or solute concentration results in thicker films. In this thesis, spin-coating and baking above T_m of the polymer was utilized for polymer infiltration into porous SCTFs.

2.3 Etching

Selective removal of the templates is the final step towards the formation of porous structures in polymers, which is generally performed with etching techniques. Etching is essentially a process to remove the undesired materials with chemical or physical methods such that the nanostructured pattern can be accurately reproduced in the remaining materials⁽¹²¹⁾. Several parameters are used to evaluate the etching process, including etching rate, etching profile, selectivity, *etc.* The etching process is generally classified into two types: dry etching and wet etching.

Dry etching utilizes plasma generated in the gas state to etch the materials, therefore it is a plasma etching process. Two plasma-sample interactions occur simultaneously. First, energetic particles (*e.g.* heavy positive ions) physically impinge on the sample surface to remove the materials, which is referred as physical etching. Secondly, energetic particles (*e.g.* radicals) in plasma react chemically with the materials on the sample surface, which is referred as chemical etching. Physical etching generally leads to an anisotropic etching profile while chemical etching results in an isotropic profile. The material removal is a combined effect from both physical and chemical etching. Reactive ion etching (RIE) is a plasma etching technique utilizing physical and chemical processes for material removal. In RIE, the etching gas is dissociated after being subjected to an radio frequency AC field to generate positive ions, radicals, free electrons, *etc.* A DC self-bias is developed on the cathode to create voltage difference between sample and plasma, such that the ionized particles can be directed to bombard the sample surface to improve anisotropic etching. Finally, the etch by-product is removed via the exhaust. In addition, modern RIE systems are attached with inductively-coupled plasma (ICP) generator to create high-density plasma⁽¹²¹⁾. In ICP, a spiral inductive coil is utilized to produce an electromagnetic field for plasma generation. A broad range of etchant gases can be utilized for selective etching on different templates. For instance, fluorine-based gases (*e.g.* CF_4 , CHF_3 , SiF_4) etch oxide materials, SF_6 and CF_4 with addition of O_2 etch silicon, chlorine-based gases (*e.g.* BCl_3 , Cl_2) etch aluminum⁽¹²¹⁾. O_2 is generally used for polymer etching.

In wet etching, material removal is realized by the chemical reaction between chemical reagent solutions and samples, and the by-products are resolved in the solution and discarded, or they can be removed in a rinsing process. Wet etching is typically an isotropic etch process. The etching rate can be adjusted by reagent concentration, temperature and etch time, but it is more difficult to control in wet etching than plasma control. Nevertheless, wet etching has several advantages over plasma etching. First, it has low requirements on technical equipment. Secondly, plasma damage is avoided in wet etching. Furthermore, a wide range of wet etch recipes can be used to obtain a highly selective process which is not available in plasma etching⁽²⁸⁾. For instance, silica templates can be easily removed by HF or NaOH, some polymer templates can be removed by organic solvents. Thus wet chemical etching is the major method for porous polymer preparation. In the present thesis, an aqueous iron chloride (FeCl_3) solution is employed to etch the Co STF templates. The ionic equation of the chemical reaction can be expressed as⁽¹²²⁾:



where aq and s stand for aqueous and solid states, respectively. This reaction etches Co layers effectively without forming gaseous products or precipitates.

Two etching methods are employed for preparation: plasma and chemical wet etching. Firstly, RIE is used to remove the extra top polymer layer on SCTFs after spin-coating. This step is carefully controlled such that the SCTFs infiltrated with polymer remain intact. Secondly, wet chemical etching is used to remove the STF templates. With this preparation, a polymer matrix is created which resembles the SCTFs in its void structure.

2.4 Atomic Layer Deposition

Atomic layer deposition (ALD) is a CVD process with repeating gas-solid reaction cycles to grow materials layer by layer. The irreversible and saturating gas-solid reactions, for instance chemisorption of the reactants, are the key features for a conformal, uniform and dense deposition on complex three-dimensional structures^(123,124). One cycle of a two-reactant ALD process typically comprises of four

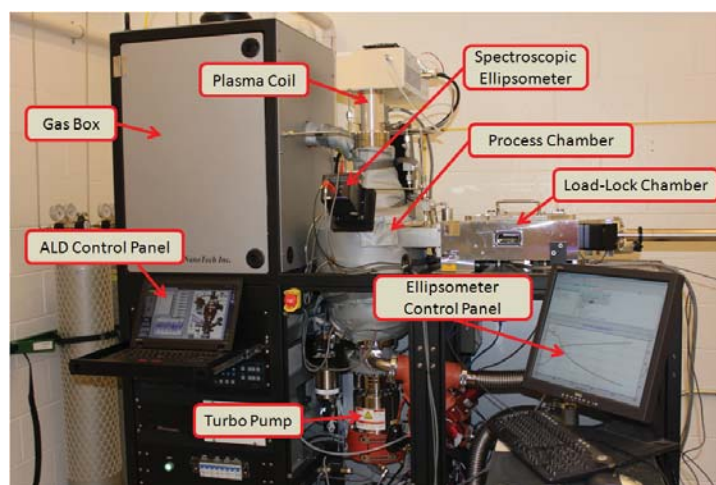


Figure 2.5: Photograph of the ALD system indicating main components.

steps⁽¹²⁴⁾. In the first step, the first reactant, generally a metal reactant, is chemically adsorbed on the substrate; secondly, the unreacted gases and by-products are removed by a purge or evacuation step; thirdly, the second reactant (non-metal reactant) is introduced to react with the first reactant. Fourth step is a purge step to remove the unreacted gases and by-products. This cycle is repeated to gradually increase the material thickness. The pulse-controlled process in ALD allows for accurate control over the thickness. A wide range of ALD reactions have been developed for the growth of various materials, including metal oxides, noble metals, *etc*⁽¹²⁴⁾.

In the present thesis, ALD is employed to deposit an ultrathin oxide layer onto porous PMMA films for SEM investigation. When porous PMMA films are subjected to high energy electron beam, damage or deformation of the nanostructure could occur, thus it is very difficult to obtain SEM images with high resolution to reveal the nanoporous structure. In general, a layer of inorganic materials is required to coat on the polymer to protect the porous polymer structure from electron beam damage. In this thesis, an aluminum oxide (Al_2O_3) layer with a thickness of approximately 5 nm was deposited on the porous PMMA via ALD. The ALD system (Fiji 200, Cambridge NanoTech Inc.) used for deposition is shown in Fig. 2.5. The main components of the system include gas (precursor)

cabinet, ALD control panel, process chamber, load-lock chamber, turbo pump. A spectroscopic ellipsometer is attached to the ALD process chamber, allowing for in-situ monitoring of the thin film growth process. The system is capable of depositing substrates with size up to 200 mm via thermal or plasma-assisted process. The system is equipped with 6 heated precursor cylinders and 6 plasma gas lines.

Chapter 3

Characterization Methods

3.1 Scanning Electron Microscopy

Scanning electron microscopy (SEM) is one of the most versatile techniques for examination and analysis of surface morphology and chemical composition of materials⁽¹²⁵⁾. In SEM, high-energy electrons interact with a material specimen to generate secondary electrons, back-scattered electrons, Auger electrons, *etc.* These electrons can be collected with specific detectors for imaging or composition analysis. High-energy electrons with an energy level of 0.1-30 keV are generated through electron sources generally composed of tungsten hairpin or lanthanum hexaboride filaments⁽¹²⁵⁾. For a modern SEM instrument, a field emission source is used to produce a stable electron beam with higher current and lower energy dispersion. The generated electron beam is subsequently adjusted and focused by the magnetic field produced by the magnetic lens system.

The image acquisition in SEM depends on detecting various signals from electron-specimen interactions which can be divided into two categories: elastic interaction and inelastic interaction. In elastic interaction, the energy loss of the electrons is negligible during the collision with the specimen atomic nucleus and a large electron deflection angle is accompanied. Backscattered electrons (BSE) is one typical signal due to elastic interaction, which can be used to provide information on both topography and composition. During inelastic interaction, the energy loss of incident electrons occurs due to collision accompanied by a

large energy transfer to the specimen lattice. The created signals are carried by secondary electrons, back-scattered electrons, characteristic X-rays, for example. When incident electrons impinge on the specimen, loosely bound outer shell electrons are ejected from the specimen atoms after receiving sufficient kinetic energy to form secondary electrons⁽¹²⁶⁾. As the incident electrons propagate through the specimen, electron trajectories spread laterally to regions larger than the original incident beam size⁽¹²⁶⁾. This lateral spreading determines the spatial resolutions for different signals in SEM. Less spreading results in higher resolution. Due to inelastic scattering and energy loss, electrons and characteristic X-rays can escape from certain depth below the material surface only, which is referred to as escape depth⁽¹²⁶⁾. As shown in Figure 3.1, the escape depth and spatial resolution vary for different types of signals. Auger electrons have highest spatial resolution, while characteristic X-rays have largest escape depth. Secondary electrons with low kinetic energy (approximately 3-5 eV) possess relatively small escape depth ranging from 5 to 50 nm. They are very sensitive to the surface morphologies of materials and are mainly used to obtain topographic contrast in high resolution⁽¹²⁵⁾. The resolution of the secondary electron image generally determines the highest resolution of the SEM instruments.

Since SEM depends on electron signals for imaging, specimen preparation is required for materials which emit low level of secondary electrons, such as polymeric or bioorganic samples. Coating of other conductive materials (gold, chromium, carbon, titanium, *etc.*) is a common method to improve the image quality. Sputtering is widely used in the coating process, but the coatings prepared via this method are not suitable for polymeric or bioorganic materials with ultra fine nanostructures, because sputtering results in coatings with large grain size (2-6 nm) and nonuniformity which prevent the nanofeatures from being observed by SEM. Additionally, many polymeric or biological samples suffer from damage or deformation under high energy electron beam, thus it is imperative to use coating to protect these materials from electron beam damage^(127,128). Particularly for nanostructured organic materials, a uniform, conformal and ultrathin coating is required. In the thesis, ALD is utilized to achieve a uniform and conformal coating on porous PMMA with inverse nanocolumnar structure for SEM analysis.

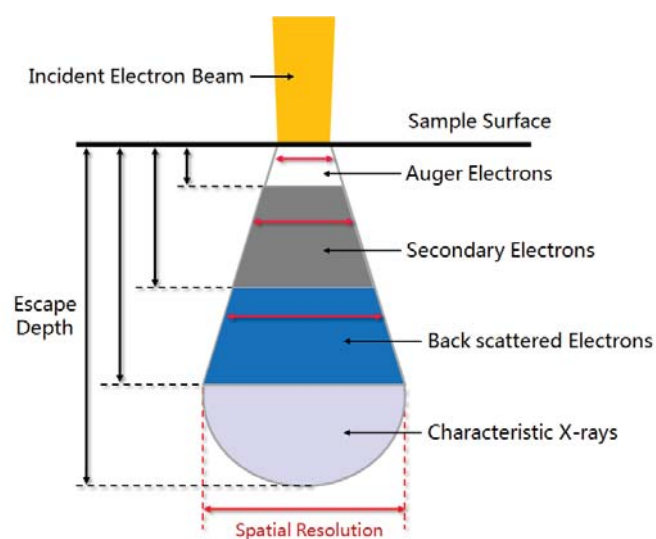


Figure 3.1: Diagram for interaction regions in specimens exposed to high energy electron beam. The vertical and lateral double-headed arrows indicate the escape depths and spatial resolutions for the signals generated at each region. The length of the arrows illustrates the magnitude of the escape depth and spatial resolution. Note that longer lateral arrows denote larger electron spreading and therefore lower resolution.

3.2 Energy Dispersive X-ray Spectroscopy

Energy dispersive X-ray spectroscopy (EDS) utilizes characteristic X-rays emitted during the electron-specimen interactions to provide compositional information on localized areas of the specimens. An incident electron beam bombards a specimen and causes ionization due to a knock-out of an inner shell electrons of the atoms. Another electron transfers from an outer shell down to the inner shell to fill the vacancy and emit X-ray photons. The X-ray energy equals to the energy difference between the two involved electron orbits which is characteristic for each element. The X-ray is detected by the EDS spectrometer to generate a spectrum for chemical composition analysis⁽¹²⁶⁾. In the EDS spectra, the position of the peaks can be used to identify specific elements in the specimen while the peak intensities are generally used to conduct quantitative analysis for the detected elements. The energy of the X-rays measured for EDS analysis generally ranges from 0.1 to 20 keV⁽¹²⁶⁾.

As described above, characteristic X-rays originate from outer shell electrons filling the inner shell vacancies due to the knock-out of inner shell electrons. Electrons occupy different shells with specific energies which are named after capital Roman letters. In an order of increasing distance from the atomic nucleus are K shells, L shells, M shells, N shells. In EDS, the characteristic X-rays are distinguished by a capital Roman letter to indicate the orbits in which the knock-out occurs due to the incident electron bombardment. The Greek letters (α , β , γ) are used to distinguish between energy levels from which the outer shell electrons transit to fill the vacancies. Figure 3.2 illustrates the energy level diagram for an atom and the excitations which induce X-rays with specific energies. Each horizontal line indicates the energy level of an electron state. Normal state corresponds to an atom with no electrons ejected. Knock-out of an electron in each shell increases the energy of the ionized atom to the level of that shell. For instance, ejection of an electron in the K shell increases the energy of the ionized atom to the K level. If an electron in the L shell falls into the vacancy in the K shell, the atom energy decreases to the L level leading to the emission of $K\alpha$ X-ray.

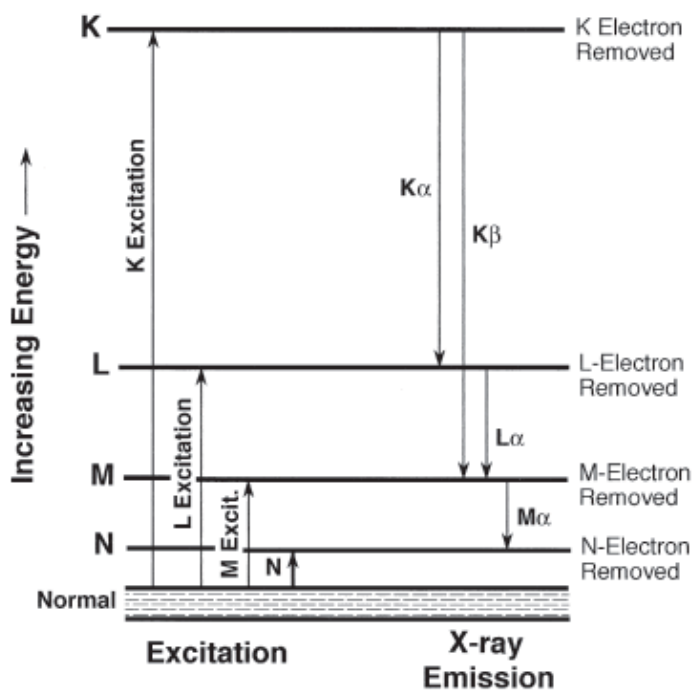


Figure 3.2: Energy level diagram for an atom showing the transitions resulting in different characteristic X-rays. The electrons at K, L, M and N shells are removed and vacant states are created due to the incident electron bombardment (excitation). X-rays such as $K\alpha$, $K\beta$, $L\alpha$ and $M\alpha$ are emitted when the outer shell electrons move into the vacancies. Figure adapted from⁽¹²⁶⁾.

Via measuring the specific energies of the emitted X-rays, particular elements can be determined according to Moseley's law which is expressed as:

$$E = A(Z - C)^2, \quad (3.1)$$

where E denotes the energy (eV) of the X-ray peak, A and C are constants which are specific for each x-ray series, for example, $A = 10.2$ for $K\alpha$ and 1.89 for $L\alpha$, while $C = 1.13$ for $K\alpha$ and 7.4 for $L\alpha$. Hence, Z which is the atomic number of a specific element in the specimens can be determined⁽¹²⁶⁾.

In EDS measurement, X-ray artifacts, such as the escape peaks, stray radiation and sum peaks (pileup peaks), could appear and be wrongly interpreted as characteristic peaks⁽¹²⁵⁾. A sum peak may appear in the EDS spectra when two X-ray photons arrive almost simultaneously. If an X-ray photon arrives at the detector before the signal system finishes processing the preceding photon, the two X-ray photons may be counted as a single photon whose energy is the sum of both X-ray photon energies⁽¹²⁶⁾. For example, if a $K\alpha$ and a $K\beta$ X-ray arrive at the detector simultaneously, a $K\alpha + K\beta$ X-ray could be counted, which can be found at an energy E_{sum} , with $E_{sum} = E_{K\alpha} + E_{K\beta}$ ($E_{K\alpha}$ and $E_{K\beta}$ are the energies of $K\alpha$ and $K\beta$ X-rays, respectively). Sum peaks generally occur at high count rates or when the spectrum is dominated by a single element⁽¹²⁵⁾. Therefore, this X-ray artifact must be considered and corrected in EDS analysis. In the present thesis, sum peaks due to the signals of Si are identified and not assigned to any specific elements.

3.3 Spectroscopic Ellipsometry

3.3.1 General Description

Ellipsometry is an optical characterization method which analyzes the change in the polarization state of a light beam upon reflection from (or transmission through) a sample to determine material properties, such as optical constants, thin film thickness, material composition, *etc.*⁽¹²⁹⁾. In spectroscopic ellipsometry (SE), the spectral-dependent change of the polarization state of the light upon

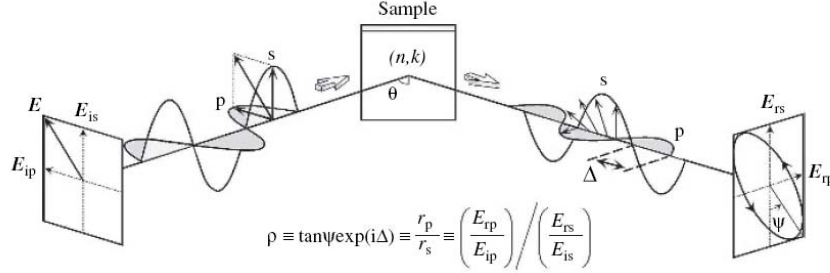


Figure 3.3: The scheme of ellipsometry measurement ⁽¹²⁹⁾.

reflection (or transmission) is measured and analyzed. Figure 3.3 illustrates a typical ellipsometry measurement in reflection configuration. The parallel (p-) and perpendicular (s-) polarized components of the incident light change their polarization state in both amplitude and phase after reflection on a sample. For p-polarized light, the electric field is parallel to the plane of incidence while for s-polarized light the electric field is perpendicular. Standard SE measures two parameters Ψ and Δ which are defined by the following equation:

$$\rho \equiv \tan \Psi \exp(i\Delta) \equiv \frac{r_p}{r_s} \equiv \left(\frac{E_{rp}}{E_{ip}} \right) / \left(\frac{E_{rs}}{E_{is}} \right), \quad (3.2)$$

where r_p and r_s are the Fresnel reflection coefficients, respectively. E_{rp} and E_{rs} denote the complex amplitudes of the reflected p- and s-polarized electrical fields, respectively. E_{ip} and E_{is} are the complex amplitudes of the incident p- and s-polarized electrical fields, respectively ⁽¹²⁹⁾. From Eq. 3.2 we have:

$$\tan \Psi = |r_p|/|r_s|, \quad \Delta = \delta_{rp} - \delta_{rs}. \quad (3.3)$$

here the angle Ψ relates to the amplitude ratio of E_{rp} to E_{rs} while Δ denotes the phase difference between r_p and r_s ⁽¹²⁹⁾.

3.3.2 Jones Matrix and Mueller Matrix

3.3.2.1 Jones Matrix

For completely polarized light, the polarization state can be represented by the Jones Vector which is defined by the electric field vector along x and y directions.

For example, the polarization state of the light traveling in z direction with two electric field components oscillating in x and y directions can be expressed by the Jones vector as follows⁽¹²⁹⁾:

$$\mathbf{E}(z, t) = \exp [i(kz - \omega t)] \begin{bmatrix} E_{x0} \exp (i\delta_x) \\ E_{y0} \exp (i\delta_y) \end{bmatrix}. \quad (3.4)$$

In general, by omitting the term $\exp [i(kz - \omega t)]$ this equation can be simplified to⁽¹²⁹⁾

$$\mathbf{E}(z, t) = \begin{bmatrix} E_{x0} \exp (i\delta_x) \\ E_{y0} \exp (i\delta_y) \end{bmatrix}. \quad (3.5)$$

In ellipsometry, the Jones matrix shown in Eq. 3.6 can be used to represent the sample properties which are responsible for the change of the polarization state of the light after the reflection on a sample. In the equation, the Jones matrix \mathbf{J} connects the incident polarized light (A_p, A_s) and the reflected light (B_p, B_s) . The Jones matrix contains four complex-valued elements. For isotropic materials, only the diagonal elements r_{pp} and r_{ss} of the Jones matrix take nonzero values (r_{pp} and r_{ss} represent the Fresnel reflection coefficients). On the other hand, both the diagonal and the off-diagonal elements of the Jones matrix are nonzero for anisotropic materials. r_{ps} represents the conversion of s-polarization into p-polarization while r_{sp} represents the conversion of p-polarization into s-polarization after reflection.

$$\begin{pmatrix} B_p \\ B_s \end{pmatrix} = J \begin{pmatrix} A_p \\ A_s \end{pmatrix} = \begin{pmatrix} r_{pp} & r_{ps} \\ r_{sp} & r_{ss} \end{pmatrix} \begin{pmatrix} A_p \\ A_s \end{pmatrix}. \quad (3.6)$$

3.3.2.2 Generalized Ellipsometry

In the Jones matrix formalism, a complex reflectance ratio ρ is defined as follows⁽¹³⁰⁾:

$$\rho = \frac{r_{pp} + r_{sp}\chi^{-1}}{r_{ss} + r_{ps}\chi}, \quad (3.7)$$

where r_{pp} , r_{sp} , r_{ss} and r_{ps} are the four Jones matrix elements introduced in Eq. 3.6, $\chi = A_p/A_s$ denotes the ratio of the incident wave amplitude. Six real-valued GE parameters for reflection Ψ_{pp} , Δ_{pp} , Ψ_{ps} , Δ_{ps} , Ψ_{sp} and Δ_{sp} can be defined with the ratios of the four Jones matrix elements⁽¹³⁰⁾:

$$\frac{r_{pp}}{r_{ss}} \equiv R_{pp} = \tan \Psi_{pp} \exp(i\Delta_{pp}), \quad (3.8a)$$

$$\frac{r_{ps}}{r_{pp}} \equiv R_{ps} = \tan \Psi_{ps} \exp(i\Delta_{ps}), \quad (3.8b)$$

$$\frac{r_{sp}}{r_{ss}} \equiv R_{sp} = \tan \Psi_{sp} \exp(i\Delta_{sp}). \quad (3.8c)$$

Thus the complex reflectance ratio ρ can be written by the three GE ratios as follows⁽¹³⁰⁾:

$$\rho = \frac{r_{pp}/r_{ss} + (r_{sp}/r_{ss})\chi^{-1}}{1 + (r_{ps}/r_{pp})(r_{pp}/r_{ss})\chi} = \frac{R_{pp} + R_{sp}\chi^{-1}}{1 + R_{pp}R_{ps}\chi}. \quad (3.9)$$

By definition, ρ is dependent on the polarization state of the incident plane wave represented by χ , which is different from standard ellipsometry^(131,132). However, the six parameters are only sufficient for the non-depolarized light conditions. When the sample or ellipsometer optical components cause light depolarization, the Mueller matrix elements need to be employed to represent the GE data⁽¹³²⁾.

3.3.2.3 Mueller Matrix

The optical response of materials can be also characterized using a 4×4 Mueller matrix descriptive system. In Mueller matrix representation, a Stokes vector composed of four elements is used to describe the polarized or partially polarized light propagating through a material. The four Stokes parameters grouped in the column vector \mathbf{S} are defined as

$$\begin{pmatrix} S_0 \\ S_1 \\ S_2 \\ S_3 \end{pmatrix} = \begin{pmatrix} I_p + I_s \\ I_p - I_s \\ I_{45} - I_{-45} \\ I_R - I_L \end{pmatrix}, \quad (3.10)$$

where I_p , I_s , I_{45} , I_{-45} , I_R and I_L denote the intensities for the p-, s-, +45°, -45°, right-handed and left-handed circularly polarized light components, respectively⁽¹³⁰⁾. The degree of polarization P_χ can be defined as:

$$P_\chi = \frac{\sqrt{S_1^2 + S_2^2 + S_3^2}}{S_0}, \quad (3.11)$$

here P_χ varies from zero to unity. $P_\chi = 1$ for totally polarized light while $P_\chi = 0$ for unpolarized light. For partially polarized light, $0 < P_\chi < 1$. Thereby, the Mueller matrix scheme can be used to describe the propagation of partially polarized light

through the materials. In this description, the Mueller matrix, corresponding to the optical response of material, transforms the input Stokes vector to the output vector by a matrix multiplication:

$$\begin{pmatrix} S_0 \\ S_1 \\ S_2 \\ S_3 \end{pmatrix}_{\text{output}} = \begin{pmatrix} M_{11} & M_{12} & M_{13} & M_{14} \\ M_{21} & M_{22} & M_{23} & M_{24} \\ M_{31} & M_{32} & M_{33} & M_{34} \\ M_{41} & M_{42} & M_{43} & M_{44} \end{pmatrix} \begin{pmatrix} S_0 \\ S_1 \\ S_2 \\ S_3 \end{pmatrix}_{\text{input}}. \quad (3.12)$$

In ellipsometry measurements, the Mueller matrix elements are normalized with respect to M_{11} . The 16 Mueller matrix elements can be divided into two categories: the diagonal and off-diagonal elements. The 4 elements at the upper right corner (M_{13} , M_{14} , M_{23} , M_{24}) and the 4 at lower left corner (M_{31} , M_{32} , M_{41} , M_{42}) are accounted as the off-diagonal Mueller matrix elements, while the other 8 elements are the diagonal Mueller matrix elements.

The Mueller matrix for an isotropic sample is given by⁽¹³⁰⁾:

$$M = \begin{pmatrix} 1 & -N & 0 & 0 \\ -N & 1 & 0 & 0 \\ 0 & 0 & C & S \\ 0 & 0 & -S & C \end{pmatrix}. \quad (3.13)$$

Where N, C and S are related to the ellipsometric parameters Ψ and Δ , which can be expressed as:

$$N = \cos 2\Psi, \quad (3.14a)$$

$$S = \sin 2\Psi \sin \Delta, \quad (3.14b)$$

$$C = \sin 2\Psi \cos \Delta. \quad (3.14c)$$

N, C and S also obey the relation $N^2 + S^2 + C^2 = 1$. As shown in Eq. 3.13, the off-diagonal elements are zero for an isotropic sample. For anisotropic samples only, the off-diagonal elements are nonzero, therefore these elements can be used to study the anisotropic optical properties of the materials. Nevertheless, for anisotropic samples with particular symmetry, these elements become zero in certain measurement configurations^(95,99).

3.3.3 Anisotropic Dielectric Function Tensor

3.3.3.1 Dielectric Function Tensor

In non-cubic materials, the dielectric function can be expressed by a complex-valued second-rank symmetric tensor ε in Cartesian coordinates (x, y, z) :

$$\mathbf{D} = \varepsilon_0(\mathbf{E} + \mathbf{P}) = \varepsilon_0\varepsilon\mathbf{E} = \varepsilon_0 \begin{pmatrix} \varepsilon_{xx} & \varepsilon_{xy} & \varepsilon_{xz} \\ \varepsilon_{xy} & \varepsilon_{yy} & \varepsilon_{yz} \\ \varepsilon_{xz} & \varepsilon_{yz} & \varepsilon_{zz} \end{pmatrix} \mathbf{E}, \quad (3.15)$$

where \mathbf{D} , \mathbf{P} and \mathbf{E} are the displacement, polarization field and electric field, respectively (ε_0 is the vacuum permittivity)⁽¹³¹⁾. \mathbf{D} , \mathbf{P} and \mathbf{E} are given along the unit directions \mathbf{x} , \mathbf{y} , \mathbf{z} as:

$$\mathbf{D} = \mathbf{x}D_x + \mathbf{y}D_y + \mathbf{z}D_z, \quad (3.16a)$$

$$\mathbf{E} = \mathbf{x}E_x + \mathbf{y}E_y + \mathbf{z}E_z, \quad (3.16b)$$

$$\mathbf{P} = \mathbf{x}P_x + \mathbf{y}P_y + \mathbf{z}P_z. \quad (3.16c)$$

3.3.3.2 Rotation Matrix

In order to transform the dielectric function tensor from the Cartesian laboratory coordinate system (x, y, z) to Cartesian auxiliary coordinate system (ξ, η, ζ) , a rotation matrix \mathbf{A} containing three (real-valued) Euler angles can be used such that:

$$\varepsilon(x, y, z) = \mathbf{A}\varepsilon(\xi, \eta, \zeta)\mathbf{A}^{-1}, \quad (3.17)$$

where the unitary matrix \mathbf{A} ($A^{-1} = A^T$, T denotes the transpose of a matrix) is an orthogonal rotation matrix defined as:

$$\mathbf{A} = \begin{pmatrix} \cos \psi \cos \varphi - \cos \theta \sin \varphi \sin \psi & -\sin \psi \cos \varphi - \cos \theta \sin \varphi \sin \psi & \sin \theta \sin \varphi \\ \cos \psi \cos \varphi + \cos \theta \sin \varphi \sin \psi & -\sin \psi \cos \varphi + \cos \theta \sin \varphi \sin \psi & -\sin \theta \cos \varphi \\ \sin \theta \sin \psi & \sin \theta \cos \psi & \cos \theta \end{pmatrix}, \quad (3.18)$$

where φ , θ and ψ are the three Euler angles for the rotation⁽¹³¹⁾. The rotation procedure is depicted in Fig. 3.4. In applying the rotation matrix, firstly the coordinate is rotated by φ around the z-axis; subsequently the system is rotated by θ around the new x-axis; finally the system is rotated by ψ around the ζ -axis to become the Cartesian auxiliary coordinate system (ξ, η, ζ) .

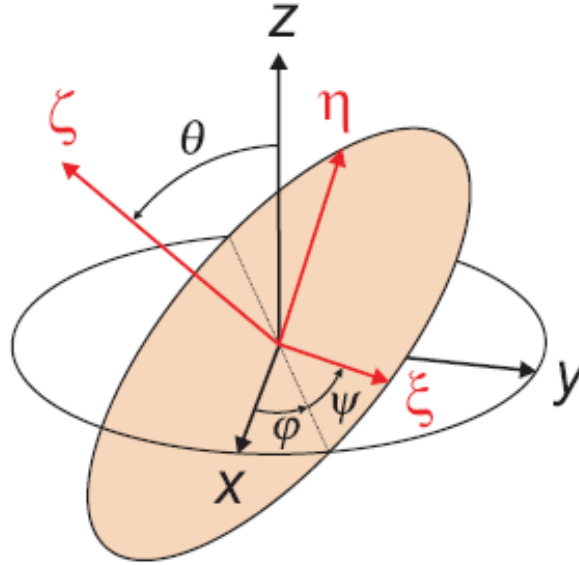


Figure 3.4: Definition of the Euler angles φ , θ and ψ and the orthogonal rotations as provided by the rotation matrix \mathbf{A} . (x, y, z) and (ξ, η, ζ) are the Cartesian laboratory coordinate system and the Cartesian auxiliary coordinate system, respectively⁽¹³¹⁾.

3.3.3.3 Bond Polarizability Model

The intrinsic bond polarizations establish a spatial non-Cartesian (monoclinic or triclinic) or Cartesian (orthorhombic, tetragonal, hexagonal, trigonal, or cubic) center-of-gravity system, with axes described by vectors $\mathbf{a} = \mathbf{x}a_x + \mathbf{y}a_y + \mathbf{z}a_z$, $\mathbf{b} = \mathbf{x}b_x + \mathbf{y}b_y + \mathbf{z}b_z$ and $\mathbf{c} = \mathbf{x}c_x + \mathbf{y}c_y + \mathbf{z}c_z$ ⁽¹³¹⁾. The dielectric polarization can be described by linear superposition of polarizations along the unit axes \mathbf{a} , \mathbf{b} and \mathbf{c} :

$$\mathbf{P} = \mathbf{P}_a + \mathbf{P}_b + \mathbf{P}_c, \quad (3.19)$$

with

$$\mathbf{P}_a = \varrho_a(\mathbf{aE})\mathbf{a}, \quad (3.20a)$$

$$\mathbf{P}_b = \varrho_b(\mathbf{bE})\mathbf{b}, \quad (3.20b)$$

$$\mathbf{P}_c = \varrho_c(\mathbf{cE})\mathbf{c}. \quad (3.20c)$$

where ϱ_a , ϱ_b and ϱ_c are the complex-valued scalar major polarizabilities along each unit axis⁽¹³¹⁾, and \mathbf{a} , \mathbf{b} and \mathbf{c} are referred as the major polarizability axes. The three major polarizabilities obey Kramers-Kronig relation and exhibit dependence on the photon energy $\hbar\omega$. The corresponding part of the (symmetric) dielectric function tensor ε can be related to the three major polarizabilities as follows:

$$\varepsilon_{xx} = 1 + a_x a_x \varrho_a + b_x b_x \varrho_b + c_x c_x \varrho_c, \quad (3.21a)$$

$$\varepsilon_{xy} = a_x a_y \varrho_a + b_x b_y \varrho_b + c_x c_y \varrho_c, \quad (3.21b)$$

$$\varepsilon_{xz} = a_x a_z \varrho_a + b_x b_z \varrho_b + c_x c_z \varrho_c, \quad (3.21c)$$

$$\varepsilon_{yy} = 1 + a_y a_y \varrho_a + b_y b_y \varrho_b + c_y c_y \varrho_c, \quad (3.21d)$$

$$\varepsilon_{yz} = a_y a_z \varrho_a + b_y b_z \varrho_b + c_y c_z \varrho_c, \quad (3.21e)$$

$$\varepsilon_{zz} = 1 + a_z a_z \varrho_a + b_z b_z \varrho_b + c_z c_z \varrho_c. \quad (3.21f)$$

with $\varepsilon_{ij} = \varepsilon_{ji}$ ($i \neq j$)⁽¹³¹⁾.

For materials in Cartesian systems (orthorhombic, tetragonal, hexagonal, trigonal and cubic systems), a rotation matrix \mathbf{A} independent of the wavelength can be found such that ε has a diagonal form in the coordinate system (ξ, η, ζ) :

$$\varepsilon = \mathbf{A} \begin{pmatrix} \varepsilon_a & 0 & 0 \\ 0 & \varepsilon_b & 0 \\ 0 & 0 & \varepsilon_c \end{pmatrix} \mathbf{A}^{-1}, \quad (3.22)$$

where ε_a , ε_b , and ε_c are the dielectric functions in the major polarizability axis system (a, b, c) and $\varepsilon_j = 1 + \varrho_j$ ($j = a, b, c$)⁽¹³¹⁾. The diagonal tensor in the equation above represents the dielectric properties of different crystal systems. For example, for an isotropic system $\varepsilon_a = \varepsilon_b = \varepsilon_c$. In this case, ε is a scalar. For uniaxial materials with tetragonal, hexagonal and trigonal symmetry, ε is composed of one out-of-plane component ε_c along \mathbf{c} axis and two identical in-plane components $\varepsilon_a = \varepsilon_b$ along the other two axes. For biaxial materials with orthorhombic symmetry $\varepsilon_a \neq \varepsilon_b \neq \varepsilon_c$.

For biaxial materials in non-Cartesian systems such as monoclinic and triclinic systems, an additional projection matrix \mathbf{U} is required to compose a virtual orthogonal basis such that ε has a diagonal form in the coordinate system $(a, b,$

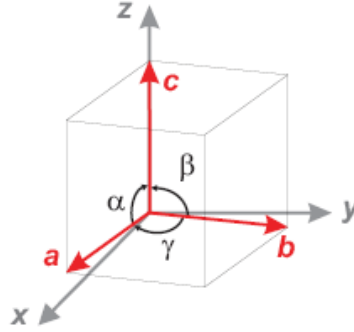


Figure 3.5: Definition of α , β and γ . The scheme depicts a crystallographic unit cell with the major axes \mathbf{a} , \mathbf{b} and \mathbf{c} . α , β and γ are the angles between \mathbf{a} , \mathbf{b} and \mathbf{c} . For example, with monoclinic symmetry, $\varepsilon_a \neq \varepsilon_b \neq \varepsilon_c$ and $\beta \neq \alpha = \gamma = 90^\circ$; with triclinic symmetry, $\varepsilon_a \neq \varepsilon_b \neq \varepsilon_c$ and $\alpha \neq \beta \neq \gamma \neq 90^\circ$ ⁽¹⁰⁷⁾.

c):

$$\varepsilon = \mathbf{A}\mathbf{U} \begin{pmatrix} \varepsilon_a & 0 & 0 \\ 0 & \varepsilon_b & 0 \\ 0 & 0 & \varepsilon_c \end{pmatrix} \mathbf{U}^T \mathbf{A}^T, \quad (3.23)$$

and \mathbf{U} takes the form as follows⁽¹³³⁾:

$$\mathbf{U} = \begin{pmatrix} \sin \alpha & (\cos \gamma - \cos \alpha \cos \beta)(\sin \alpha)^{-1} & 0 \\ 0 & (1 - \cos^2 \alpha - \cos^2 \beta - \cos^2 \gamma + 2 \cos \alpha \cos \beta \cos \gamma)^{\frac{1}{2}}(\sin \alpha)^{-1} & 0 \\ \cos \alpha & \cos \beta & 1 \end{pmatrix}, \quad (3.24)$$

where α , β and γ are the internal angles between the major polarizability axes \mathbf{a} , \mathbf{b} and \mathbf{c} . $\beta \neq \alpha = \gamma = 90^\circ$ can be found for monoclinic system with β being the monoclinic angle, while $\alpha \neq \beta \neq \gamma \neq 90^\circ$ holds for triclinic system. Obviously, $\alpha = \beta = \gamma = 90^\circ$ is valid for materials in a cubic, uniaxial or orthorhombic system, and \mathbf{U} becomes a diagonal 3×3 identity matrix. As shown in Figure 3.5, \mathbf{c} axis is chosen to coincide with the z-axis while \mathbf{a} axis is located within the x-z plane. For instance, the dielectric tensor ε_m of a monoclinic system is expressed as follows⁽¹⁰⁷⁾:

$$\varepsilon_m = \mathbf{U} \begin{pmatrix} \varepsilon_a & 0 & 0 \\ 0 & \varepsilon_b & 0 \\ 0 & 0 & \varepsilon_c \end{pmatrix} \mathbf{U}^T = \begin{pmatrix} 1 + \varrho_a & 0 & 0 \\ 0 & 1 + \sin^2 \beta \varrho_b & \sin \beta \cos \beta \varrho_b \\ 0 & \sin \beta \cos \beta \varrho_b & 1 + \cos^2 \beta \varrho_b + \varrho_c \end{pmatrix}, \quad (3.25)$$

where ϱ_a , ϱ_b and ϱ_c are the polarizability along each axis \mathbf{a} , \mathbf{b} and \mathbf{c} , β is the internal angle between axes \mathbf{b} and \mathbf{c} . The dielectric tensor ε_t of a triclinic system is given as follows⁽¹⁰⁷⁾:

$$\varepsilon_t = \begin{pmatrix} \varrho_a \sin^2 \alpha + \varrho_b \frac{1}{\sin^2 \alpha} \Gamma^2 & \varrho_b \frac{1}{\sin^2 \alpha} \Gamma \Lambda & (\varrho_a + \varrho_b \frac{1}{\sin^2 \alpha} \Gamma) \sin \alpha \cos \beta \\ \varrho_b \frac{1}{\sin^2 \alpha} \Gamma \Lambda & -\varrho_b \frac{1}{\sin^2 \alpha} \Upsilon & -\varrho_b \frac{1}{\sin \alpha} \cos \beta \Lambda \\ (\varrho_a + \varrho_b \frac{1}{\sin^2 \alpha} \Gamma) \sin \alpha \cos \beta & -\varrho_b \frac{1}{\sin \alpha} \cos \beta \Lambda & \varrho_a \cos^2 \alpha + \varrho_a \cos^2 \beta + \varrho_c \end{pmatrix}, \quad (3.26)$$

with

$$\Gamma = -\cos \alpha \cos \beta \cos \gamma + \cos \gamma, \quad (3.27a)$$

$$\Lambda = (-\cos^2 \alpha - \cos^2 \beta + 2 \cos \alpha \cos \beta \cos \gamma + \sin^2 \gamma)^{\frac{1}{2}}, \quad (3.27b)$$

$$\Upsilon = \cos^2 \alpha + \cos^2 \beta - 2 \cos \alpha \cos \beta \cos \gamma + \cos^2 \gamma - 1. \quad (3.27c)$$

For monoclinic and triclinic systems, the rotation matrix \mathbf{A} used to diagonalize ε in the coordinate system (a, b, c) (as shown in Eq. 3.23) becomes wavelength-dependent, because the matrices in Eq. 3.25 and 3.26 contain wavelength-dependent entries $\varrho_a(\omega)$, $\varrho_b(\omega)$ and $\varrho_c(\omega)$. Therefore, in order to determine the optical properties of monoclinic and triclinic systems, the measured GE data must be analyzed in a wide spectral range, and wavelength-independent Euler angles (φ , θ and ψ) must be found⁽¹⁰⁷⁾. Table 3.1 summarizes the symmetries and dielectric tensor properties of different crystal systems presented above⁽¹³⁰⁾.

3.3.4 Generalized Ellipsometry Modeling Approaches for Sculptured Thin Films

3.3.4.1 Homogeneous Biaxial Layer Approach

The homogeneous biaxial layer approach (HBLA) is used to model the optical response of anisotropic composite materials. The model assumes the investigated materials to be homogeneous and possess biaxial optical properties which can be described by a dielectric function tensor. This diagonal tensor comprises of three

Table 3.1: Symmetries and dielectric tensor properties of symmetrically dielectric materials

Symmetry	Crystal systems	Dielectric tensor	Internal angles
Isotropic	Cubic	$\varepsilon_a = \varepsilon_b = \varepsilon_c$	$\alpha = \beta = \gamma = 90^\circ$
Uniaxial	Trigonal	$\varepsilon_a = \varepsilon_b \neq \varepsilon_c$	$\alpha = \beta = \gamma = 90^\circ$
	Tetragonal		
	Hexagonal		
Biaxial	Orthorhombic	$\varepsilon_a \neq \varepsilon_b \neq \varepsilon_c$	$\alpha = \beta = \gamma = 90^\circ$
	Monoclinic		$\beta \neq \alpha = \gamma = 90^\circ$
	Triclinic		$\alpha \neq \beta \neq \gamma \neq 90^\circ$

effective dielectric functions in the major polarizability axes **a**, **b** and **c** as shown in Eq. 3.22.

When used to model the optical response of SCTFs, HBLA considers SCTF to be a biaxial layer with **c** along the long axis of the nanocolumns^(95,99,100). The Euler angles φ , θ and ψ are employed in the HBLA to determine the orientation of the film. The internal angles α , β and γ in the model determine the orientation of the three major axes to differentiate different optical systems, such as orthorhombic, monoclinic and triclinic systems. The anisotropic optical properties of SCTFs are represented by different sets of effective dielectric function along each axis. Due to the porosity within SCTFs, other materials such as polymers can be used to be infiltrated into the voids to form composite materials. Similarly, the HBLA is applied to consider such hybridized SCTFs to be biaxial with **c** axis along the nanocolumns⁽¹³⁴⁾. Although the shape of the nanocolumns and constituent fractions within SCTFs are not determined, the HBLA has the following advantages over other effective medium approximation approaches⁽¹³⁵⁾. First, the HBLA is a simple method with few model assumptions. No initial knowledge of the optical constants of each constituents or material fractions are required in this model. Secondly, it is valid for both absorbing and non-absorbing ma-

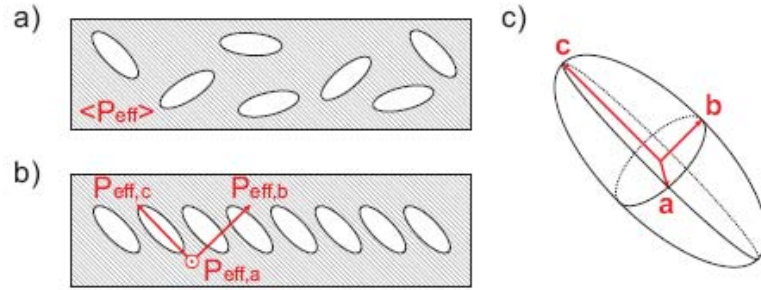


Figure 3.6: Scheme of AB-EMA: (a) the inclusions randomly distributed in the host medium with an isotropic effective polarizability; (b) the inclusions orderly distributed in the host medium with three effective polarizabilities; (c) the individual elliptical inclusions⁽¹¹⁵⁾.

terials. Thirdly, it shows no dependence on the structure size. This approach is valid since the dimensions and nanocolumnar diameters are much smaller than the probing wavelength⁽¹³⁵⁾. The HBLA is generally considered as a primary method to describe the optical biaxial behaviors of SCTFs with or without infiltration. The pristine results, namely the effective biaxial dielectric functions obtained by the HBLA, can be used as target data for other effective medium approximation approaches⁽¹³⁴⁾.

3.3.4.2 Anisotropic Bruggeman Effective Medium Approximation

In order to obtain the constituent fractions of SCTFs and SCTFs with infiltration, the anisotropic Bruggeman effective medium approximation (AB-EMA) has been employed to analyze the GE data measured from the materials^(94,96,101–105). In the AB-EMA, SCTFs are assumed to be composite materials with the nanocolumns considered as highly oriented inclusions in the host medium (air or infiltration)^(101,102). As illustrated in Fig. 3.6, with the ellipsoidal inclusions randomly distributed in the host material, the composite exhibits an isotropic effective polarizability, while the polarizability becomes biaxial with the inclusions orderly distributed in the host medium. Two formalisms of AB-EMA have been described, which differ in the calculation of the depolarization factors. The first formalism is referred to

here as traditional AB-EMA (TAB-EMA). In the TAB-EMA, the effective dielectric functions along the three major axes **a**, **b** and **c** for a composite with n components are expressed as^(101,102):

$$\sum_{i=1}^n f_i \frac{\varepsilon_i - \varepsilon_{\text{eff},j}}{\varepsilon_{\text{eff},j} + L_j(\varepsilon_i - \varepsilon_{\text{eff},j})} = 0, \quad j = a, b, c, \quad (3.28)$$

where ε_i and f_i denote the bulk dielectric function and volume fraction of the i^{th} component of the composite, respectively, $\varepsilon_{\text{eff},j}$ represents the effective dielectric function along the three major axes **a**, **b** and **c**. L_a , L_b , L_c are the three depolarization factors along **a**, **b** and **c**. The three depolarization factors are defined as follows⁽¹³⁵⁾:

$$L_j = \frac{U_a U_b U_c}{2} \int_0^\infty ds \frac{1}{(s + U_j^2) \sqrt{(s + U_a^2)(s + U_b^2)(s + U_c^2)}}, \quad j = a, b, c, \quad (3.29)$$

where U_j is the real valued shape parameter for the ellipsoidal inclusions, the two ratios U_a/U_c and U_b/U_c define the inclusion shape exactly⁽¹³⁵⁾. The sum of the three depolarization factors must follow^(101,102):

$$L_a + L_b + L_c = 1, \quad (3.30)$$

with

$$0 \leq L_j \leq 1, \quad j = a, b, c. \quad (3.31)$$

In this formalism, the depolarization factors are only related with shape of the inclusions. For instance, $L_a = L_b = L_c = 1/3$ for spherical inclusions. For the prolate spheroidal inclusions oriented along the substrate normal, $L_a = L_b = 0.5$ and $L_c = 0$.

The second formalism, referred to here as rigorous AB-EMA (RAB-EMA) takes the form of⁽¹³⁶⁾:

$$\sum_{i=1}^n f_i \frac{\varepsilon_i - \varepsilon_{\text{eff},j}}{1 + D_j(\varepsilon_i - \varepsilon_{\text{eff},j})} = 0, \quad j = a, b, c, \quad (3.32)$$

with the depolarization factors D_j specified by the double integrals:

$$D_a = \frac{1}{4\pi} \int_0^{2\pi} d\phi \int_0^\pi d\theta \frac{\sin^3 \theta \cos^2 \phi}{U_a^2 \rho_D}, \quad (3.33a)$$

$$D_b = \frac{1}{4\pi} \int_0^{2\pi} d\phi \int_0^\pi d\theta \frac{\sin^3 \theta \sin^2 \phi}{U_b^2 \rho_D}, \quad (3.33b)$$

$$D_c = \frac{1}{4\pi} \int_0^{2\pi} d\phi \int_0^\pi d\theta \frac{\sin \theta \cos^2 \theta}{U_c^2 \rho_D}. \quad (3.33c)$$

which involve the scalar parameter

$$\rho_D = \frac{\sin^2 \theta \cos^2 \phi}{U_a^2} \varepsilon_{\text{eff},a} + \frac{\sin^2 \theta \sin^2 \phi}{U_b^2} \varepsilon_{\text{eff},b} + \frac{\cos^2 \theta}{U_c^2} \varepsilon_{\text{eff},c}. \quad (3.34)$$

In the RAB-EMA, the depolarization factor D_j along each axis is a function of the effective permittivities $\varepsilon_{\text{eff},j}$ as well as the shape of the inclusion. Since the depolarization factors are coupled to the effective permittivities, numerical methods are required to obtain D_j and $\varepsilon_{\text{eff},j}$. In addition, the depolarization factors are complex numbers in a lossy medium and are wavelength-dependent.

3.3.5 Ellipsometry Data Analysis

Since ellipsometry is an indirect characterization method, a data analysis procedure involving the use of physical models is required to determine the sample properties. A regression analysis is performed to match the model-calculated data to the experimental data as close as possible by varying the model parameters. The mean square error (MSE) function is minimized during the analysis to reach the best match. In the present thesis, GE in Mueller matrix formalism is utilized to analyze the structural and optical properties of the anisotropic samples. Mueller matrix elements were measured at multiple sample orientations. Different data analysis procedures are used to obtain sample properties including dielectric function tensor, optical symmetry and structural properties.

3.3.5.1 Wavelength-by-Wavelength Analysis

Wavelength-by-wavelength fits (also referred as point-by-point fits) are performed to extract the dielectric function from the experimental data at each wavelength⁽¹³¹⁾. The dielectric function of a particular layer with known thickness is varied at each wavelength to match the model-calculated data to the experimental data as close as possible. The dielectric constants at each wavelength are independent of each

other. The dielectric function from wavelength-by-wavelength fits needs further fitting with parameterized model dielectric function to maintain the Kramers-Kronig consistency and obtain physical parameters (such as critical point energies and broadening parameters)⁽¹⁰⁷⁾.

3.3.5.2 Parameterized Model Dielectric Function Analysis

Parameterized model dielectric function (MDF) fits are employed to extract the dielectric function which obeys the Kramers-Kronig consistency, and to obtain physical parameters of interest. In this analysis, physical lineshape models (such as Lorentzian and Drude models) are utilized and the parameters in the models are varied to match the model-calculated data to the experimental data as close as possible for the entire spectral range. Generally, this procedure is performed after the wavelength-by-wavelength analysis. Physical lineshape models are firstly used to fit the dielectric function obtained from the wavelength-by-wavelength analysis. Based on the results of the initial fit, the parameters in physical lineshape models are varied to fit the experimental data. MDF analysis can prevent the wavelength-by-wavelength random measurement errors from becoming a part of the dielectric function, and greatly reduce the number of free parameters⁽¹³¹⁾. In the present thesis, mainly two physical models are utilized: Lorentzian and Drude models.

3.3.5.3 Ellipsometry Test Functions

During the data analysis procedure, model parameters are varied to match the model-calculated data to the experimental data as close as possible, which is referred to as the best-model calculation. A Levenberg-Marquardt algorithm can be used to vary the model parameters to reach the closest match by minimizing the weighted test function (mean square error, MSE)⁽¹³⁷⁾. For standard ellipsometry, the weighted test function ξ_{SE} is given by⁽¹³¹⁾:

$$\xi_{SE}^2 = \frac{1}{2S - K + 1} \sum_{i=1}^S \left[\left(\frac{\Psi_i - \Psi_i^c}{\sigma_i^\Psi} \right)^2 + \left(\frac{\Delta_i - \Delta_i^c}{\sigma_i^\Delta} \right)^2 \right], \quad (3.35)$$

where S denotes the number of measured data pairs (Ψ_i and Δ_i), σ_i^Ψ and σ_i^Δ are their standard deviations obtained in the measurements, K is the number of

real-valued fit parameters, Ψ_i^c and Δ_i^c are the calculated ellipsometric parameters at the photon energy $E = \hbar\omega_i$ ⁽¹³⁸⁻¹⁴⁰⁾.

For the GE situation where Mueller matrix elements M_{ij} are involved, the weighted test function ξ_{ME} is given by⁽¹³¹⁾:

$$\xi_{ME}^2 = \frac{1}{JS - K + 1} \sum_{i=1}^S \sum_{l=1}^J \left(\frac{M_{il} - M_{il}^c}{\sigma_{il}^{M_{il}}} \right)^2, \quad (3.36)$$

where S denotes the number of wavelengths at which the data are measured, J denotes the number of individual Mueller matrix elements, and K is the number of fit parameters. M_{il} and M_{il}^c are the experimental and model calculated data, respectively. $\sigma_{il}^{M_{il}}$ is the corresponding standard deviations. Note that the MSE in GE for anisotropic samples can not be compared directly to the one in standard ellipsometry for isotropic samples. The experimental data sets in GE are measured at multiple sample orientations and are generally much larger than those in standard ellipsometry. GE data analysis requires a best match of the model-calculated data to the experimental data not only in the investigated spectral range, but also versus sample orientations and angle of incidence⁽¹⁰⁷⁾.

If the dielectric functions are used as target data to be analyzed, the weighted test function ξ_ε is given by:

$$\xi_\varepsilon^2 = \frac{1}{3S - K} \sum_{j=1}^S \sum_{k=0}^2 \left(\frac{\varepsilon_{k,j} - \varepsilon_{k,j}^c}{\sigma_j^{\varepsilon_k}} \right)^2, \quad (3.37)$$

where S denotes the number of wavelengths, K is the number of fit parameters, $\varepsilon_{k,j}$ and $\varepsilon_{k,j}^c$ are the target and model calculated dielectric functions, respectively. $\sigma_j^{\varepsilon_k}$ is the generated standard deviations with $\sigma_j^{\varepsilon_k} = 0.01\varepsilon_{k,j}$ ⁽¹³⁵⁾.

During the data analysis, the correlations may exist between different adjusted model parameters. The curvature matrix α used to derive the correlation is given by⁽¹⁰⁷⁾:

$$\alpha_{kl} = \sum_{j=1}^N \left(\frac{1}{\sigma_{\Psi_j}^2} \frac{\delta \Psi_j^C \delta \Psi_j^C}{\delta \alpha_k \delta \alpha_l} + \frac{1}{\sigma_{\Delta_j}^2} \frac{\delta \Delta_j^C \delta \Delta_j^C}{\Delta \alpha_k \Delta \alpha_l} \right). \quad (3.38)$$

The covariance matrix \mathbf{C} is the inverse of α with $\mathbf{C} = \alpha^{-1}$. The correlation coefficients η_{jk} can be obtained from \mathbf{C} by:

$$\eta_{jk} = \frac{C_{jk}}{\sqrt{C_{jj}}\sqrt{C_{kk}}}, \quad (3.39)$$

with $-1 \leq \eta_{jk} \leq 1$. Higher value of η_{jk} indicates larger correlation between the j th and k th model parameters. High value of η_{jk} should be avoided to obtain a correct and unique analysis. As mentioned in Sect. 3.3.5.2, using MDF analysis to reduce the model parameters is an effective method to lower the η_{jk} value. In GE, the analysis of an anisotropic sample is performed at multiple sample orientations and angles of incidence, which also reduces the parameter correlation.

Another important factor in the data analysis is the confidence limit of the individual model parameter. The standard 90% confidence limit L for the j th parameter is given by⁽¹⁰⁷⁾:

$$L_j = \pm 1.65\sqrt{C_{jj}}\xi, \quad (3.40)$$

where 1.65 is a statistically derived constant, ξ is the MSE. Lower value of L indicates higher accuracy for the obtained parameter. The error bar (uncertainty) in the modeling result of the present thesis is the confidence limit for each model parameter.

Chapter 4

Experiment

4.1 Material Fabrication

4.1.1 Fabrication of Permalloy SCTFs Infiltrated with Polymer

The permalloy SCTFs were grown by GLAD on a n-type silicon (Si) substrate. The source material for deposition was composed of 81 wt% Ni and 19 wt% Fe (SCM, Inc.). A typical deposition was conducted at a deposition angle of 85° measured between the incident flux direction and substrate normal and a deposition rate of approximately 3 \AA/s measured by a QCM deposition controller positioned normal to the incident flux. The deposition time was approximately 14 min. The pressure during the deposition was maintained at 10^{-9} mbar.

The infiltration process was conducted by spin-coating 2.5 wt% of PMMA (Sigma-Aldrich) dissolved in toluene onto the as-deposited SCTFs. The spin-coating process was performed at 3000 rpm for 60 s. After spin-coating, the permalloy SCTFs infiltrated with PMMA (hybridized SCTFs) were baked in a convection oven at 165°C for 1 h. Prior to the infiltration experiments, a PMMA layer spin-coated on a Si substrate was baked at 165°C for 1 h and measured with an ellipsometer to obtain the optical constants using a Cauchy optical parameter model.

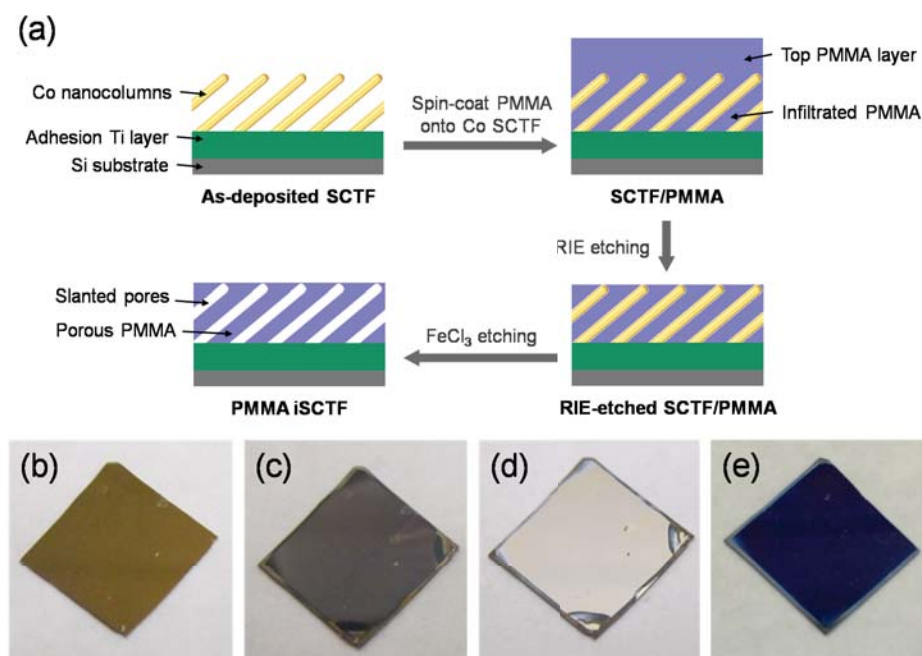


Figure 4.1: The scheme in (a) depicts the preparation process for PMMA iSCTFs. The photographs of samples are: (b) the as-deposited Co SCTF; (c) the Co SCTF coated with PMMA after RIE; (d) the PMMA iSCTF after FeCl_3 wet etching; (e) a 90 nm solid PMMA film spin-coated on Si substrate. The size of all samples is approximately $1\text{cm} \times 1\text{cm}$.

4.1.2 Fabrication of Porous PMMA Thin Films with Inverse SCTF Structure

Fig. 4.1(a) depicts the preparation process for a typical sample of porous PMMA thin films with inverse SCTF structure (PMMA iSCTFs). First, an adhesion titanium (Ti) layer with a thickness of approximately 30 nm was deposited on a n-type silicon (Si) substrate with a 2 nm native oxide layer, followed by a GLAD growth of Co SCTF. The Ti deposition was conducted with the incident particle flux direction normal to the substrate. The deposition rate was approximately 1.5 \AA/s measured at normal incidence. The source material for deposition was Ti pellets (K. J. Lesker, Inc.) with a purity of 99.99%. Co SCTFs were deposited

at a deposition angle of 85° and a deposition rate ranged between 3 and 4 $\text{\AA}/\text{s}$ for approximately 10 min (pressure at 10^{-9} mbar). Co pellets (K. J. Lesker, Inc.) with a purity of 99.95% were used as source material for the deposition.

Subsequently, 2.5 wt% of PMMA dissolved in toluene was spin-coated onto the as-deposited SCTF at a spinning speed of 3000 rpm for 60 s. The Co SCTF spin-coated with PMMA was baked in a convection oven at 165°C for 1 h.

Reactive ion etching (RIE) was utilized to etch away the extra PMMA layer on the top of Co SCTF after spin-coating. The etching was performed using a flow of 50 sccm sulfur hexafluoride (SF_6) at a chamber pressure of 50 mT and a RIE power of 200 W. A 110 nm PMMA layer spin-coated on Si substrate was etched under the same conditions to test the etching rate. The PMMA sample was cleaved into four parts which were etched for 30 s, 45 s, 60 s and 90 s, respectively. The thickness changes for the four samples were measured with an ellipsometer to determine an averaged etching rate of approximately 90 nm/min. This rate was used to determine the etching time for removing the top PMMA layer of Co SCTF coated with PMMA. Typically, an etching time of 15 s was used to remove the top PMMA layer.

After RIE, the Co SCTF was selectively removed by submersion into an aqueous iron chloride (FeCl_3) solution (1 M) for 30 s and rinsed with deionized water. The obtained PMMA iSCTF was then dried in a convection oven at 60°C for 2 h.

Figs. 4.1(b), (c) and (d) show the photographs of the samples at different preparation steps. A 90 nm solid PMMA film spin-coated on Si substrate was shown in Fig. 4.1(e) for comparison. In Fig. 4.1(d), the color of the sample is changed significantly after FeCl_3 etching, indicative of change of composition and optical properties due to etching. The PMMA iSCTF shows good transparency such that the Si substrate is visible, and differs from the color appearance of a solid nonporous PMMA film in Fig. 4.1(e).

4.2 Material Characterization

4.2.1 GE Measurements

Spectroscopic Mueller matrix GE measurements were performed with a commercial ellipsometer (M-2000VI, J. A. Woollam Co., Inc.). The ellipsometer is capable of measuring samples from visible to near-infrared range and adapts an optical configuration of PC_RSA_R (polarizer-rotating compensator-sample-rotating analyzer) which allows for the measurement of 11 out of 16 Mueller matrix elements normalized to M_{11} (except for elements in the fourth row)⁽¹³⁰⁾. A 50 W halogen lamp is used as the light source for the instrument. The sample is mounted on an automatic horizontal stage which enables the sample azimuth (ϕ) rotation during measurements. The light reflected from the samples passes through the rotating analyzer and is detected by two CCD arrays. One CCD array detects 390 wavelengths in the spectral range from 370 to 1000 nm and the other detects 200 wavelengths in the range from 1000 to 1690 nm.

GE measurements were conducted on the as-deposited SCTFs, SCTFs infiltrated with PMMA and PMMA iSCTFs. During the measurements, two focusing probes were attached to the light source and detector optics units, respectively. The spot size of the probing light beam on the samples is approximately 500 μm in diameter. The angle of incidence Φ_a was varied from 45° to 75° in steps of 10° and at each Φ_a the sample azimuth angle ϕ was rotated from 0° to 360° in steps of 6°.

4.2.2 SEM Measurements

The SEM images were obtained using a field-emission SEM (Nova NanoSEM 450, FEI). The highest resolution with an acceleration voltage of 1 kV is 1.4 nm. SEM images are taken using an acceleration voltage of 2 kV and a working distance of 2-3 mm. Secondary electron images are used in the present thesis. During SEM measurements, samples were fixed on the sample stages with carbon tapes. For the cross-section SEM images, the samples were carefully cleaved and mounted

on a sample holder with the sample cross-section facing directly to the incident electron beam.

Typically, a 50 nm Ti layer was deposited on the permalloy SCTF infiltrated with PMMA via GLAD to protect the polymer from electron beam damage and improve the contrast in the SEM image. The deposition was performed at normal flux incidence with a deposition rate of approximately 1.5 Å/s.

Metal and oxide coatings were deposited on PMMA iSCTFs with two methods to protect the polymer during SEM experiments. For a typical top-view SEM image, a 8 nm Ti thin layer was deposited on the PMMA iSCTF by GLAD. The deposition was performed at normal flux incidence with a rate of approximately 1.5 Å/s. For the cross-sectional SEM image, a thin layer of aluminum oxide (Al_2O_3) was coated conformally on the PMMA iSCTF using ALD. During the ALD process, a thermal Al_2O_3 process of 55 cycles was conducted at 80 °C to grow approximately 5 nm oxide layer. The two reactants used for the Al_2O_3 growth were trimethylaluminum and nanopure water. In each cycle, the pulse time for each reactant was 60 ms and the following purge time was 40 s.

4.2.3 EDS Measurements

Energy dispersive X-ray spectroscopy (EDS) spectra of Co SCTFs and PMMA iSCTFs coated with Al_2O_3 were measured with an EDS spectrometer (Oxford Instruments) attached to the SEM system operating at 15 kV. A silicon drift detector (X-Max^N Silicon Drift Detector, OXFORD INSTRUMENTS) is used to detect the characteristic X-rays. The samples were mounted on the sample stage with the thin film surface facing up to the incident electron beam. EDS analysis software INCA was utilized to analyze the EDS spectra to obtain the chemical compositions of our samples.

Chapter 5

Generalized Ellipsometry Analysis Approach for Porous Slanted Columnar Thin Films Infiltrated with Polymer

5.1 GE Data Analysis Procedure

In the beginning of our analysis approach, the experimental Mueller matrix element data are analyzed using the HBLA model, with an assumption that the thin film samples are homogeneous and biaxial. The optical models used to analyze the experimental data of as-deposited permalloy SCTFs and permalloy SCTFs infiltrated with PMMA (hybridized SCTFs) are shown schematically in Fig. 5.1. For permalloy SCTF, the stratified optical model comprises an isotropic Si substrate and a biaxial HBLA layer which accounts for the dielectric response of the SCTF. For the hybridized SCTF, the model consists of a Si substrate, an HBLA layer and a top isotropic PMMA layer. The orientation of the major polarizability axes in HBLA layer is depicted in Fig. 5.1. The \mathbf{c} axis orients along the long axis of the nanocolumns. The monoclinic angle β denotes the angle between \mathbf{b} and \mathbf{c} . The Euler angle θ indicates the angle between the \mathbf{c} axis and the substrate surface normal (slanting angle of the nanocolumns). The optical constants along

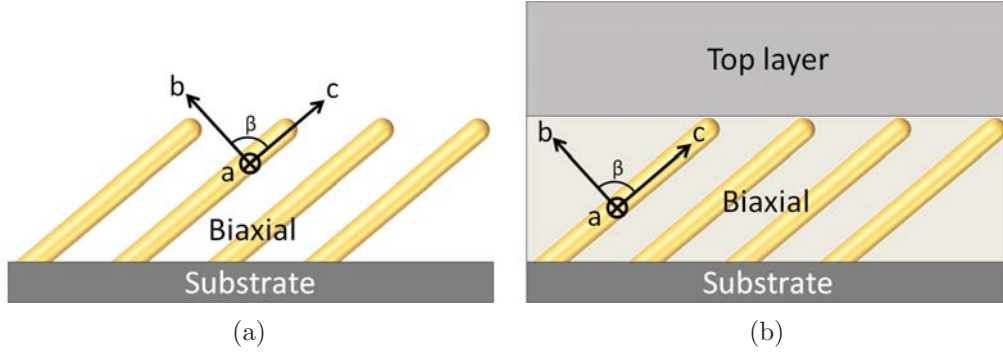


Figure 5.1: Optical models for (a) the as-deposited permalloy SCTF; (b) permalloy SCTF infiltrated with PMMA. **a**, **b** and **c** denote the major polarizability axes, β is the internal angle between **b** and **c**.

each major axis in the HBLA layer are parameterized using sums of harmonic oscillator functions to maintain Kramers-Kronig consistency and reduce the numbers of unknown parameters. The experimental data and model-calculated data are matched as close as possible by varying the model parameters (best-model).

Two AB-EMA formalisms (TAB-EMA and RAB-EMA) are further employed to obtain useful structural parameters such as constituent fractions. Based on the target data for analysis, two different analysis procedures are used. In the first procedure, the two AB-EMA formalisms are used to match the effective optical constants from the HBLA analysis to obtain the constituent fractions. Since the target data are the effective optical constants along each major axis, structural parameters, such as the slanting angle, SCTF thickness, internal angle between **b** and **c**, are excluded during the analysis. Only f_i (the volume fraction of each component), L_j or D_j (depolarization factor along each axis) and ε_i (the bulk dielectric function of each component) in Eq. 3.28 and 3.32 are varied to match the target data as close as possible. Note that the uncertainties in the HBLA results also affect the AB-EMA analysis⁽¹³⁵⁾. In this procedure, the MSE used to evaluate the quality of the regression analysis becomes a function of the effective dielectric functions obtained from the HBLA as defined in Eq. 3.37. For the SCTFs, the AB-EMA formalisms comprise the bulk optical constants of permalloy

and void ($n = 1, k = 0$). For the SCTFs with PMMA, the AB-EMA formalisms comprise the bulk optical constants of permalloy, PMMA and void. The optical constants of permalloy are first determined on a wavelength-by-wavelength basis in the modeling for as-deposited SCTFs, and kept constant in subsequent analysis for the hybridized SCTFs.

In the second procedure, the target data are the experimental Mueller matrix element data and the two AB-EMA formalisms are used to match the experimental data. Besides the constituent volume fractions, depolarization factors and bulk optical constants, structural parameters including the slanting angle, SCTF thickness, internal angle between \mathbf{b} and \mathbf{c} are also varied to reach the best match. MSE used in this procedure is a function of Mueller matrix elements as defined in Eq. 3.36. A stratified optical model as depicted in Fig. 5.1 is utilized to analyze the experimental data. For the SCTFs, the optical model comprises a Si substrate and an AB-EMA layer. The AB-EMA layer accounts for the SCTF and includes the bulk optical constants of permalloy and void. For the SCTFs with PMMA, the model consists of a Si substrate, an AB-EMA layer and a top PMMA layer. The AB-EMA layer accounts for the SCTF with PMMA and comprises the optical constants of permalloy, PMMA and void. The bulk optical constants of permalloy are parameterized using sums of harmonic oscillator functions in the modeling for the as-deposited SCTFs, and kept constant in subsequent analysis for the hybridized SCTFs.

5.2 SEM Analysis

The cross-section SEM images of typical samples for permalloy SCTFs and SCTFs infiltrated with PMMA are shown in Fig. 5.2(a) and (b), respectively. In Fig. 5.2(b), a 50 nm Ti layer was deposited on the SCTF infiltrated with PMMA. From SEM analysis for the SCTF, the SCTF thickness and slanting angle of the nanocolumns are evaluated to be $84 \text{ nm} \pm 10 \text{ nm}$ and $64^\circ \pm 1^\circ$, respectively. For the SCTF with PMMA, the SEM analysis show that the thickness and slanting angle become $68 \text{ nm} \pm 3 \text{ nm}$ and $69^\circ \pm 1^\circ$, respectively. The thickness of the top PMMA layer is estimated to be $86 \text{ nm} \pm 4 \text{ nm}$.

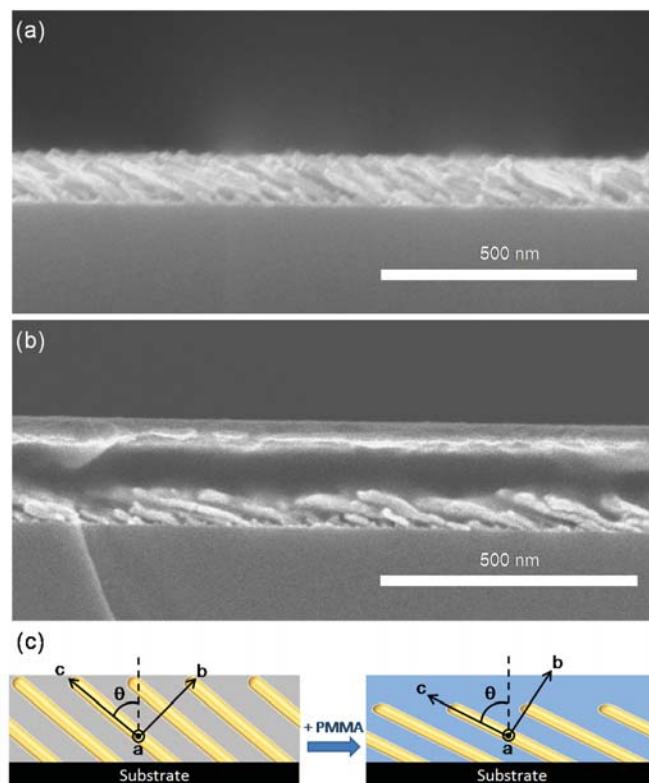


Figure 5.2: The cross-section SEM images of (a) the permalloy SCTF and (b) permalloy SCTF infiltrated with PMMA. As shown in (b), a 50 nm Ti layer was deposited on the top. The scheme in (c) depicts the orientation of the major polarizability axes. The solid arrows denote the geometry of the biaxial system with the \mathbf{c} axis along the orientation of the slanted nanocolumns and \mathbf{a} parallel to the film surface. θ represents the angle between the axis \mathbf{c} and the substrate surface normal (slanting angle of the nanocolumns). The dashed line denotes the substrate surface normal. The gray and blue areas indicate void and PMMA in the interspace between the nanocolumns, respectively.

5.3 Homogeneous Biaxial Layer Approach Analysis

5.3.1 Experimental and Best-model Calculated Mueller Matrix Data (1st Procedure)

Fig. 5.3 depicts the experimental Mueller matrix elements M_{ij} normalized to M_{11} for the permalloy SCTF and SCTF infiltrated with PMMA. The Mueller matrix elements which are not shown in the figure can be obtained by symmetry⁽¹⁴¹⁾. The diagonal elements (M_{12} , M_{22} , M_{33} and M_{34}) of both samples show a mirror symmetry with the symmetry plane located at around $\phi = 180^\circ$. For the ease of comparison, the off-diagonal elements (M_{13} , M_{14} , M_{23} and M_{24}) for both samples are shown next to each other in Fig. 5.4. The experimental off-diagonal elements for both samples show a two-fold rotational symmetry versus sample azimuth ϕ with the rotation axis located at around the center of each block ($M_{ij} = 0$ and $\phi = 180^\circ$). The off-diagonal elements reveal a strong optical anisotropy since these elements are zero for isotropic samples regardless of sample azimuth, angle of incidence and wavelength⁽⁹⁵⁾. The off-diagonal elements approach to zero for all angles of incidence at $\phi \approx 0^\circ$ and 180° where the nanocolumn orientation is parallel to the plane of incidence. These positions are termed the pseudo-isotropic sample orientations⁽⁹⁵⁾. After infiltration, the two pseudo-isotropic sample orientations with $M_{ij} \approx 0$ remain at $\phi \approx 0^\circ$ and $\phi \approx 180^\circ$. It is noted that the variation of the off-diagonal Mueller matrix elements at $\lambda = 600$ nm versus ϕ has changed after polymer infiltration, which indicates a change in the anisotropic optical properties of the hybridized SCTF.

The experimental Mueller matrix elements for the two samples are also shown within a spectral range from 400 to 1650 nm in Fig. 5.5. A large discrepancy can be found between the spectral Mueller matrix data of the two samples especially in the visible range from 400 to 700 nm. For the SCTF with PMMA, evident peaks in the diagonal element spectra are identified between 500 and 750 nm for different sample azimuths. In the off-diagonal spectra, similar features are still observable in this range. But at $\phi \approx 0^\circ$ where pseudo-isotropic sample orientation

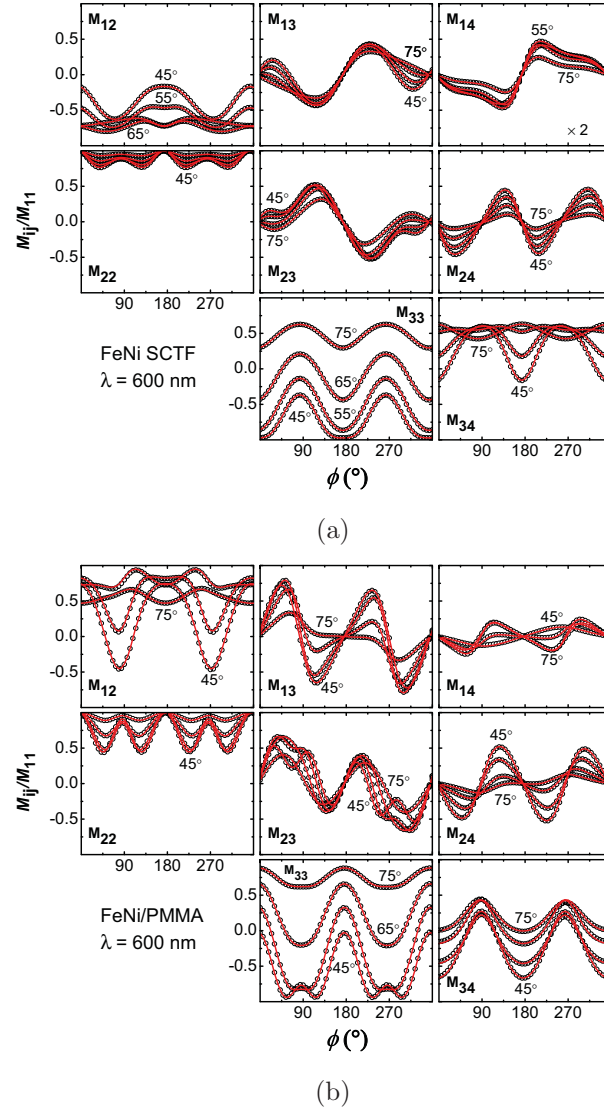


Figure 5.3: Experimental (open circles) and best-model calculated (solid lines) Mueller matrix elements M_{ij} normalized to M_{11} versus sample azimuth ϕ and angle of incidence $\Phi_a = 45^\circ, 55^\circ, 65^\circ, 75^\circ$ at $\lambda = 600$ nm: (a) the permalloy SCTF; (b) SCTF infiltrated with PMMA. The GE data are presented by Mueller matrix elements M_{ij} normalized to M_{11} . Note that M_{14} for the permalloy SCTF is multiplied by 2.

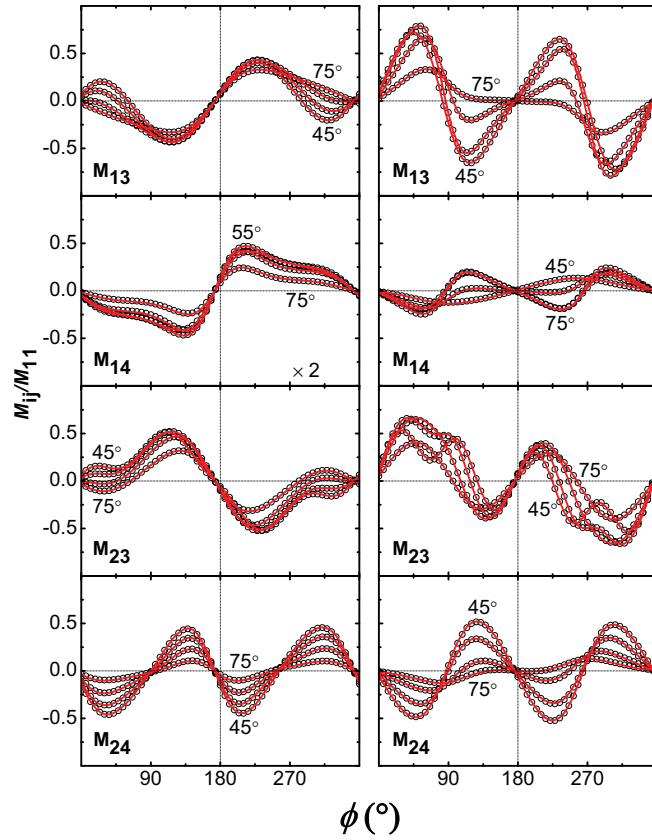
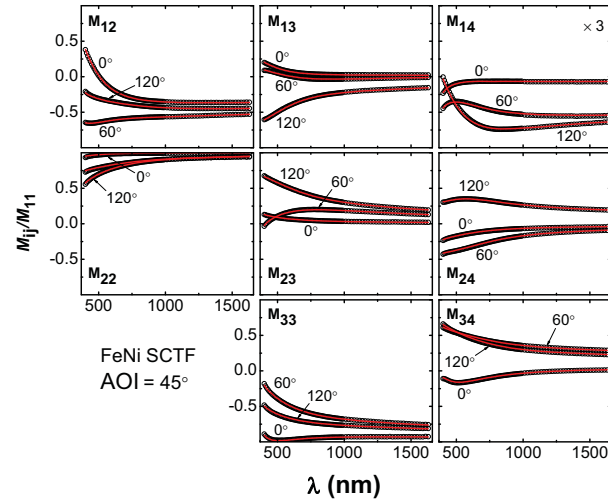
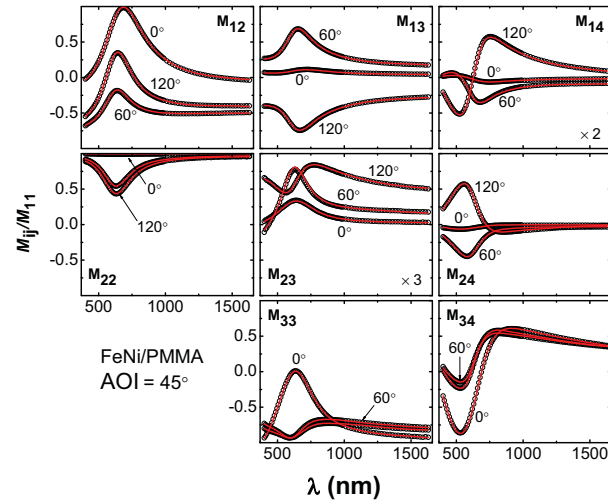


Figure 5.4: Experimental (open circles) and best-model calculated (solid lines) off-diagonal Mueller matrix elements M_{ij} normalized to M_{11} versus sample azimuth ϕ and angle of incidence $\Phi_a = 45^\circ, 55^\circ, 65^\circ, 75^\circ$ at $\lambda = 600$ nm. The left column shows the GE data for the permalloy SCTF and the right one shows the data for the SCTF infiltrated with PMMA. Note that M_{14} for the permalloy SCTF is multiplied by 2.



(a)



(b)

Figure 5.5: Experimental (open circles) and best-model calculated (solid lines) Mueller matrix elements M_{ij} normalized to M_{11} at angle of incidence $\Phi_a = 45^\circ$ for three different sample azimuths $\phi = 0^\circ, 60^\circ, 120^\circ$ within spectral range from 400 to 1650 nm: (a) the permalloy SCTF; (b) SCTF infiltrated with PMMA. Note that M_{14} in (a) and M_{14}, M_{23} in (b) are scaled up. Note that M_{14} for the permalloy SCTF is multiplied by 2.

occurs, the peak features are substantially reduced and the entire spectra vanish to almost zero. The HBLA is utilized to analyze the experimental data. As shown in Fig. 5.3 and 5.5, the experimental and best-model calculated data are in excellent agreement.

5.3.2 Structural properties

The structural parameters of the samples determined by the best-model analysis of the HBLA are shown in Table 5.1. The best-model results represent the averaged physical properties over the measured spot on the samples. The error bars in the table denote the finite uncertainty which is related to the measurement accuracy and best-model calculation process. The best-model results for the permalloy SCTF reveal a film thickness of 83 nm and slanting angle of 64° approximately, which are highly consistent with the values found from SEM investigation ($84 \text{ nm} \pm 10 \text{ nm}$ and $64^\circ \pm 1^\circ$, respectively). From Table 5.1, it can be seen that after infiltration the SCTF thickness t_s is reduced to be approximately 66 nm and slanting angle θ increases to 70° , and both values show good agreement with the results from SEM image analysis showing $t_s \approx 68 \text{ nm}$ and $\theta \approx 69^\circ$. The top layer thickness is determined to be 87 nm which also shows high consistency with the SEM result ($86 \pm 4 \text{ nm}$).

Table 5.1: The best-model parameters for the permalloy SCTF and SCTF infiltrated with PMMA. t_s : SCTF thickness; t_p : thickness of top PMMA layer; β : the angle between \mathbf{b} and \mathbf{c} ; θ : the slanting angle. The error bars given in parentheses denote the numerical uncertainty of the last digit (90% confidence interval).

Parameter	SCTF	SCTF+PMMA
t_s (nm)	82.53(4)	66.09(8)
θ ($^\circ$)	64.44(1)	70.25(2)
t_p (nm)	N/A	86.58(5)
β ($^\circ$)	91.68(2)	90.82(3)
MSE	5.71	5.32

5.3.3 Anisotropic Optical Properties

Fig. 5.6 shows the effective optical constants along the three major axes of the permalloy SCTF and SCTF with PMMA obtained from the best-model calculation based on the HBLA. The dispersion of the refractive indices shows similar pattern for both samples. In addition, the optical constants for both samples exhibit the strongest wavelength dependency along **c** axis. Nevertheless, the optical constants along each axis are enhanced substantially across the investigated spectral range after polymer infiltration. The optical constants along the **c** axis show relatively

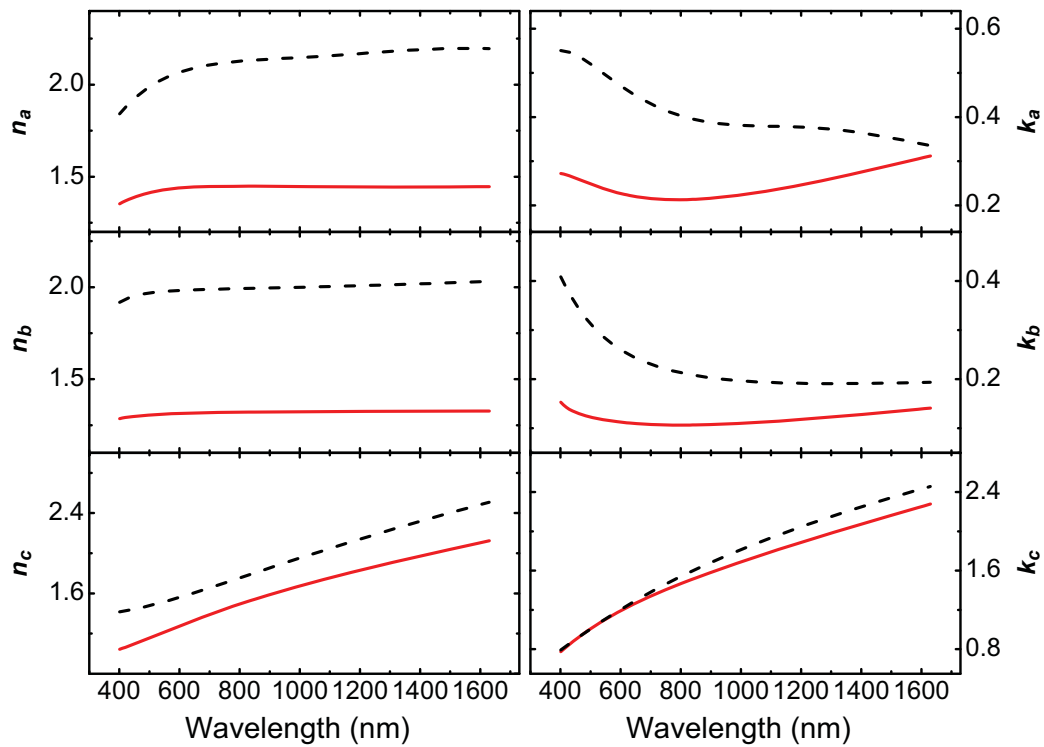


Figure 5.6: Effective optical constants along the major axes **a**, **b** and **c** for the permalloy SCTF (red solid line) and SCTF infiltrated with PMMA (black dash line): n_a , n_b , n_c and k_a , k_b , k_c . The effective optical constants are obtained from the best-model calculations based on HBLA.

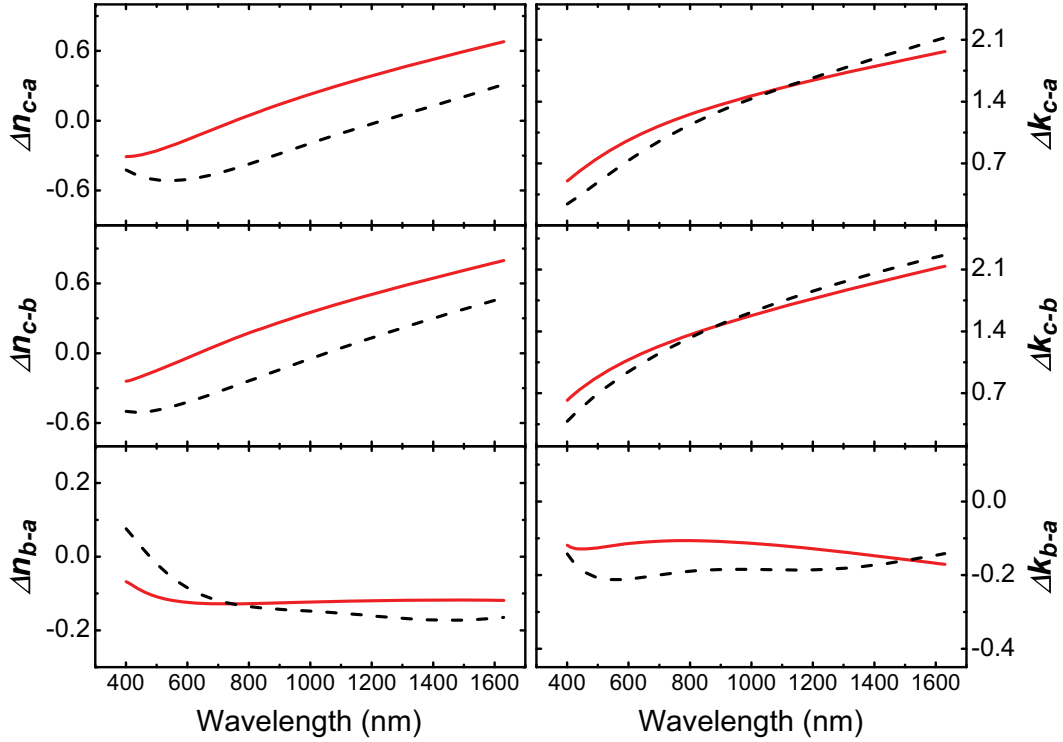


Figure 5.7: The birefringence and dichroism between the major axes obtained from the HBLA for the permalloy SCTF (red solid line) and SCTF infiltrated with PMMA (black dashed line): $\Delta n_{c-a} = n_c - n_a$, $\Delta k_{c-a} = k_c - k_a$; $\Delta n_{c-b} = n_c - n_b$, $\Delta k_{c-b} = k_c - k_b$; $\Delta n_{b-a} = n_b - n_a$, $\Delta k_{b-a} = k_b - k_a$.

smaller variation, whereas the optical constants of the SCTF with PMMA along **a** and **b** axes display a large difference upon polymer infiltration. Because PMMA adds a larger isotropic optical constant to the hybrid than air, the effective optical constants along **a** and **b** increase after polymer infiltration. Furthermore, the increased slanting angle leads to a smaller intercolumnar distance along **b**, thereby increasing the volume fraction of permalloy and optical constants in this direction.

Fig. 5.7 depicts the birefringence and dichroism between the major axes for the as-deposited and hybridized SCTFs. The effective optical constants along each

major axis are extracted from the HBLA analysis, subsequently the birefringence and dichroism are represented by the difference of the effective optical constants between the axes. The birefringence and dichroism for both samples show a strong wavelength-dispersion. Figure 5.7 reveals that the dispersion of the birefringence and dichroism presents a large difference after infiltration. For example, Δk_{b-a} becomes more negative in the spectral range from approximately 400 to 1500 nm, indicative of a larger dichroism between axis **a** and **b** for the hybrid. The changes in dichroism can be mainly explained by the nanocolumn deformation due to infiltration, since PMMA as a transparent infiltration material can mostly influence the birefringence. The augmentation in Δk_{b-a} for the hybrid could be caused by the reduction of intercolumnar distance along **b**, because k_b increases when the permalloy columns are closer to each other along this direction.

5.3.4 Discussion

It is noted that t_s decreases by approximately 17 nm and θ increases by 6° upon PMMA infiltration. The two parameters are directly correlated to each other, since an increase in slanting angle is caused by bending the nanocolumns towards the substrate surface which causes a reduction of film thickness (shown in Fig. 5.2(c)). The following equation can be used to calculate the change of the SCTF thickness as a function of the slanting angle:

$$t'_s = t_s \left(\frac{\cos \theta'}{\cos \theta} \right), \quad (5.1)$$

where the apostrophe denotes the structural parameters after infiltration. Inserting the best-model parameters $\theta=64.44^\circ$, $\theta'=70.25^\circ$ and $t_s = 82.53$ nm into Eq. 5.1, we can estimate a film thickness $t'_s \approx 64.6$ nm for the SCTF with PMMA. From model results we obtain a reduction of the film thickness to 66 nm, which is very close to the calculated value of 64.6 nm. In Fig. 5.4, the pseudoisotropic orientations for the hybrid remain at $\phi \approx 0^\circ$ and $\phi \approx 180^\circ$, indicating the further inclination of the nanocolumns still occurs within the same plane.

Krause *et al.* also reported a further inclination of 10° for TiO₂ nanorods after spin-coating with photoresist and subsequent baking⁽⁸⁴⁾. The bending of the

nanocolumns might occur during the polymer solidification process. In general, the solidification of polymer films is caused by macromolecular chain cross-linking and associated with material shrinkage. For a planar PMMA film, the shrinkage is restrained in the direction of the interface by the polymer adhesion to the substrate while the shrinkage in direction parallel to the film normal can develop freely⁽¹⁴²⁾. Spectroscopic ellipsometry was performed to investigate the thickness change of a pure PMMA film spin-coated onto a Si substrate after baking at 165 °C for 1 h. The ellipsometry analysis shows that the PMMA film thickness decreases from 121.4 to 109.8 nm after baking, indicative of a volume shrinkage. The shrinkage introduces stress into the SCTF which causes the nanocolumns to bend towards the substrate surface thereby reducing the intercolumnar distance. The SCTF thickness decrease shown in Table 5.1 reveals a reduction on the interspace volume, which is consistent with the volume shrinkage of PMMA upon baking. Therefore, the nanocolumn bending might be caused by polymer volume shrinkage due to temperature induced cross-linking.

5.4 Anisotropic Bruggeman Effective Medium Approximation Analysis

5.4.1 Use of Effective Optical Constants from the HBLA as Target Data

The two formalisms of AB-EMA are used to model the effective optical constants along the three axes as obtained by the HBLA. Fig. 5.8 shows the effective optical constants. For the permalloy SCTF, k_a and k_b obtained from the RAB-EMA exhibit a better match with the HBLA. Along the axis \mathbf{c} , both AB-EMA models show an excellent match with the HBLA. For the hybridized SCTF, the optical constants along \mathbf{c} from the TAB-EMA show a closer match with the HBLA. Otherwise, the matches of the two models with the HBLA indicate a wavelength dependence. For instance, k_b of the hybridized SCTF produced by the RAB-EMA shows a better match with the the HBLA below around 800 nm, but above 800 nm the TAB-EMA shows a closer match. The MSE listed in Table 5.2 reflects

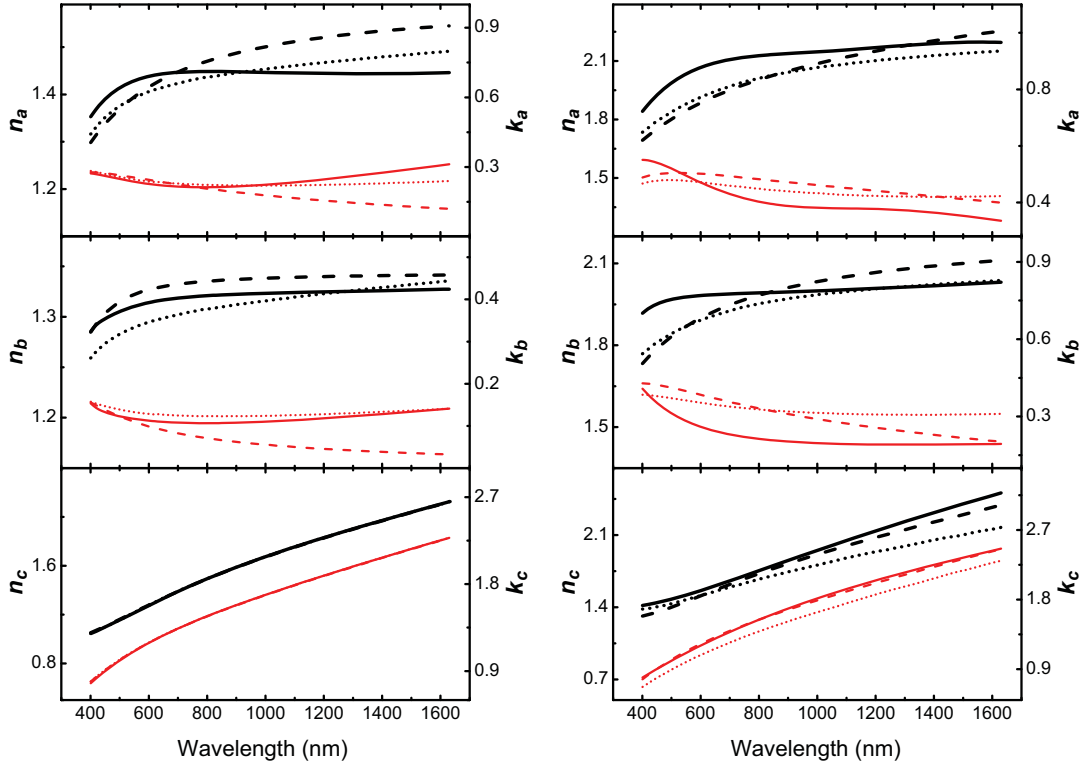


Figure 5.8: Effective optical constants, n_j (thick black line) and k_j (thin red line) along the major axes **a**, **b** and **c** determined by the HBLA (solid lines), TAB-EMA (dashed lines) and RAB-EMA (dotted lines) in the 1st procedure. The left column shows the results for the permalloy SCTF and the right one for the SCTF infiltrated with PMMA.

the overall agreement between the two AB-EMA formalisms and HBLA. For the SCTF, the MSE for the RAB-EMA is lower than that for the TAB-EMA, revealing a better match given by the RAB-EMA. For the SCTF with PMMA, the TAB-EMA delivers a closer match to the HBLA as indicated by the lower MSE.

The parameters of the AB-EMA described in Eq. 3.28 and Eq. 3.32 can be extracted from the best-model (shown in Table 5.2). Note that for convenient comparison the D_j values determined by the RAB-EMA are converted according to the definition of L_j of the TAB-EMA as shown in Eq. 3.29. The volume fraction of void f_v obtained by the TAB-EMA decreases substantially from approximately

75% to 9% indicative of an excellent polymer filling into the void regions, while $f_v = 0$ obtained by the RAB-EMA shows no more sensitivity to f_v after the infiltration. For the depolarization factors, the TAB-EMA shows that L_c becomes zero for both samples, but the RAB-EMA provides a result with small value of L_c , which is consistent with the nanocolumn shape elongated along \mathbf{c} .

Fig. 5.9 shows the bulk-like optical constants of permalloy for the SCTFs determined by the TAB-EMA and RAB-EMA in the 1st procedure. A large discrepancy can be seen in the results obtained from the two formalisms. Particularly the refractive indices obtained by TAB-EMA display a much higher value than those obtained by RAB-EMA. Additionally, the refractive indices from the two formalisms show great difference in wavelength dispersion. The extinction coefficients from TAB-EMA show similar dispersion with those from RAB-EMA, but TAB-EMA yields lower values than RAB-EMA. A 100 nm solid permalloy thin film was deposited on Si substrate with our GLAD system as a reference

Table 5.2: The best-model parameters for the as-deposited SCTF and the SCTF infiltrated with PMMA obtained from TAB-EMA and RAB-EMA in the 1st procedure. f_v : the volume fraction of void; f_{py} : the volume fraction of permalloy nanocolumns; f_p : the volume fraction of PMMA; L_j : depolarization factor along each major axis. The error bars given in parentheses denote the numerical uncertainty of the last digit (90% confidence interval).

	TAB-EMA		RAB-EMA	
	SCTF	SCTF/PMMA	SCTF	SCTF/PMMA
f_v (%)	74.66(9)	9.0(7)	79.56(2)	0
f_{py} (%)	25.34(9)	30.8(2)	20.44(2)	20.4(1)
f_p (%)	NA	60.2(5)	NA	79.6(1)
L_a	0.428(2)	0.457(2)	0.383(2)	0.39(2)
L_b	0.572(2)	0.543(2)	0.527(1)	0.47(1)
L_c	0	0	0.090(3)	0.14(2)
MSE	0.161	0.329	0.057	0.636

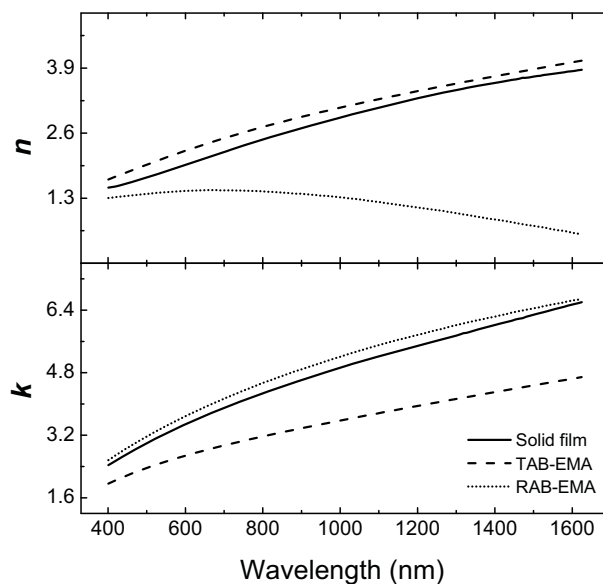


Figure 5.9: Bulk optical constants of permalloy determined by TAB-EMA (dashed lines) and RAB-EMA (dotted lines) in the 1st procedure, which are compared with the optical constants of a 100 nm solid permalloy film obtained from a wavelength-by-wavelength analysis (solid lines).

sample and the optical constants of the film were determined with wavelength-by-wavelength analysis for comparison. The refractive indices from TAB-EMA exhibit good agreement with the data of the solid film, but the RAB-EMA delivers extinction coefficients which show a closer match to the reference sample.

5.4.2 Use of Mueller Matrix Elements as Target Data (2nd Procedure)

In the second procedure, TAB-EMA and RAB-EMA are employed to analyze the experimental Mueller matrix elements directly, therefore structural properties such as SCTF thickness and slanting angle can also be obtained with the two formalisms. Fig. 5.10 depicts the match between the experimental Mueller matrix element data and the best-model calculated data from the two formalisms. It can

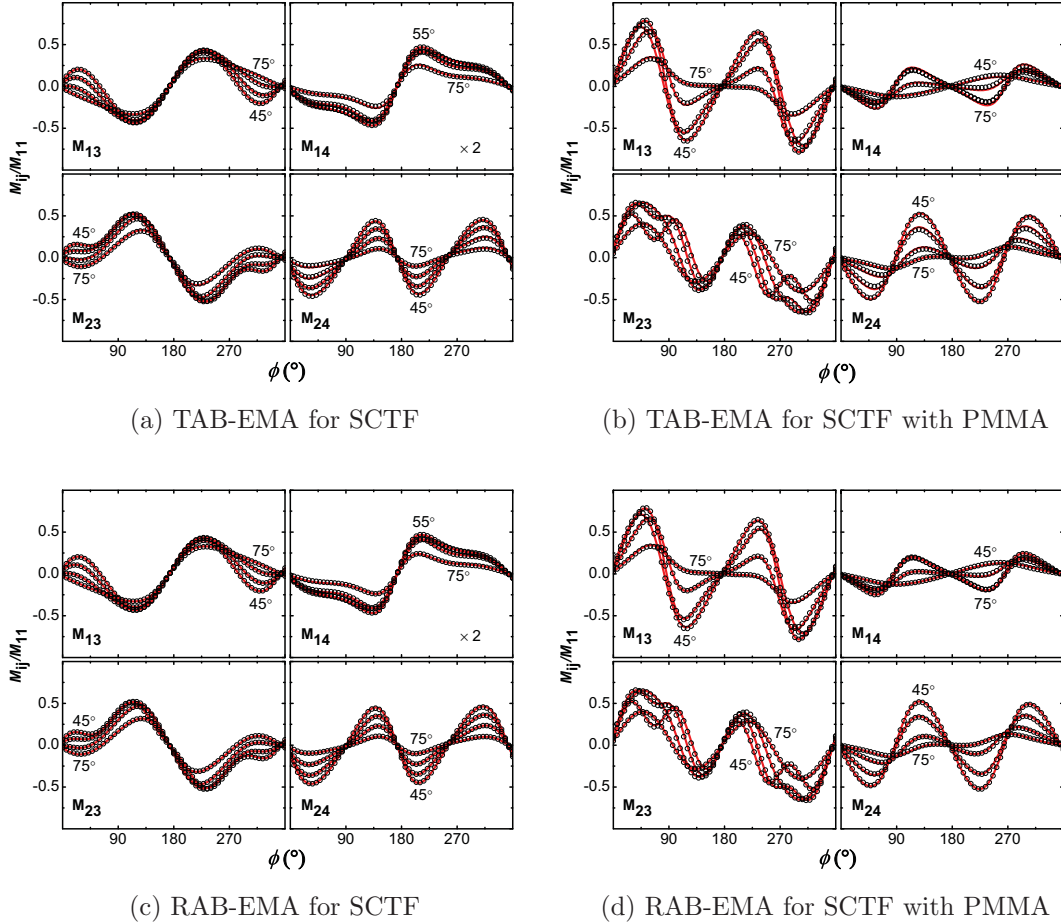


Figure 5.10: Experimental (open circles) and best-model calculated (solid lines) off-diagonal Mueller matrix elements M_{ij} normalized to M_{11} versus sample azimuth ϕ and angle of incidence $\Phi_a = 45^\circ, 55^\circ, 65^\circ, 75^\circ$ at $\lambda = 600$ nm. The best-model calculated data in (a) and (b) are obtained from TAB-EMA while the data in (c) and (d) are from RAB-EMA. (a) and (c) show the data for the as-deposited permalloy SCTF; (b) and (d) show the data for the SCTF infiltrated with PMMA. Note that M_{14} for the permalloy SCTF is multiplied by 2.

be seen that both formalisms yield a good match with the experimental data.

The structural parameters of the samples determined by the best-model analysis of the TAB-EMA, RAB-EMA and HBLA are shown in Table 5.3. As described in Sect. 3.3.4.1, the HBLA is a simple and primary method with few model assumption, the results from the HBLA which highly conform with the SEM analysis are also shown here. The MSE values indicate that the HBLA yields the closest match to the experimental data. For both permalloy SCTF and SCTF with PMMA, the RAB-EMA with lower MSE gives closer match to the experimental

Table 5.3: The best-model parameters for the as-deposited SCTF and the SCTF infiltrated with PMMA obtained from TAB-EMA (TAB) and RAB-EMA (RAB) in the 2nd procedure. t_s : SCTF thickness; t_p : thickness of top PMMA layer; β : the angle between \mathbf{b} and \mathbf{c} ; θ : the slanting angle; f_v : the volume fraction of void; f_{py} : the volume fraction of permalloy nanocolumns; f_p : the volume fraction of PMMA; L_j : depolarization factor along each major axis. The error bars given in parentheses denote the numerical uncertainty of the last digit (90% confidence interval). Note that the D_j values determined by the RAB-EMA are converted according to the definition of L_j of the TAB-EMA as shown in Eq. 3.29.

	SCTF			SCTF/PMMA		
	HBLA	TAB	RAB	HBLA	TAB	RAB
t_s (nm)	82.53(4)	74.35(9)	86.23(4)	66.09(8)	67.17(6)	75.43(2)
θ ($^\circ$)	64.44(1)	61.97(2)	64.93(1)	70.25(2)	67.91(4)	71.47(2)
t_p (nm)	N/A	N/A	N/A	86.58(5)	89.74(3)	81.22(1)
β ($^\circ$)	91.68(2)	83.12(6)	92.22(3)	90.82(3)	91.39(5)	92.64(3)
f_v (%)	N/A	75.58(3)	78.49(1)	N/A	0.8(1)	3.07(5)
f_{py} (%)	N/A	24.42(3)	21.51(1)	N/A	27.49(4)	23.56(1)
f_p (%)	N/A	N/A	N/A	N/A	71.7(2)	73.37(3)
L_a	N/A	0.418(1)	0.392(7)	N/A	0.4171(4)	0.386(2)
L_b	N/A	0.513(1)	0.550(7)	N/A	0.5005(4)	0.548(2)
L_c	N/A	0.069(1)	0.058(7)	N/A	0.0825(3)	0.066(2)
MSE	5.71	12.87	8.352	5.32	16.19	11.98

data than TAB-EMA. Herein, the structural properties obtained from the two AB-EMA formalisms are compared with the HBLA results for both samples.

For the permalloy SCTF, the RAB-EMA renders closer results to HBLA in SCTF thickness, slanting angle and internal angle β . For instance, the internal angles from the HBLA and RAB-EMA approach to 90° indicating orthorhombic optical properties, while the TAB-EMA reveals a monoclinic optical response for the SCTF. For constituent volume fractions, both formalisms deliver close results, except that the TAB-EMA gives a slightly higher value in permalloy fraction than RAB-EMA. The two formalisms also render similar results of depolarization factors with very small values along axis \mathbf{c} which are consistent with the columnar structure elongated along \mathbf{c} . The EMA parameters (constituent fractions and depolarization factors) from the two formalisms in this procedure show good agreement with the model results in the 1st procedure (Table 5.2). The noticeable difference is the nonzero value in L_c given by this procedure.

For SCTF infiltrated with PMMA, the TAB-EMA renders closer results to HBLA in SCTF thickness, while the RAB-EMA overestimates the thickness. The RAB-EMA again gives a more consistent slanting angle with the HBLA, while TAB-EMA underestimates this angle. All three modeling approaches deliver consistent results with β close to 90° which unravel orthorhombic optical properties within the SCTF after infiltration. The constituent fractions given by both AB-EMA formalisms reveal a large decrease in void fraction and increase in PMMA fraction, indicative of an excellent polymer infiltration into the porous areas of SCTF. Both formalisms deliver similar results of depolarization factors with smallest values along axis \mathbf{c} , suggesting the elongated columnar structure of SCTF is not changed after infiltration. The EMA parameters for SCTF with PMMA obtained by this procedure show a noticeable difference from those by the 1st procedure. For instance, the TAB-EMA yields a much lower void fraction than that in the 1st procedure and the TAB-EMA gives a lower L_c in this procedure.

Comparing the model results for the as-deposited and hybridized SCTFs, we find that both formalisms deliver a decreased SCTF thickness and an increased slanting angle which also reveal a further inclination of the nanocolumns after infiltration as identified in the previous HBLA modeling. In addition, the permalloy

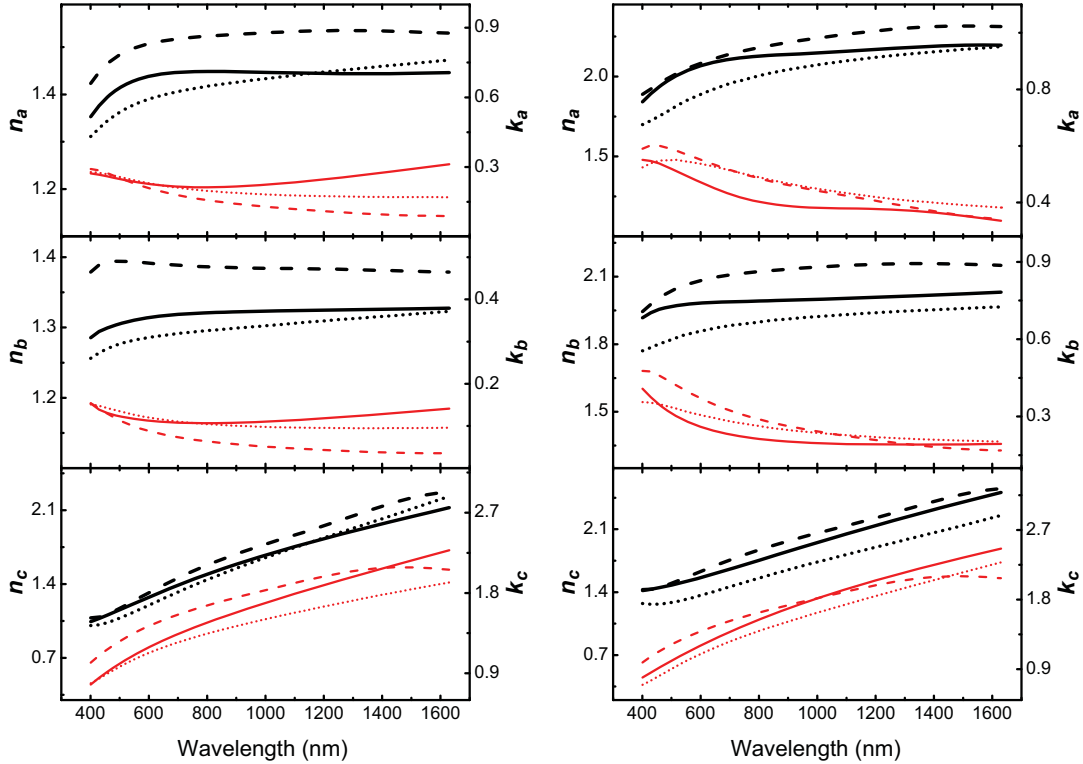


Figure 5.11: Effective optical constants, n_j (thick black line) and k_j (thin red line) along the major axes **a**, **b** and **c** determined by the HBLA (solid lines), TAB-EMA (dashed lines) and RAB-EMA (dotted lines) in the 2nd procedure. The left column shows the results for the permalloy SCTF and the right one for the SCTF infiltrated with PMMA.

fractions given by both formalisms show increased values after infiltration which are consistent with the interspace reduction due to nanocolumnar inclination as discussed in Sect. 5.3.4.

Fig. 5.11 compares the effective optical constants determined by the two AB-EMA formalisms in this procedure with the data obtained from the HBLA. Compared with the match obtained from the 1st procedure (shown in Fig. 5.8), the results for the permalloy SCTF obtained by the AB-EMA formalisms show larger deviation from the data obtained by the HBLA, especially along **c**. The TAB-EMA overestimates the refractive indices along **a** and **b**, while both formalisms

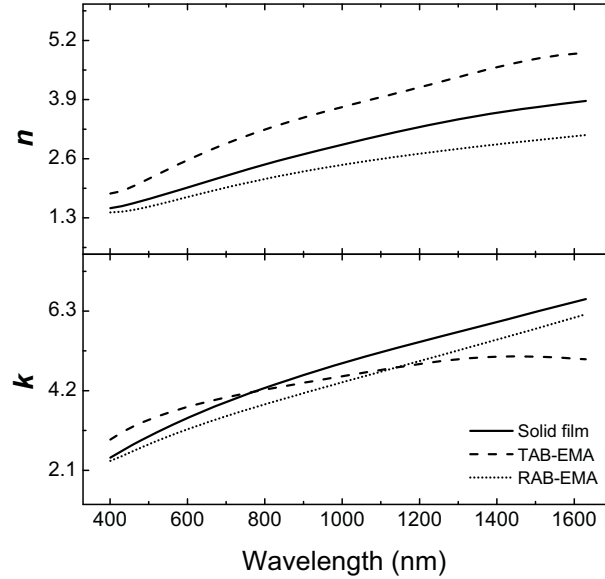


Figure 5.12: Bulk optical constants of permalloy determined by TAB-EMA (dashed lines) and RAB-EMA (dotted lines) in the 2nd procedure, which are compared with the optical constants of a 100 nm solid permalloy film obtained from a wavelength-by-wavelength analysis (solid lines).

underestimate the extinctive coefficients along **a** and **b**. The optical constants from the RAB-EMA exhibit a closer match to the data from the HBLA, especially along **a** and **b**. This better match in the biaxial optical constants could contribute to a lower MSE for the RAB-EMA as shown in Table 5.3 which indicates that the best-model calculated Mueller matrix data from the RAB-EMA exhibit a closer match to the experimental data than the TAB-EMA. For the SCTF with PMMA, no general trend can be found to compare the match of the two formalisms. For instance, the TAB-EMA yields a better match in n_c while the RAB-EMA delivers a closer match in k_b . The matches of the two formalisms with the HBLA mostly show a wavelength dependence.

Fig. 5.12 shows the bulk-like optical constants of permalloy for the SCTFs determined by the TAB-EMA and RAB-EMA in the 2nd procedure. Compared with the results in the 1st procedure (as shown in Fig. 5.9), the bulk optical

constants for the RAB-EMA in this procedure show much smaller difference from the data for the RAB-EMA. For instance, the bulk refractive indices given by the two formalisms follow similar wavelength dispersion. The extinction coefficients given by the two formalisms also show better agreement. But the refractive indices obtained by TAB-EMA still display higher value than those obtained by RAB-EMA over the entire spectrum. The refractive indices of the solid permalloy film are between the TAB-EMA and RAB-EMA data. The extinction coefficients given by the RAB-EMA show closer match to the reference sample at long wavelength.

5.4.3 Discussion

Compared with the HBLA, the TAB-EMA and RAB-EMA provide useful information on the constituent fractions of a porous film with material infiltration. Thus the analysis procedures are performed mainly to evaluate hybridization level as well as the fraction changes after polymer infiltration.

In the 1st procedure, the TAB-EMA shows that the volume fraction of the permalloy nanocolumns f_{py} increases from around 25% to 31% (shown in Table 5.2), which reveals that the volume fraction of the interspace f_{in} is reduced since ideally $f_{\text{in}} = 1 - f_{\text{py}}$. With larger slanting angle the nanocolumns approach each other and the intercolumnar distance along axis \mathbf{b} decreases (Fig. 5.2(c)), thus the increased permalloy fraction f_{py} is consistent with a larger slanting angle. If the physical volume of permalloy V_{py} remains constant upon infiltration the increase in volume fraction must be related to a decrease in interspace volume. The change of the interspace volume can be estimated by finding the ratio for the interspace volume fraction before and after infiltration and can be expressed by:

$$\frac{t'_s}{t_s} = \frac{V_{\text{py}}\left(\frac{1 - f'_{\text{py}}}{f'_{\text{py}}}\right)}{V_{\text{py}}\left(\frac{1 - f_{\text{py}}}{f_{\text{py}}}\right)}, \quad (5.2)$$

where the apostrophe denotes the structural parameters after infiltration. Substituting the model parameters of HBLA $t_s = 82.53$ nm, $t'_s = 66.09$ nm and TAB-EMA parameter $f_{\text{py}} = 25.34\%$ into Eq. 5.2, we obtain $f'_{\text{py}} \approx 29.8\%$ which

agrees with the TAB-EMA result of 30.8%. f_{py} obtained by the RAB-EMA shows a nearly constant value for the hybridized SCTF. Thereby, the permalloy volume fraction change revealed by the TAB-EMA is more consistent with the larger nanocolumnar slanting angle after infiltration.

In the 2nd procedure, structural properties such as film thickness can be obtained from the TAB-EMA and RAB-EMA. The results from both formalisms (shown in Table 5.3) reveal a decreased SCTF thickness and an increased slanting angle after infiltration which are consistent with the HBLA modeling results. Eq. 5.1 is used to calculate the change of SCTF thickness as a function of the slanting angle. Inserting the model parameters θ , θ' and t_s of TAB-EMA and RAB-EMA into Eq. 5.1, respectively, we estimate a SCTF thickness of hybridized SCTF $t'_s \approx 60$ nm for TAB-EMA and $t'_s \approx 65$ nm for RAB-EMA (shown in Table 5.4). Compared with the calculation, both formalisms deliver a larger film thickness.

In the 2nd procedure, the permalloy fractions given by the two AB-EMA formalisms show increased values after infiltration, therefore both formalisms deliver results which show consistency with the further nanocolumnar inclination. Inserting the model parameters from the TAB-EMA and RAB-EMA into Eq. 5.2, respectively, we obtain that $f'_{\text{py}} \approx 26.3\%$ for TAB-EMA and $f'_{\text{py}} \approx 23.9\%$ for RAB-EMA as shown in Table 5.4. The permalloy fraction given by the TAB-EMA is slightly above the calculation, while the fraction given by the RAB-EMA is highly

Table 5.4: Comparison between the best-model parameters in the 2nd procedure with the calculated values based on Eq. 5.1 and 5.2. t'_s and f'_{py} denote the SCTF thickness and volume fraction of permalloy nanocolumns for the SCTF infiltrated with PMMA, respectively.

	TAB-EMA		RAB-EMA	
	Calculation	Model	Calculation	Model
t'_s (nm)	60	67.2	65	75.4
f'_{py} (%)	26.3	27.5	23.9	23.6

consistent with the calculation. Additionally, both formalisms give a significantly reduced void fraction which indicates a high level of polymer infiltration.

As shown in Table 5.2 and 5.3, the constituent fraction results given by the two AB-EMA formalisms in either 1st or 2nd procedure show difference. For instance, the RAB-EMA delivers a higher void fraction for the permalloy SCTF than the TAB-EMA in either procedure, while TAB-EMA gives a higher permalloy fraction for the hybridized SCTF than the RAB-EMA. Unfortunately, alternative methods are lacked for accurate determination on the constituent fractions of SCTFs and hybridized SCTFs as discussed in Sect. 1.1.3.2. Therefore, no results can be obtained in the literatures for an comparison with the AB-EMA results to determine which formalism gives more accuracy.

The structural parameters such as film thickness and slanting angle can also be determined with the AB-EMA formalisms in the 2nd procedure, but it is noted that the AB-EMA results show some difference from the previous HBLA and SEM analysis. This disagreement could be attributed to the AB-EMA model assumption which deviates from the actual structure of SCTFs. Both AB-EMA formalisms are approximations based on an ideal scenario where highly oriented ellipsoidal inclusions are aligned in a host material. The model scenario is very different from a real SCTF sample in which the nanocolumns are not ideally ellipsoidal, but grown on the substrate. Additionally, the model parameters obtained from the AB-EMA represent the averaged physical properties of the nanocolumns which differ slightly from each other in shape and slanting angle. Therefore, the AB-EMA is a physical model which gives an averaged approximation towards the actual complicated SCTF structures. In contrast, the HBLA is a simple model which only assumes the SCTFs to be homogeneous and biaxial and negates any further assumption on the actual structure of the nanocolumns, thus it avoids large deviation from the real sample and provides reliable results showing the best agreement with the SEM analysis.

The effective optical constants along major axes are obtained from the AB-EMA formalisms in both procedures. However, good agreement with the HBLA results must be pursued, because the HBLA is considered to be a primary method

providing pristine results on the biaxial optical constants. In general, the AB-EMA results in the 1st procedure show a closer match to the HBLA data than in the 2nd procedure, since the 1st procedure uses directly the biaxial optical constants from the HBLA as the target data for AB-EMA modeling. The difference between the AB-EMA from HBLA data could be again due to the deviation of the AB-EMA model assumption from the actual SCTF structure. In both procedures, the two AB-EMA formalisms deliver the bulk optical constants of permalloy which show large differences from each other and from the optical constants of a solid permalloy film, especially the bulk refractive indices obtained in the 1st procedure. The difference between the bulk optical constants and the reference optical constants is generally expected, since porous nanocolumnar structure is significantly different from the solid thin film, this morphology difference could lead to surface and quantum confinement effects influencing the dielectric properties^(143–145). Again, the actual sample structure which is not considered in the AB-EMA model scenarios could contribute to this difference.

5.5 Conclusion

The HBLA and AB-EMA are incorporated into a GE analysis approach to determine the structural and optical changes of the porous SCTFs upon polymer infiltration. First, the HBLA is employed to model the GE data of SCTFs and hybridized SCTFs to obtain the effective biaxial optical constants and structural parameters. A further inclination of the nanocolumns after infiltration is identified by the HBLA modeling, which can be confirmed with scanning electron microscopy (SEM) analysis. The increase of optical constants along the major axes corresponds to the addition of PMMA and the structural changes. The changes in birefringence and dichroism are also fully revealed by the HBLA. It is deduced that the nanocolumn bending is caused by the polymer shrinkage during the solidification.

In order to evaluate the constituent fraction changes upon PMMA infiltration, the two AB-EMA formalisms are utilized to analyze the HBLA data of effective biaxial optical constants and experimental Mueller matrix data in two different pro-

cedures. In the 1st procedure, the AB-EMA results show a significantly reduced void fraction which indicates a high level of polymer infiltration. The changed permalloy fraction for the hybridized SCTF revealed by the modelling approaches show consistency with the nanocolumn deformation as identified in the previous HBLA and SEM results. The structural parameters such as SCTF thickness and slanting angle obtained in the 2nd procedure also show good agreement with SEM analysis.

Our analysis approach demonstrates that the HBLA is needed to deliver the pristine effective optical constants for SCTFs and hybridized SCTFs which can be used as the target data for the AB-EMA formalisms. Furthermore, the HBLA can be used to provide reliable results on the structural properties (SCTF thickness and slanting angle) which show the best agreement with SEM analysis. Both AB-EMA formalisms are based on model scenarios which differ partly from the real nanocolumnar structure within SCTFs, thus the two formalisms could yield results which deviate from each other, or from the HBLA and SEM analysis, for instance the bulk optical constants in both procedures. However, the AB-EMA formalisms are useful for determination of constituent fraction changes upon infiltration, which are difficult to obtain with other characterization methods.

Chapter 6

Optical Anisotropy of Porous Polymer Film Revealed via Generalized Ellipsometry

6.1 GE Data Analysis Procedure

Stratified optical models as illustrated in Fig. 6.1 are utilized to analyze the experimental Mueller matrix data with TAB-EMA. For the Co SCTF, the optical model comprises an isotropic Si substrate, an isotropic Ti layer and an anisotropic (AB-EMA) layer. The AB-EMA layer accounts for the biaxial dielectric response of SCTF and includes the bulk optical constants of Co and void ($n = 1$, $k = 0$). The orientation of the major polarizability axes in AB-EMA layer is depicted in Fig. 6.1(a). The \mathbf{c} axis orients along the long axis of the nanocolumns. The monoclinic angle β denotes the angle between \mathbf{b} and \mathbf{c} . The Euler angle θ indicates the angle between the \mathbf{c} axis and the substrate surface normal (slanting angle of the nanocolumns). The bulk optical constants of Co are parameterized using sums of harmonic oscillator functions to maintain Kramers-Kronig consistency and reduce the numbers of unknown parameters. For the Co SCTF infiltrated with PMMA before and after RIE, the model consists of a Si substrate, a Ti layer, an AB-EMA layer and a top isotropic PMMA layer. The AB-EMA layer accounting for the SCTF infiltrated with PMMA comprises the bulk optical constants of Co, PMMA

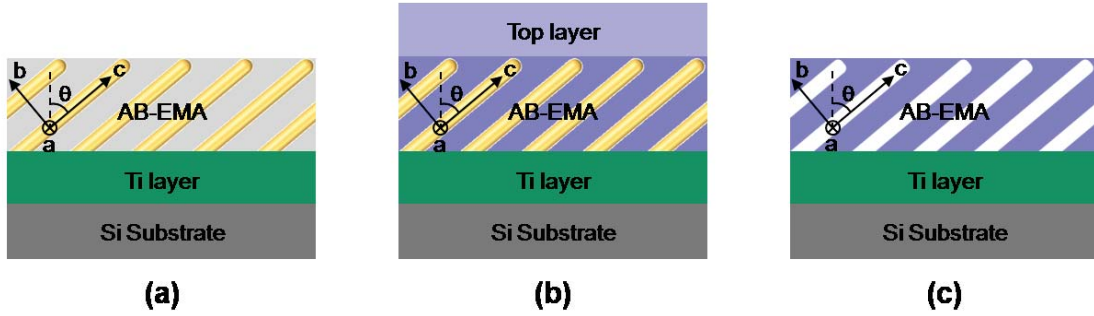


Figure 6.1: Optical models for: (a) the as-deposited Co SCTF; (b) Co SCTF infiltrated with PMMA before and after RIE; (c) PMMA iSCTF.

and void. The orientation of major axes for the sample (shown in Fig. 6.1(b)) is similar with the Co SCTF. For the PMMA iSCTF, the model consists of a Si substrate, a Ti layer and an AB-EMA layer. The AB-EMA layer accounting for the iSCTF includes the bulk optical constants of Co, PMMA and void. As depicted in Fig. 6.1(c), the c axis is directed along the long axis of the slanted columnar nanopores and θ denotes the slanting angle of the nanopores. The biaxial optical response of PMMA iSCTF is considered to be orthorhombic with $\beta = 90^\circ$. The bulk optical constants of Co determined previously in the modeling for Co SCTF and those of PMMA determined by a Cauchy model are kept constant during the modeling for the Co SCTF infiltrated with PMMA before or after RIE and PMMA iSCTF. In the modeling for all samples, the experimental and model-calculated data are matched as close as possible by varying the model parameters (best-model).

Same model and axis orientation shown in Fig. 6.1(c) are used for the RAB-EMA analysis on the PMMA iSCTF. The AB-EMA layer accounting for the iSCTF includes the bulk optical constants of Co, PMMA and void. The bulk optical constants for Co (from Palik⁽¹⁴⁶⁾) and PMMA (determined previously by a Cauchy model) are kept constant during the modeling.

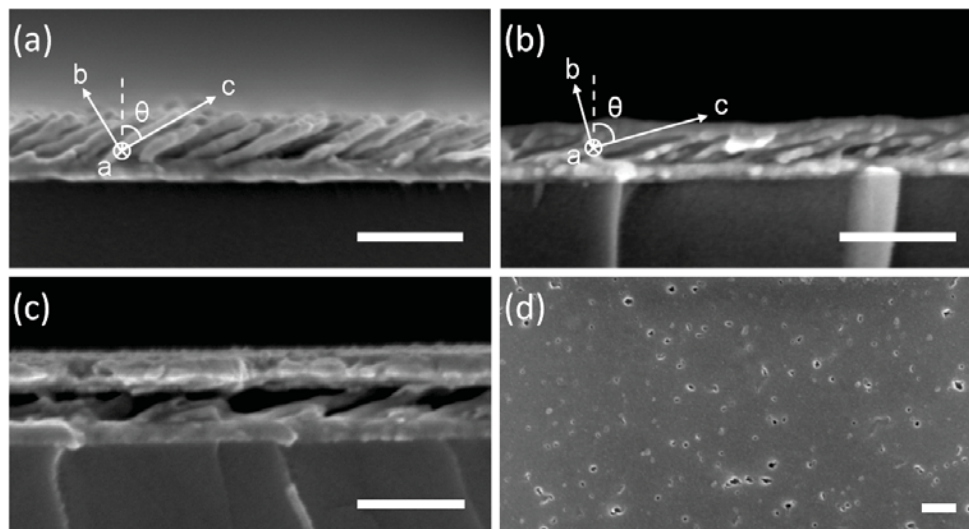


Figure 6.2: The cross-section SEM images of (a) the as-deposited Co SCTF, (b) PMMA iSCTF coated with 5 nm of Al_2O_3 , (c) PMMA iSCTF coated with 45 nm Ti layer and top-view SEM image of (d) PMMA iSCTF coated with 8 nm Ti. Scale bar: 200 nm. The overlaid schemes in (a) and (b) depict the orthorhombic system with the **c** axis along the orientation of the slanted nanocolumns or nanopores and **a** axis parallel to the film surface. The slanting angle θ represents the angle between **c** and the substrate surface normal (dashed line).

6.2 SEM and EDX Analysis

Fig. 6.2 shows the cross-section and top-view SEM images for typical samples of as-deposited Co SCTFs and PMMA iSCTFs. From the cross-sectional image of PMMA iSCTF in Fig. 6.2(b), it can be seen that the pores with shape of slanted columns are oriented within the PMMA matrix. The diameter of the slanted pores is evaluated to be $12 \text{ nm} \pm 4 \text{ nm}$ which is close to that of the as-deposited Co nanocolumns ($19 \text{ nm} \pm 4 \text{ nm}$) when a 5 nm Al_2O_3 coating is considered. Note that the nanoscale feature below 20 nm of the PMMA iSCTF is preserved by a conformal ALD coating of Al_2O_3 . The slanting angle of the nanopores is evaluated to be $71^\circ \pm 3^\circ$ in Fig. 6.2(b). From Fig. 6.2(c), the total thickness for Al_2O_3 -coated iSCTF plus the top Ti layer is determined to be $140 \text{ nm} \pm 4 \text{ nm}$.

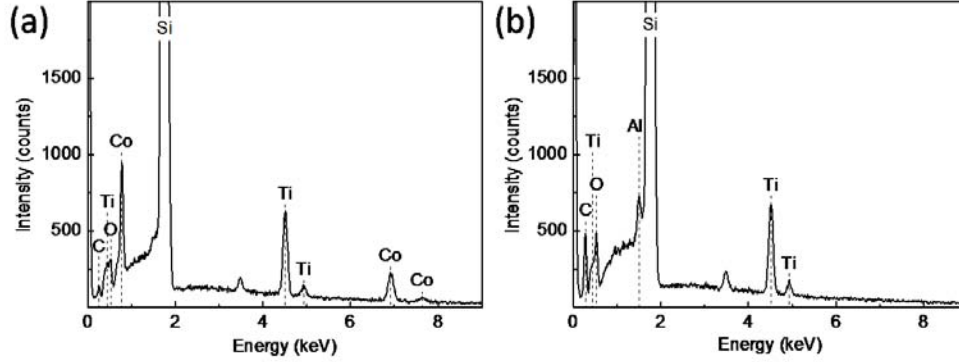


Figure 6.3: EDX spectra of (a) the as-deposited Co SCTF and (b) PMMA iSCTF coated with 5 nm of Al_2O_3 .

Subtracting the thicknesses of 5 nm for Al_2O_3 and 45 nm for Ti, we determine the thickness for PMMA iSCTF to be approximately 90 nm. The top-view image of PMMA iSCTF in Fig. 6.2(d) shows a large number of pores randomly distributed on the sample surface even though the sample is coated with a 8 nm Ti layer. The SEM images of PMMA iSCTF indicate evidently that the PMMA iSCTF and Co SCTF template are structurally complementary to each other. The slanted pores lead to a strong structural anisotropy in PMMA iSCTF. Table 6.1 summarizes the structural parameters for the as-deposited Co SCTF and PMMA iSCTF film

Table 6.1: The structural parameters for the as-deposited Co SCTF and PMMA iSCTF obtained from SEM analysis. t_f : film thickness; θ : the slanting angle; d : the diameter of the Co nanocolumns or slanted pores; t_a : thickness of Ti adhesion layer.

Parameter	SCTF	SCTF+PMMA
t_s (nm)	82 ± 6	90 ± 4
θ ($^\circ$)	61 ± 3	71 ± 3
d (nm)	19 ± 4	12 ± 4
t_a (nm)	37 ± 3	39 ± 2

determined from SEM analysis.

Fig. 6.3(a) and (b) show the EDX spectra of the Co SCTF and PMMA iSCTF coated with Al_2O_3 , respectively. Both spectra display Ti peaks due to the Ti adhesion layer in the samples. The peaks positioned at approximately 3.5 eV in both spectra are pileup signals from Si⁽¹²⁶⁾. The spectrum of PMMA iSCTF in Fig. 6.3(b) shows an increased signal of carbon (C) due to the presence of PMMA and a new signal from aluminum (Al) which is attributed to the thin Al_2O_3 coating. Furthermore, Fig. 6.3(b) shows no signals from Co element (EDX detection limit on transition metals is generally in the order of 0.1 wt%⁽¹⁴⁷⁾), indicating FeCl_3 etching removed the Co slanted columns effectively.

6.3 TAB-EMA Analysis

6.3.1 Experimental and Best-model Calculated Mueller Matrix Data

Fig. 6.4 depicts the experimental and best-model calculated off-diagonal Mueller matrix elements M_{ij} normalized to M_{11} for the samples at each step of the preparation processes as depicted in Fig. 4.1(a): (a) as-deposited Co SCTF; (b) SCTF infiltrated with PMMA; (c) SCTF infiltrated with PMMA after RIE; (d) PMMA iSCTF. Data for the Co SCTF and PMMA-infiltrated SCTFs resemble those presented in chapter 5, thus the diagonal elements for the sample are omitted further for brevity, while off-diagonal elements are discussed below. Comparing (a) and (b), we can see the variation of the off-diagonal elements again showing large differences after infiltration, indicative of the changes in the optical anisotropy due to polymer filling. However, the data for the two hybridized samples in (b) and (c) show very similar variation patterns, which suggests that the optical anisotropy is unchanged after RIE etching.

The off-diagonal Mueller matrix elements for the Co SCTF template and PMMA iSCTF are compared in Fig. 6.5. The experimental off-diagonal elements of Co SCTF show a two-fold rotational symmetry versus sample azimuth ϕ . The two pseudoisotropic sample orientations of Co SCTF with $M_{ij} \approx 0$ are present at

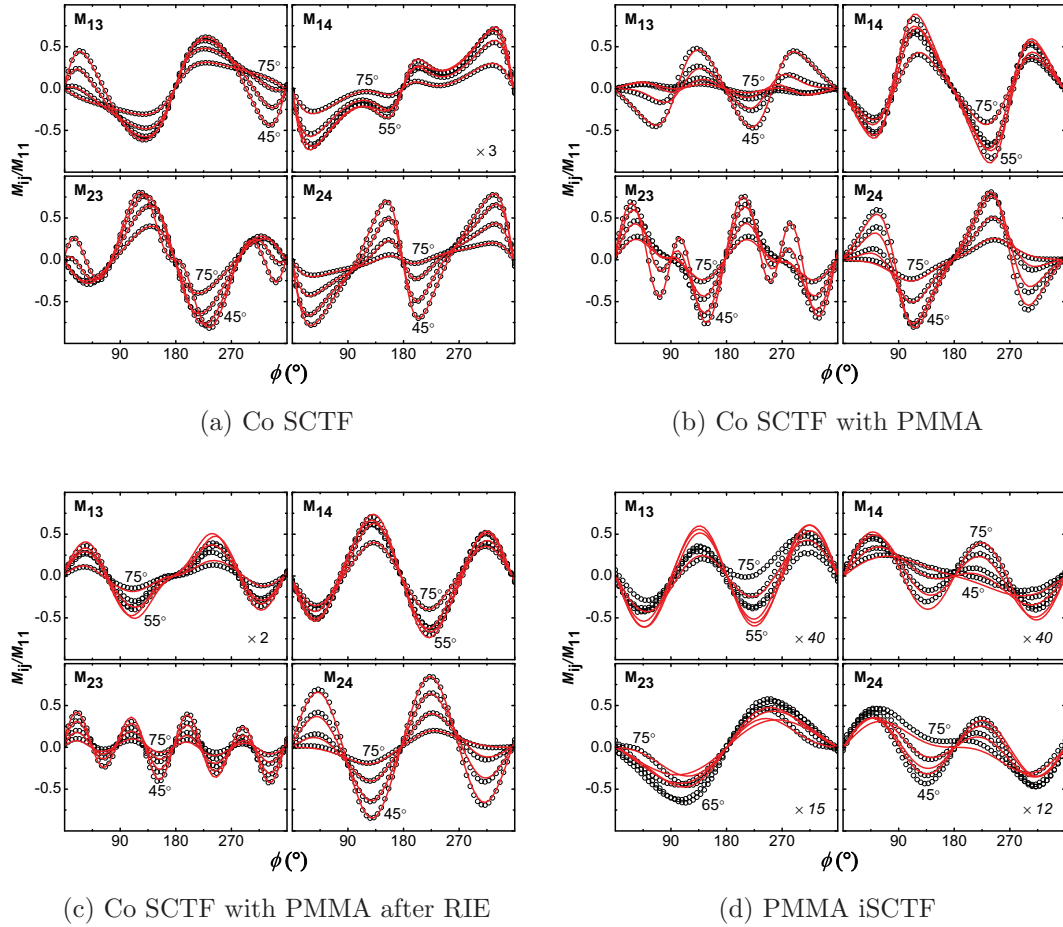


Figure 6.4: Experimental (open circles) and best-model calculated (solid lines) off-diagonal Mueller matrix elements M_{ij} normalized to M_{11} for the samples versus azimuth ϕ and angle of incidence $\Phi_a = 45^\circ, 55^\circ, 65^\circ, 75^\circ$ at $\lambda = 485$ nm: (a) as-deposited Co SCTF; (b) SCTF infiltrated with PMMA; (c) SCTF infiltrated with PMMA after RIE; (d) PMMA iSCTF. The symbols in the blocks denote the multiplications.

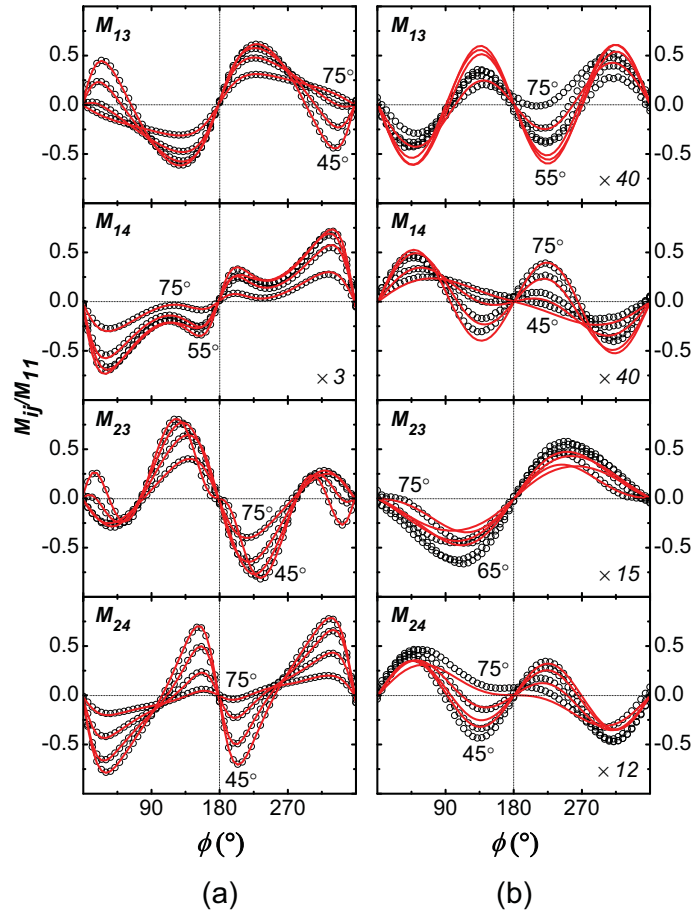


Figure 6.5: Experimental (open circles) and best-model calculated (solid lines) off-diagonal Mueller matrix elements M_{ij} normalized to M_{11} versus sample azimuth ϕ and angle of incidence $\Phi_a = 45^\circ, 55^\circ, 65^\circ, 75^\circ$ at $\lambda = 485$ nm. Columns (a) and (b) show the GE data for the as-deposited Co SCTF and PMMA iSCTF, respectively. Note that M_{14} for the Co SCTF and M_{ij} for the PMMA iSCTF are scaled up. The symbols in the lower right corner of the blocks denote the multiplication.

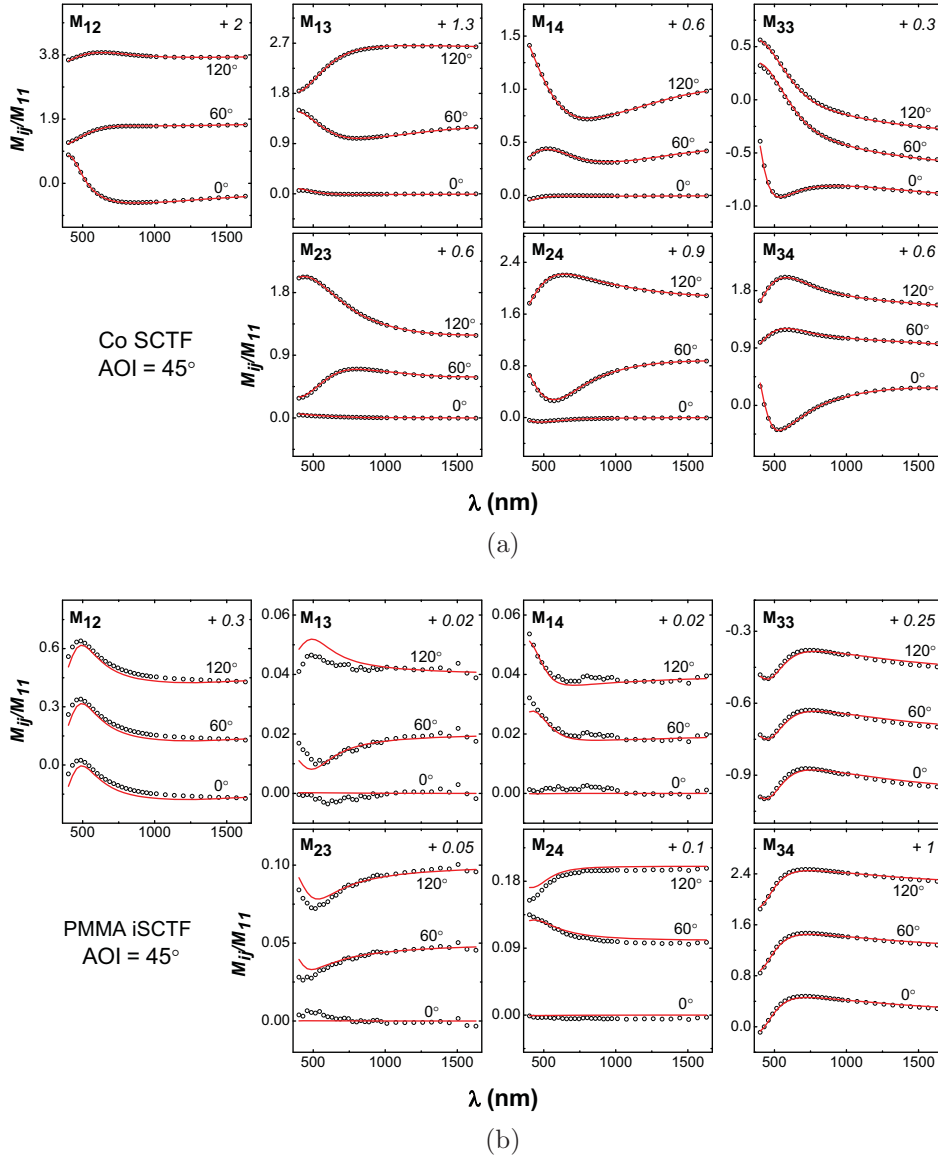


Figure 6.6: Experimental (open circles) and best-model calculated (solid lines) Mueller matrix elements M_{ij} normalized to M_{11} at angle of incidence $\Phi_a = 45^\circ$ for three different sample azimuths $\phi = 0^\circ, 60^\circ, 120^\circ$ within spectral range from 400 to 1650 nm: (a) Co SCTF; (b) PMMA iSCTF. The Mueller matrix data are presented by stack plots. For each stack plot, M_{ij} at $\phi = 0^\circ$ is set as the baseline data and a constant offset is added up to the data at followed ϕ . The number at the upper right corner of each block denotes the offset.

$\phi \approx 0^\circ$ and $\phi \approx 180^\circ$, where the plane of incidence is parallel to the nanocolumn orientation. Compared to the SCTF template, the magnitudes of the off-diagonal elements and their variation versus sample azimuth ϕ are substantially decreased for PMMA iSCTF, which discloses a large reduction of optical anisotropy within PMMA iSCTF. However, the data for PMMA iSCTF still show a similar symmetry versus ϕ . The off-diagonal elements reveal an optical anisotropy within PMMA iSCTF since otherwise these elements are zero. This optical anisotropy results from the anisotropic structure which consists of highly oriented nanopores within PMMA matrix as shown in the SEM image (Fig. 6.2(b)). The two pseudoisotropic orientations for PMMA iSCTF remain positioned at $\phi \approx 0^\circ$ and $\phi \approx 180^\circ$ approximately, which indicates that after etching SCTF template the pores within PMMA preserve the slanted nanocolumnar structure and the slanted pores are oriented parallel to the plane of incidence at two pseudoisotropic orientations. The similarities in the off-diagonal Mueller matrix data reveal that the PMMA iSCTF resembles Co SCTF template in the anisotropic optical response.

Fig. 6.6 shows how the spectral Mueller matrix element data for the two samples vary with different sample azimuths. In order to distinguish the decreased M_{ij} for PMMA iSCTF at different azimuths, the data are plotted as stacks with offsets for three azimuths $\phi = 0^\circ, 60^\circ, 120^\circ$, and M_{ij} at $\phi = 0^\circ$ is set as the baseline data. It is noted that the diagonal elements (M_{12}, M_{33}, M_{34}) for PMMA iSCTF show nearly identical wavelength dependency for three different azimuths. In the off-diagonal element spectra, it is seen clearly that the data at $\phi = 0^\circ$ vanish to zero over the entire spectral range. At the other two azimuths, the off-diagonal elements for PMMA iSCTF exhibit a large variation against λ especially in the short wavelength range, further indicating the anisotropic optical response within PMMA iSCTF. From both Fig. 6.5 and Fig. 6.6, the best-model calculated data for Co SCTF are in excellent agreement with experimental data. For PMMA iSCTF, the experimental off-diagonal element spectra become less smooth and small differences can be seen between the experimental and calculated data, which could be due to that such small signals nearly reach the detection limit of the ellipsometer. However, the best-model calculation matches the data signatures versus sample

azimuth and angle of incidence excellently as shown in Fig. 6.5. In Fig. 6.6, the calculated spectral data also show a good agreement with the experimental data.

6.3.2 Structural Properties

Table 6.2 shows the structural parameters determined by the best-model analysis of the TAB-EMA for the samples at each step of the preparation processes. The best-model results represent the averaged physical properties over the measured spot on the samples. The error bars in the table denote the finite uncertainty

Table 6.2: The best-model parameters obtained from TAB-EMA: (a) as-deposited Co SCTF; (b) SCTF infiltrated with PMMA; (c) SCTF infiltrated with PMMA after RIE; (d) PMMA iSCTF. t_f : film thickness; t_p : thickness of top PMMA layer; t_a : thickness of Ti adhesion layer; β : the angle between \mathbf{b} and \mathbf{c} ; θ : the slanting angle; f_v : the volume fraction of void; f_{Co} : the volume fraction of Co nanocolumns; f_p : the volume fraction of PMMA; L_j : depolarization factor along each major axis.

	(a)	(b)	(c)	(d)
	SCTF	SCTF/PMMA	After RIE	PMMA iSCTF
t_f (nm)	83.07(8)	85.12(7)	85.80(8)	95.9(1)
t_p (nm)	N/A	21.18(7)	0.22(8)	N/A
t_a (nm)	31.29(8)	27.38(7)	27.98(7)	34.8(1)
β ($^\circ$)	90.03(4)	91.90(5)	92.09(5)	90 (fixed)
θ ($^\circ$)	59.68(1)	68.60(5)	69.00(5)	70.5(7)
f_v (%)	78.96(2)	0	0	36.6(2)
f_{Co} (%)	21.04(2)	16.6(1)	16.3(1)	0.15(1)
f_p (%)	N/A	83.4(1)	83.7(1)	63.2(2)
L_a	0.4112(4)	0.3723(6)	0.3683(6)	0.456(4)
L_b	0.5096(4)	0.6059(6)	0.6059(6)	0.320(4)
L_c	0.0792(6)	0.0218(3)	0.0259(3)	0.224(3)
MSE	33.1	69.4	68.3	129.5

which is related to the measurement accuracy and best-model calculation process. From the results for the SCTF infiltrated with PMMA, it is found that the nanocolumnar slanting angle increases from 60° to 69° , which reveals a further inclination of nanocolumns after infiltration. The void fraction decreased significantly to zero is indicative of an excellent infiltration. From the results after RIE, it can be seen that all the structural parameters for SCTF with PMMA are almost identical to those before RIE, aside from the top PMMA layer thickness decreased to nearly zero. This result indicate that the RIE etching is carefully controlled such that only the top PMMA layer is removed, whereas the SCTF structure and PMMA infiltration underneath are intact. The preserved structural properties after RIE lead to the unchanged anisotropic optical response as shown in Fig. 6.4(b) and (c).

The obtained structural parameters for the Co SCTF template and PMMA iSCTF are mainly compared and discussed. The best-model results for the Co SCTF show a film thickness of 83 nm and slanting angle of 60° approximately, which are highly consistent with the values found via SEM analysis (82 nm and 61° , respectively). The slanting angle of the PMMA iSCTF is determined to be 70° which is in good agreement with SEM result showing $\theta \approx 71^\circ$. The thickness of the iSCTF given by best-model is 96 nm which is slightly above the SEM result with $t_f \approx 90$ nm. The parameter t_a values for both samples are consistent with the SEM analysis. The best-model results for the iSCTF reveal that the Co volume fraction parameter is decreased significantly from 21.04% to 0.15% which is consistent with the vanished Co EDX signal in Fig. 6.3(b). The PMMA fraction is the largest with 63.2% indicating PMMA becomes the main constituent in this iSCTF. The void fraction is determined to be 36.6% by the best-model which confirms the porous structure within the film. Comparing to the depolarization factors of the Co SCTF, it is found that for the PMMA iSCTF L_b decreases and L_c increases while the change in L_a is relatively small, but L_c still shows the lowest value compared with L_a and L_b , indicative of a cylindrical pore shape elongated along **c** axis. We find that β is approximately 90° for both Co SCTF and iSCTF, and thus both films reveal orthorhombic optical anisotropy along axes **a**, **b** and **c**.

6.3.3 Anisotropic Optical Properties

Fig. 6.7 depicts the effective optical constants along the three major axes of the as-deposited Co SCTF and PMMA iSCTF which are determined by the best-model calculation based on the TAB-EMA. The optical constants of the Co SCTF along axis \mathbf{c} show strongest wavelength dependency, The structure of optical anisotropy follows $n_c > n_a > n_b$ in the near-infrared spectral region (above 800 nm) and $k_c > k_a > k_b$ over the entire spectrum. For the PMMA iSCTF, the optical constants along each axis are decreased substantially due to the removal of Co nanocolumns. The ultra low extinction coefficients are attributed to the low volume fraction of Co and are indicative of high transparency over the spectral range. The refractive indices of the PMMA iSCTF along each axis show a small wavelength dependency similar to that of the solid PMMA film obtained by a Cauchy model. n_a , n_b and n_c are lower than the refractive indices of the solid PMMA film (between 1.49 and 1.51 approximately), which reflects the porous structure within the iSCTF. The structure for optical anisotropy becomes $n_c > n_a > n_b$ in the entire spectral range, thus \mathbf{c} remains as the axis of the PMMA iSCTF for which the largest dielectric polarizability occurs. For ease of comparison, the effective refractive indices of Si SCTF ($t_f = 109$ nm, $\beta = 88^\circ$ and $\theta = 62^\circ$) which is nearly lossless in this spectral range are exhibited in Fig. 6.7⁽¹³⁵⁾. It is noted that $n_c > n_a > n_b$ holds over the entire spectral range for Si SCTF. Therefore, our results indicate that the samples with complementary physical structures possess identical structure for optical anisotropy.

Fig. 6.8 depicts the birefringence for the as-deposited Co SCTF, PMMA iSCTF and Si SCTF which is presented as the difference of the refractive indices between the major axes extracted from the TAB-EMA. Instead of a strong wavelength dependency as for the Co SCTF, the birefringence for PMMA iSCTF is reduced substantially and becomes nearly constant over the entire spectral range, which is because the refractive indices along each axis show weak wavelength dependency after removing the Co nanocolumns (shown in the right column of Fig. 6.7). For Co SCTF, Δn_{c-a} and Δn_{c-b} vanish at 750 nm approximately, but for PMMA iSCTF Δn_{c-a} , Δn_{c-b} and Δn_{b-a} stabilize at certain non-zero values in the entire spectral range. Δn_{c-b} shows the largest value at 0.022 approximately. In the

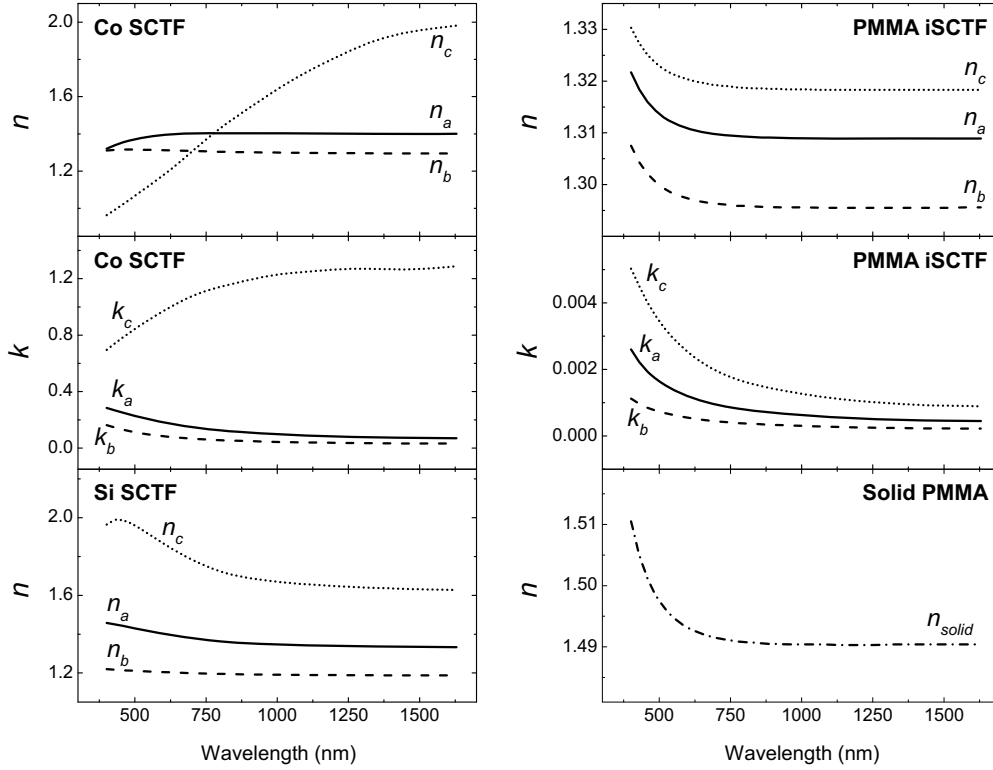


Figure 6.7: Effective optical constants, n_j and k_j ($j = a, b, c$), along the major axes **a** (solid lines), **b** (dashed lines) and **c** (dotted lines) determined by the TAB-EMA for the as-deposited Co SCTF and PMMA iSCTF. n_j for the Si SCTF and refractive indices for the solid PMMA film are shown in the bottom blocks of each column for comparison.

near-infrared range where Si has little absorption, the birefringence also becomes nearly constant for Si SCTF. Similarly, Si SCTF has no vanished birefringence over the entire spectral range with Δn_{c-b} being the largest. From the results above, it is indicated that PMMA iSCTF has similar birefringence behavior with the slanted nanocolumns.

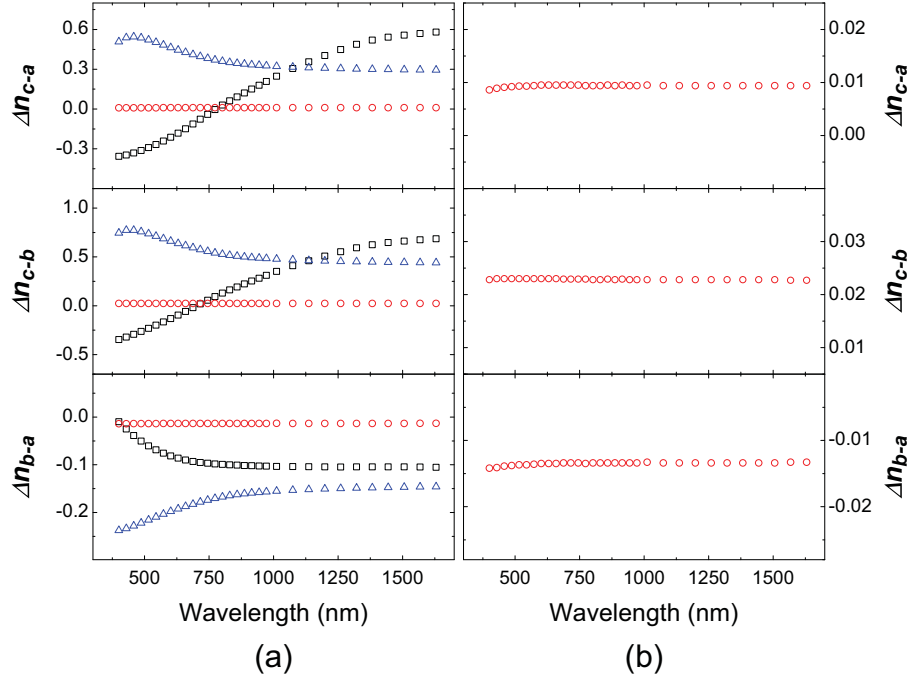


Figure 6.8: The birefringence between the major axes for the as-deposited Co SCTF (square), PMMA iSCTF (circle) and Si SCTF (triangle) is depicted in column (a). Column (b) shows the the birefringence for PMMA iSCTF in reduced scale for clear view. The refractive indices n_j along the major axes ($j = a, b, c$) are extracted from the TAB-EMA best-model calculation and the birefringence is represented by the difference of n_j between the axes: $\Delta n_{c-a} = n_c - n_a$; $\Delta n_{c-b} = n_c - n_b$; $\Delta n_{b-a} = n_b - n_a$.

6.3.4 Discussion

From the best-model results in Table 6.2, it is noted that the slanting angle θ of the PMMA iSCTF is larger than that of the as-deposited Co SCTF. Upon PMMA infiltration via spin-coating, the nanocolumns may incline further to the substrate due to the polymer shrinkage⁽¹³⁴⁾. After FeCl_3 etching, the nanopores preserve the shape of the inclined nanocolumns, therefore possessing an increased θ . The ultra low volume fraction for Co in PMMA iSCTF given by the model is consistent with the EDX results in Fig. 6.3(b) showing no distinguishable signal

from Co element. Since a detection limit on transition metals exists in the order of 0.1 wt%⁽¹⁴⁷⁾, the Co fraction is still included in the TAB-EMA to account for the residual Co component after FeCl₃ etching. Ideal etching on SCTF template could result in a void fraction for the PMMA iSCTF equal to the Co volume fraction of the as-deposited SCTF. f_v for PMMA iSCTF is larger than f_{Co} for the as-deposited SCTF. This disagreement indicates that a small amount of PMMA was removed along with Co nanocolumns during the FeCl₃ etching. The difference of the depolarization factors between the two samples can be explained by the difference in slanting angle. The increased L_c of the PMMA iSCTF could be due to the further inclination of the nanopores towards the substrate surface than the as-deposited nanocolumns, where L_c approaches zero with the infinite columnar structures perpendicular to the substrate, while approaching unity with such columns parallel to the substrate⁽¹⁰⁷⁾. The reduction in L_b can be explained by the smaller space along **b** resulting from the larger slanting angle. Since the larger slanting angle has limited effect on the interspace along **a**, the change in L_a is relatively small.

For the monoclinic optical system, the Euler angles such as θ become wavelength-dependent, because they depend explicitly on the wavelength-dependent dielectric functions along three axes.^(107,131) However, Fig. 6.7 shows a weak wavelength dependency of the effective refractive indices for PMMA iSCTF, thus the wavelength-dependency of the Euler angles for the monoclinic system can be hardly revealed by the GE analysis in the spectral range of interest here. Instead, the biaxial optical properties for PMMA iSCTF are determined to be orthorhombic. In Fig. 6.7 and 6.8, the PMMA iSCTF and Si SCTF show the resemblance in biaxial optical properties. This result reveals that the anisotropic optical behaviors for the two samples may be analogous to the reciprocity theorem. According to the general definition, the reciprocity theorem represents the reciprocal relations for systems of sources in which one source and another source are interchangeable without altering the response of the systems to either source.⁽¹⁴⁸⁾ In the present work, the system is composed of two complementary structures with different electric dipole distributions: slanted nanopores embedded in polymers and slanted nanocolumns embedded in voids. The dipole radiation

due to the incident light is the source for the optical response of materials.⁽¹²⁹⁾ When the SCTFs are present, the anisotropic optical response results from the dipoles within the slanted nanocolumns. When the slanted nanopores replace nanocolumns, dipole radiation of the polymer surrounding the hollow cores becomes the source. Our TAB-EMA results demonstrate that the two dipole sources within each structure can be interchanged, while the classification and structure for optical anisotropy are identical. Therefore, and notwithstanding that different materials produce different absolute values of optical constants, the PMMA iSCTFs and SCTFs exhibit a reciprocal relation in anisotropic optical behavior. The similarities in Mueller matrix data also reveal this reciprocity.

6.4 RAB-EMA Analysis

The structural parameters obtained from RAB-EMA are shown and compared with TAB-EMA results in Table 6.3. The two AB-EMA formalisms show good agreement on the thicknesses, slanting angle and constituent fractions with TAB-EMA. The closeness of MSE indicate both AB-EMA formalisms produce same quality of match to the experimental Mueller matrix data. For the depolarization factors, both formalisms deliver the smallest values along **c**, but $L_a > L_b$ obtained from TAB-EMA while $L_a < L_b$ from RAB-EMA. Since the depolarization factors depend on the shape of the columnar nanopores embedded in PMMA matrix, different orders for L_a and L_b indicate the two formalisms give different results on pore geometry along **a** and **b**. However, both formalisms are consistent in the elongated pore structure along **c**.

In Fig. 6.9, the effective optical constants along each major axis for the PMMA iSCTF obtained from the RAB-EMA and TAB-EMA show excellent agreement. Such agreement can also be obtained in the results for Si SCTF⁽¹³⁵⁾. But for lossy metal (*e.g.*, Co, Ti and permalloy) SCTFs, the RAB-EMA and TAB-EMA deliver different results on the principal biaxial optical constants⁽¹³⁵⁾. Thus it is indicated that for lossless or nearly lossless materials, such as PMMA and Si nanostructured films, the two AB-EMA formalisms can produce very close results for the effective optical constants as well as the structural parameters. According to Eq. 3.34

for the RAB-EMA, the depolarization factor along each axis is function of the dielectric constants and becomes wavelength-dependent, while these factors are wavelength-independent for the TAB-EMA. For the lossy materials which have strong dispersion in the optical constants, the difference in the results between the two formalisms can be large. However, for the materials with low or vanished extinctive coefficients such as dielectric polymers, the wavelength-dependent effect becomes small for the RAB-EMA depolarization factors, therefore the two formalisms can deliver very similar results.

Table 6.3: The best-model parameters obtained from RAB-EMA and TAB-EMA for PMMA iSCTF. t_f : film thickness; t_a : thickness of Ti adhesion layer; β : the angle between \mathbf{b} and \mathbf{c} ; θ : the slanting angle; f_v : the volume fraction of void; f_{Co} : the volume fraction of Co nanocolumns; f_p : the volume fraction of PMMA; L_j : depolarization factor along each major axis. The error bars given in parentheses denote the numerical uncertainty of the last digit (90% confidence interval). Note that the D_j values determined by the RAB-EMA are converted according to the definition of L_j of the TAB-EMA as shown in Eq. 3.29.

Parameter	RAB-EMA	TAB-EMA
t_f (nm)	95.81(4)	95.9(1)
t_a (nm)	34.83(9)	34.8(1)
β ($^\circ$)	90 (fixed)	90 (fixed)
θ ($^\circ$)	69.2(5)	70.5(7)
f_v (%)	36.26(1)	36.6(2)
f_{Co} (%)	0.16(1)	0.15(1)
f_p (%)	63.58(1)	63.2(2)
L_a	0.34(3)	0.456(4)
L_b	0.45(2)	0.320(4)
L_c	0.22(3)	0.224(3)
MSE	129.6	129.5

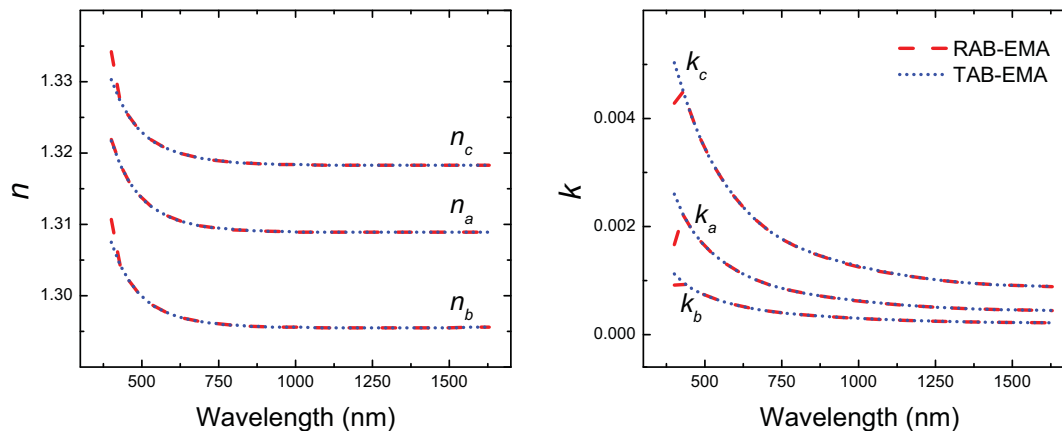


Figure 6.9: Effective optical constants along the major axes **a**, **b** and **c** of the PMMA iSCTF determined by the RAB-EMA (dashed lines) and TAB-EMA (dotted lines): n_j and k_j ($j = a, b, c$)

6.5 Conclusion

The anisotropic structural and optical properties of the PMMA iSCTFs and SCTF templates are obtained via GE. The PMMA iSCTFs were obtained by spin-coating PMMA onto the Co SCTFs and subsequent wet etching of the Co templates. The TAB-EMA is utilized to analyze the measured GE data measured on the samples at each step of the preparation processes. The obtained TAB-EMA parameters allow for monitoring the structural changes at each step, such as infiltration and top polymer layer thickness. For the PMMA iSCTFs and SCTF templates, the modeling results on film thickness and slanting angle are in good agreement with SEM analysis. The TAB-EMA delivers an ultra low Co fraction for PMMA iSCTFs which is consistent with the EDX results. The porosity of PMMA iSCTFs with anisotropic pore structure is also determined.

The optical property results for PMMA iSCTFs show that optical constants along each axis are decreased substantially as well as the wavelength-dependency. The refractive indices lower than the values for bulk PMMA indicate the porous structure within the sample. The optical anisotropy revealed by GE for the

PMMA iSCTFs and SCTF templates is further compared. The off-diagonal Mueller matrix elements of the two samples exhibit a similar symmetry versus sample azimuth and identical pseudoisotropic sample orientations. The biaxial optical properties are determined to be orthorhombic for both samples. The PMMA iSCTFs and SCTFs possess the same order for the effective refractive indices with largest values along \mathbf{c} axis, and show resemblance in birefringence. The identical class and structure for optical anisotropy indicate that the anisotropic optical behaviors for the two complementary structures are in accordance with reciprocity theorem in electrodynamics.

The structural parameters and principal biaxial optical constants obtained from the two AB-EMA formalisms show excellent agreement for PMMA iSCTFs, which is attributed to the small wavelength-dependency in the optical constants for polymer.

Chapter 7

Summary and Outlook

In the present thesis, GE is demonstrated to be an effective characterization methodology to determine the structural and optical properties for two types of anisotropic nanoporous media: the SCTFs infiltrated with polymers and inverse-SCTF porous polymer films. The SCTFs prepared with GLAD were infiltrated with PMMA via spin-coating. The porous polymer films were prepared with infiltrating PMMA into porous SCTFs and subsequent removal of the SCTF templates. The GE modeling approaches were employed to analyze the Mueller matrix element data measured on the samples from visible to near-infrared spectral range.

The changes in the structural and anisotropic optical properties for the SCTFs due to infiltration are determined with the GE modeling approach combining the HBLA and two formalisms of AB-EMA. The HBLA was utilized to analyze the Mueller matrix data to identify a decreased film thickness and larger slanting angle which conform with the geometry calculation based on a further bending of the nanocolumns. The significant changes in the biaxial optical properties such as effective principal optical constants are also quantitatively determined with the HBLA. It is found that the polymer infiltration and nanocolumnar bending contribute to the optical property changes. In order to evaluate the constituent fraction changes, two formalisms of AB-EMA, traditional AB-EMA and rigorous AB-EMA, are employed in two different analysis procedures. In the first procedure, the effective optical constants along major axes are used as the analysis data for the AB-EMA. A high level of infiltration is indicated in the results. The increased permalloy fraction shows good agreement with the geometry calculation.

In the second procedure, the two AB-EMA formalisms are utilized to directly analyze the Mueller matrix data. The results also reveal a further columnar inclination and increased permalloy fraction after infiltration. However, the HBLA is considered to be the primary method for determining the biaxial optical properties including principal optical constants and monoclinic angle.

The structural and optical properties of the porous PMMA films with inverse SCTF structure (PMMA iSCTFs) are further investigated with the AB-EMA modeling of GE data. In the AB-EMA, the slanted columnar pores are assumed to be highly oriented within the PMMA matrix which is the inverse structure of the template. This model scenario is consistent with the SEM observation. The structural parameters such as film thickness, slanting angle and void fraction are in good agreement with the SEM and EDX results. This section focuses on the relation of optical anisotropy between the PMMA iSCTFs and SCTF templates which are structurally complementary. The off-diagonal Mueller matrix data for PMMA iSCTFs show resemblance in azimuth symmetry and pseudoisotropic orientation to those for the SCTFs. The classification of the optical anisotropy for both samples are determined to be orthorhombic. The effective optical constants along each axis of the samples also follow the same order, which reveals an identical anisotropy structure. Therefore, the anisotropic optical behaviors for the two complementary structures exhibit a reciprocal relation.

The GE analysis approach developed for the SCTFs upon infiltration opens great possibility for future research on hybridized SCTFs. For instance, polymeric composites with magnetic nanoparticles can be infiltrated into the porous regions of SCTFs prepared from magnetic materials. It is a subject of interest to use magneto-optical generalized ellipsometry (MOGE) to study the changes in the anisotropic MO responses for the magnetic SCTFs due to nanoparticles^(149–152). The present approach delivers the biaxial optical properties of SCTFs which will be the basis for further analysis on MO effects. In addition, this approach is proposed to be used for the SCTF sensing devices, since the constituent fraction evaluation allows for quantitative determination on the analytes attached onto SCTFs. Finally, the application of the GE analysis can be extended to characterize other hybridized columnar systems, such as highly oriented nanorods or

nanotubes. For instance, GE analysis will be particularly useful to evaluate the structure and hybridization degree for hybrid photovoltaic materials composed of conjugated polymer and inorganic nanocolumns^(20,23,153).

The GE analysis with the AB-EMA can be considered as a versatile and non-destructive method for studying the porosity, pore shape and optical anisotropy of porous polymer films with complex 3-D pore structures. Future research is proposed to utilize this approach to characterize porous polymers with highly-ordered cylindrical pores prepared from template or self-assembly methods⁽²⁸⁾. Such cylindrical pore structure leads to birefringence within polymer films which can have potential application in optical retarding elements. GE analysis will be an effective method to measure the polymeric birefringence. Additionally, GE can be incorporated into ellipsometry porosimetry (EP) technology to determine the pore size distribution for anisotropic porous polymers. Current EP only uses standard ellipsometry measurements and isotropic optical model for data analysis^(72,73,83,87). Instead, the GE analysis with the AB-EMA adapts the Mueller matrix element measurements and considers the form-induced anisotropy, which allows for an accurate determination of the polymeric porous properties.

References

- [1] Davis, M. E. *Nature* **417**, 813 (2002). [1](#)
- [2] Wang, G., Zhang, L., and Zhang, J. *Chem. Soc. Rev.* **41**, 797 (2012). [1](#)
- [3] Birner, A., Wehrspohn, R. B., Gösele, U. M., and Busch, K. *Adv. Mater.* **13**, 377 (2001). [1](#)
- [4] Joo, W., Park, M. S., and Kim, J. K. *Langmuir* **22**, 7960 (2006). [1](#)
- [5] Knez, M., Nielsch, K., and Niinistö, L. *Adv. Mater.* **19**, 3425 (2007). [1](#), [3](#)
- [6] Kemell, M., Pore, V., Tupala, J., Ritala, M., and Leskela, M. *Chem. Mater.* **19**, 1816 (2007).
- [7] Tan, L. K., Chong, M. A. S., and Gao, H. *J. Phys. Chem. C* **112**, 69 (2008). [1](#), [3](#)
- [8] Zhao, Y., Ye, D., Wang, G., and Lu, T. *Proceedings of SPIE* **5219**, 59 (2003). [2](#), [12](#)
- [9] Hawkeye, M. M. and Brett, M. J. *J. Vac. Sci. Technol. A* **25**, 1317 (2007). [2](#), [6](#), [11](#), [12](#), [13](#)
- [10] Robbie, K. and Brett, M. J. *J. Vac. Sci. Technol. A* **15**, 1460 (1997). [12](#)
- [11] Demirel, G., Malvadkar, N., and Demirel, M. C. *Thin Solid Films* **518**, 4252 (2010). [2](#)

- [12] Kesapragada, S. V., P., V., Nalamasu, O., and Gall, D. *Nano Lett.* **6**, 854 (2006). [2](#)
- [13] Harris, K. D., Huzinga, A., and Brett, M. J. *Electrochem. Solid-State Lett.* **5**, H27 (2002).
- [14] Steele, J. J., Gospodyn, J. P., Sit, J. C., and Brett, M. J. *IEEE Sens. J.* **6**, 24 (2006). [2](#)
- [15] Kennedy, S. R. and Brett, M. J. *Appl. Opt.* **42**, 4573 (2003). [2](#)
- [16] Toader, O. and John, S. *Science* **292**, 1133 (2001). [2](#)
- [17] Hodgkinson, I. and Wu, Q. h. *Adv. Mater.* **13**, 889 (2001). [2](#)
- [18] Hrudey, P. C. P., Szeto, B., and Brett, M. J. *Appl. Phys. Lett.* **88**, 251106 (2006).
- [19] Robbie, K., Cui, Y., Elliott, C., and Kaminska, K. *Appl. Opt.* **45**, 8298 (2006). [2](#)
- [20] Gerein, N. J., Fleischauer, M. D., and Brett, M. J. *Sol. Energ. Mat. Sol. C.* **94**, 2343 (2010). [2](#), [96](#)
- [21] Lakhtakia, A., McCall, M. W., Sherwin, J. A., Wu, Q. H., and Hodgkinson, I. *Opt. Commun.* **194**, 33 (2001). [2](#)
- [22] Robbie, K., Broer, D. J., and Brett, M. J. *Nature* **399**, 764 (1999). [2](#)
- [23] Bouclé, J., Ravirajanac, P., and Nelson, J. *J. Mater. Chem.* **17**, 3141 (2007). [2](#), [96](#)
- [24] Coakley, K. M., Liu, Y., McGehee, M. D., Frindell, K. L., and Stucky, G. D. *Adv. Funct. Mater.* **13**, 301 (2003). [2](#)
- [25] Karabacak, T., Wiegand, C., Senkevich, J., Lu, T., Jia, D. D., and Fernandez, F. *Electrochem. Solid-State Lett.* **7**, H36 (2004). [2](#)
- [26] Sherwin, J. A. and Lakhtakia, A. *Opt. Commun.* **214**, 231 (2002).

- [27] Steele, J. J., Popta, A. C. V., Hawkeye, M. M., Sit, J. C., and Brett, M. J. *Sensor Actuat. B-Chem.* **120**, 213 (2006). [2](#)
- [28] Wu, D. C., Xu, F., Sun, B., Fu, R., He, H., and Matyjaszewski, K. *Chem. Rev.* **112**, 3959 (2012). [3](#), [19](#), [96](#)
- [29] Tao, Y., Kanoh, H., Abrams, L., and Kaneko, K. *Chem. Rev.* **106**, 896 (2006). [5](#)
- [30] Lu, A. H. and Schüth, F. *Adv. Mater.* **18**, 1793 (2006).
- [31] D., V. O. and Kaler, E. W. *Adv. Mater.* **12**, 531 (2000).
- [32] Barton, T. J., Bull, L. M., Klemperer, W. G., Loy, D. A., McEnaney, B., Misono, M., Monson, P. A., Pez, G., Scherer, G. W., Vartuli, J. C., and Yaghi, O. M. *Chem. Mater.* **11**, 2633 (1999). [3](#)
- [33] Hillmyer, M. A. *Adv. Polym. Sci.* **190**, 137 (2005). [3](#)
- [34] Park, S., Wang, J. Y., Kim, B., and Russell, T. P. *Nano Lett.* **8**, 1667 (2008).
- [35] Hamley, I. W. *Nanotechnology* **14**, R39 (2003).
- [36] Olson, D. A., Chen, L., and Hillmyer, M. A. *Chem. Mater.* **20**, 869 (2008). [3](#)
- [37] Stein, A. and Schroden, R. C. *Curr. Opin. Solid State Mater. Sci.* **5**, 553 (2001). [4](#)
- [38] Hu, X., An, Q., Li, G., Tao, S., and Liu, J. *Angew. Chem. Int. Ed.* **45**, 8145 (2006).
- [39] Gorey, B., Smyth, M. R., White, B., and Morrin, A. *J. Mater. Chem. C* **2**, 6004 (2014). [4](#)
- [40] Li, G. L., Liu, G., Kang, E. T., Neoh, K. G., and Yang, X. L. *Langmuir* **24**, 9050 (2008). [4](#)

- [41] Yang, X., Chen, L., Huang, B., Bai, F., and Yang, X. L. *Polymer* **50**, 3556 (2009).
- [42] Fu, G. D., Li, G. L., Neoh, K. G., and Kang, E. T. *Prog. Polym. Sci.* **36**, 127 (2011).
- [43] Wu, Q., Wang, Z., and Xue, Q. *Adv. Funct. Mater.* **17**, 1784 (2007). 4
- [44] Martin, C. R. *Chem. Mater.* **8**, 1739 (1996). 4
- [45] Stainhart, M., Wehrspohn, R. B., Gösele, U., and Wendorff, J. H. *Angew. Chem. Int. Ed.* **43**, 1334 (2004).
- [46] Lee, W., Jin, M. K., Yoo, W. C., and Lee, J. K. *Langmuir* **20**, 7665 (2004).
- [47] Lee, W. and Park, S. J. *Chem. Rev.* **114**, 7487 (2014). 4
- [48] Davis, M. E. *Nature* **417**, 813 (2002). 4
- [49] Liu, Y., Goebela, J., and Yin, Y. *Chem. Soc. Rev.* **42**, 2610 (2013).
- [50] Fu, G. D., Shang, Z., Hong, L., Kang, E. T., and Neoh, K. G. *Adv. Mater.* **17**, 2622 (2005). 4
- [51] Huang, J., Tao, C. A., An, Q., Zhang, W., Wu, Y., Li, X., Shen, D., and Li, G. *Chem. Commun.* **46**, 967 (2010). 4, 8
- [52] Li, X., Gao, J., Xue, L., and Han, Y. *Adv. Funct. Mater.* **20**, 259 (2010). 4
- [53] Ibn-Elhaj, M. and Schadt, M. *Nature* **410**, 796 (2001). 4
- [54] Harris, K. D., Sit, J. C., and Brett, M. J. *IEEE Trans. Nanotechnol.* **1**, 1 (2002). 4, 8
- [55] Walheim, S., Schäffer, E., Mlynek, J., and Steiner, U. *Science* **283**, 520 (1999). 4
- [56] Hiller, J., Mendelsohn, J. D., and Rubner, M. F. *Nature* **1**, 59 (2002).
- [57] Joo, W., Kim, H. J., and Kim, J. K. *Langmuir* **26**, 5110 (2010). 4

- [58] Hsiao, V. K. S., Kirkey, W. D., Chen, F., Cartwright, A. N., Prasad, P. N., and Bunning, T. J. *Adv. Mater.* **17**, 2211 (2005). 4
- [59] Shi, J., Hsiao, V. K. S., Walker, T. R., and Huang, T. J. *Nanotechnol.* **18**, 465501 (2007).
- [60] Shi, J., Hsiao, V. K. S., and Huang, T. J. *Sens. Actuators B* **129**, 391 (2008).
- [61] Li, Y., Cunin, F., Link, J. R., Gao, T., Betts, R. E., Reiver, S. H., Chin, V., Bhatia, S. N., and Sailor, M. J. *Science* **299**, 2045 (2003).
- [62] Hu, X., Li, G., Li, M., Huang, J., Li, Y., Gao, Y., and Zhang, Y. *Adv. Funct. Mater.* **18**, 575 (2008). 4
- [63] Sing, K. S. W. *Colloids and Surfaces A: Physicochem. Eng. Aspects* **241**, 3 (2004). 5
- [64] Thommes, M. *Chem. Ing. Tech.* **82**, 1059 (2010). 5
- [65] Hruday, P. C. P., Westra, K. L., and Brett, M. J. *Adv. Mater.* **18**, 224 (2006). 5
- [66] Xu, T., Stevens, J., Villa, J. A., Goldbach, J. T., Guarini, K. W., Black, C. T., Hawker, C. J., and Russell, T. P. *Adv. Funct. Mater.* **13**, 698 (2003).
- [67] Jiang, H., Zhao, W., Li, C., and Wang, Y. *Soft Matter* **7**, 2817 (2011). 5
- [68] Dourdain, S., Bardeau, J., Colas, M., Smarsly, B., Mehdi, A., Ocko, B. M., and Gibaud, A. *Appl. Phys. Lett.* **86**, 113108 (2005). 5
- [69] Lee, B., Yoon, J., Oh, W., Hwang, Y., Heo, K., Jin, K. S., Kim, J., Kim, K., and Ree, M. *Macromolecules* **38**, 3395 (2005).
- [70] Ito, K. O. Y. and Kawamura, S. *Appl. Phys. Lett.* **82**, 544 (2003).
- [71] Wu, W., Wallace, W. E., Lin, E. K., Lynn, G. W., Glinka, C. J., Ryan, E. T., and Ho, H. *J. Appl. Phys.* **87**, 1193 (2000). 5

- [72] Sinturel, C., Vayer, M., Morris, M., and Hillmyer, M. A. *Macromolecules* **46**, 5399 (2013). [5](#), [96](#)
- [73] Vayer, M., Nguyen, T. H., Grosso, D., Boissiere, C., Hillmyer, M. A., and Sinturel, C. *Macromolecules* **44**, 8892 (2011). [5](#), [96](#)
- [74] Silverstein, M. S., Shach-Caplan, M., Bauer, B. J., Hedden, R. C., and Lee, H. J. *Macromolecules* **38**, 4301 (2005).
- [75] Kim, J. S., Kim, H. C., Lee, B., and Ree, M. *Polymer* **46**, 7394 (2005).
- [76] Oka, T., Ito, K., Muramatsu, M., Ohdaira, T., Suzuki, R., and Kobayashi, Y. *J. Phys. Chem. B* **110**, 20172 (2006).
- [77] Krohm, F., Didzoleit, H., Schulze, M., Dietz, C., Stark, R. W., Hess, C., Stühn, B., and Brunsen, A. *Langmuir* **30**, 369 (2014). [5](#)
- [78] Song, L., Feng, D., Fredin, N. J., Yager, K. G., Jones, R. L., Wu, Q., Zhao, D., and Vogt, B. D. *ACS Nano* **4**, 189 (2010). [5](#)
- [79] Chavez, V. L., Song, L., Barua, S., Li, X., Wu, Q., Zhao, D., Rege, K., and Vogt, B. D. *Acta Biomater.* **6**, 3035 (2010).
- [80] Sanchez, C., Boissière, C., Grosso, D., Laberty, C., and Nicole, L. *Chem. Mater.* **20**, 682 (2008). [6](#)
- [81] Sinturel, C., Grosso, D., Boudot, M., Amenitsch, H., Hillmyer, M. A., Pineau, A., and Vayer, M. *Appl. Mater. Interfaces* **6**, 12146 (2014).
- [82] Song, L., Feng, D., Lee, H., Wang, C., Wu, Q., Zhao, D., and D., V. B. *J. Phys. Chem. C* **114**, 9618 (2010). [5](#)
- [83] Baklanov, M. R., Mogilnikov, K. P., Polovinkin, V. G., and Dultsev, F. N. *J. Vac. Sci. Technol. B* **18**, 1385 (2000). [5](#), [6](#), [96](#)
- [84] Krause, K. M., Vick, D. W., Malac, M., and Brett, M. J. *Langmuir* **26**, 17558 (2010). [5](#), [60](#)

- [85] Buzea, C., Beydaghyan, G., Elliott, C., and Robbie, K. *Nanotechnology* **16**, 1986 (2005).
- [86] Kaminska, K., Amassian, A., Martinu, L., and Robbie, K. *J. Appl. Phys.* **97**, 013511 (2005). [5](#)
- [87] Baklanov, M. R. and Mogilnikov, K. P. *Microelectron. Eng.* **64**, 335 (2002). [6](#), [96](#)
- [88] Krause, K., Thommes, M., and Brett, M. J. *Microporous Mesoporous Mater.* **143**, 166 (2011). [6](#)
- [89] Hodgkinson, I. and Wu, Q. H. *Appl. Opt.* **38**, 3621 (1999). [6](#)
- [90] Popta, A. C. V., Sit, J. C., and Brett, M. J. *Appl. Opt.* **43**, 3632 (2004).
- [91] Hawkeye, M. M. and Brett, M. J. *J. Appl. Phys.* **100**, 044322 (2006). [6](#)
- [92] Kesapragada, S. V., Victor, P., Nalamasu, O., and Gall, D. *Nano Lett.* **6**, 854 (2006). [6](#)
- [93] Fernando, S., Elias, A. L., and Brett, M. J. *J. Mater. Res.* **21**, 1101 (2006). [6](#)
- [94] Gospodyn, J. and Sit, J. C. *Opt. Mater.* **29**, 318 (2006). [6](#), [7](#), [38](#)
- [95] Schmidt, D., Kjerstad, A. C., Hofmann, T., Skomski, R., Schubert, E., and Schubert, M. *J. Appl. Phys.* **105**, 113508 (2009). [31](#), [37](#), [53](#)
- [96] Nerbø, I. S., Roy, S. L., Foldyna, M., Kildemo, M., and Søndergård, E. *J. Appl. Phys.* **108**, 014307 (2008). [6](#), [7](#), [38](#)
- [97] Schmidt, D., Müller, C., Hofmann, T., Inganäs, O., Arwin, H., Schubert, E., and Schubert, M. *Thin Solid Films* **519**, 2645 (2011). [6](#), [7](#), [16](#)
- [98] May, R. A., Flaherty, D. W., Mullins, C. B., and Stevenson, K. J. *J. Phys. Chem. Lett.* **1**, 1264 (2010). [6](#)

- [99] Schmidt, D., Booso, B., Hofmann, T., Schubert, E., Sarangan, A., and Schubert, M. *Appl. Phys. Lett.* **94**, 011914 (2009). [7](#), [31](#), [37](#)
- [100] Schmidt, D., Booso, B., Hofmann, T., Schubert, E., Sarangan, A., and Schubert, M. *Opt. Lett.* **34**, 992 (2009). [7](#), [37](#)
- [101] Schmidt, D., Schubert, E., and Schubert, M. *Appl. Phys. Lett.* **100**, 011912 (2012). [7](#), [38](#), [39](#)
- [102] Hofmann, T., Schmidt, D., Boosalis, A., Kühne, P., Skomski, R., Herzinger, C. M., Woollam, J. A., Schubert, M., and Schubert, E. *Appl. Phys. Lett.* **99**, 081903 (2011). [7](#), [38](#), [39](#)
- [103] Beydaghyan, G., Buzea, C., Cui, Y., Elliott, C., and Robbie, K. *Appl. Phys. Lett.* **87**, 153103 (2005).
- [104] Hofmann, T., Schmidt, D., Boosalis, A., Kühne, P., Herzinger, C. M., Woollam, J. A., Schubert, E., and Schubert, M. *Mater. Res. Soc. Symp. Proc.* **1409**, CC1331 (2012). [7](#)
- [105] Rodenhausen, K. B., Schmidt, D., Kasputis, T., Pannier, A. K., Schubert, E., and Schubert, M. *Opt. Express* **20**, 5419 (2012). [7](#), [38](#)
- [106] Lakthakia, A. and Messier, R. *Sculptured Thin Films*. SPIE Press, Bellingham, (2004). [12](#)
- [107] Losurdo, M. and Hingerl, K. *Ellipsometry at the Nanoscale*. Springer, Berlin, (2013). [12](#), [35](#), [36](#), [41](#), [42](#), [43](#), [89](#)
- [108] Summers, M. A. and Brett, M. J. *Nanotechnology* **19**, 415203 (2008). [12](#)
- [109] Nieuwenhuizen, J. M. and Haanstra, H. B. *Philips Tech. Rev.* **27**, 87 (1966). [13](#)
- [110] Tait, R. N., Smy, T., and Brett, M. J. *Thin Solid Films* **226**, 196 (1993).
- [111] Meakin, P. *Phys. Rev. A* **38**, 994 (1988).

- [112] Lichter, S. and Chen, J. *Phys. Rev. Lett.* **56**, 1396 (1986).
- [113] Hodgkinson, I., Wu, Q. H., and Hazel, J. *Appl. Opt.* **37**, 2653 (1998).
- [114] Paritosh and Srolovitz, D. J. *J. Appl. Phys.* **102**, 123109 (2013). [13](#)
- [115] Schmidt, D. *Generalized Ellipsometry on Sculptured Thin Films made by Glancing Angle Deposition*. PhD thesis, University of Nebraska-Lincoln, Department of Electrical Engineering, (2010). [13](#), [14](#), [15](#), [38](#)
- [116] Robbie, K., Beydaghyan, G., Brown, T., Dean, C., Adams, J., and Buzea, C. *Rev. Sci. Instrum.* **75**, 1089 (2004). [15](#)
- [117] Martín, J. and Mijangos, C. *Langmuir* **25**, 1181 (2009). [17](#)
- [118] Zheng, R. K., Chen, H. L., and Choy, C. L. *Nanotechnology* **16**, 1928 (2005). [17](#)
- [119] Walsh, C. B. and Franses, E. I. *Thin Solid Films* **429**, 71 (2003). [17](#)
- [120] Zhang, F., Di, C., Berdunov, N., Hu, Y., Hu, Y., Gao, X., Meng, Q., Siringhaus, H., and Zhu, D. *Adv. Mater.* **25**, 1401 (2013). [17](#)
- [121] Quirk, M. and Serda, J. *Semiconductor Manufacturing Technology*. Prentice Hall, Upper Saddle River, (2001). [18](#)
- [122] Kim, K. S., Zhao, Y., Jang, H., Lee, S. Y., Kim, J. M., Kim, K. S., Ahn, J., Kim, P., Choi, J., and Hong, B. H. *Nature* **457**, 706 (2009). [19](#)
- [123] Puurunen, R. L. *J. Appl. Phys.* **97**, 121301 (2005). [19](#)
- [124] Miikkulainen, V., Leskelä, M., Ritala, M., and Puurunen, R. L. *J. Appl. Phys.* **113**, 021301 (2013). [19](#), [20](#)
- [125] Zhou, W. and Wang, Z. *Scanning Microscopy for Nanotechnology*. Springer, New York, (2006). [22](#), [23](#), [27](#)

- [126] Goldstein, J., Newbury, D., Joy, D., Lyman, C., Echlin, P., Lifshin, E., Sawyer, L., and Michael, J. *Scanning Electron Microscopy and X-Ray Microanalysis*. Springer, New York, (2003). [23](#), [25](#), [26](#), [27](#), [79](#)
- [127] Grubb, D. T. *J. Mater. Sci.* **9**, 1715 (1974). [23](#)
- [128] Reimer, L. and Schmidt, A. *Scanning* **7**, 47 (1985). [23](#)
- [129] Fujiwara, H. *Spectroscopic Ellipsometry Principles and Applications*. John Wiley and Sons Ltd, West Sussex, England, (2007). [27](#), [28](#), [29](#), [90](#)
- [130] Tompkins, H. G. and Irene, E. A. *Handbook of Ellipsometry*. William Andrew Publishing, Norwich, (2005). [29](#), [30](#), [31](#), [36](#), [47](#)
- [131] Schubert, M. *Infrared Ellipsometry on Semiconductor Layer Structures: Phonons, Plasmons, and Polaritons*. Springer, Berlin, (2004). [30](#), [32](#), [33](#), [34](#), [40](#), [41](#), [42](#), [89](#)
- [132] Schubert, M. *Ann. Phys.* **15**, 480 (2006). [30](#)
- [133] de Graef, M. and McHenry, M. E. *Structure of Materials: An Introduction to Crystallography, Diffraction, and Symmetry*. Cambridge University Press, Cambridge, (2007). [35](#)
- [134] Schmidt, D., Schmidt, D., Wang, H., Schubert, E., and Schubert, M. *Appl. Phys. Lett.* **103**, 111906 (2013). [37](#), [38](#), [88](#)
- [135] Schmidt, D. and Schubert, M. *J. Appl. Phys.* **114**, 083510 (2013). [37](#), [38](#), [39](#), [42](#), [50](#), [86](#), [90](#)
- [136] Mackay, T. G. and Lakhtakia, A. *J. Nanophoton.* **6**, 069501 (2012). [39](#)
- [137] Press, W., Flannery, B., Teukolsky, S., and Vetterling, W. *Numerical Recipes: The Art of Scientific Computing*. Cambridge University Press, Cambridge, (1988). [41](#)
- [138] Jellison, G. E. *Thin Solid Films* **33**, 313 (1998). [42](#)

- [139] Herzinger, C. M., Snyder, P. G., Johs, B., and Woollam, J. A. *J. Appl. Phys.* **77**, 1715 (1994).
- [140] Herzinger, C. M., Yao, H., Snyder, P. G., Celii, F. G., Kao, Y. C., Ohs, B., and Woollam, J. A. *J. Appl. Phys.* **77**, 4677 (1995). [42](#)
- [141] Schmidt, D., Schubert, E., and Schubert, M. *Phys. Stat. Sol. (a)* **205**, 748 (2008). [53](#)
- [142] Francis, L. F., McCormick, A. V., and Vaessen, D. M. *J. Mater. Sci.* **37**, 4717 (2002). [61](#)
- [143] Hövel, M., Gompf, B., and Dressel, M. *Phys. Rev. B* **81**, 035402 (2010). [73](#)
- [144] Alonso, M. I., Marcus, I. C., Garriga, M., Goñi, A. R., Jedrzejewski, J., and Balberg, I. *Phys. Rev. B* **82**, 045302 (2010).
- [145] Oates, T. W. H., McKenzie, D. R., and Bilek, M. M. M. *Phys. Rev. B* **70**, 195406 (2010). [73](#)
- [146] Palik, E. D. *Handbook of Optical Constants of Solids*. Academic, Boston, (1991). [76](#)
- [147] Wilson, P. M., Mbah, G. N., Smith, T. G., Schmidt, D., Lai, R. Y., Hofmann, T., and Sinitskii, A. *J. Mater. Chem. C* **2**, 011912 (2014). [79](#), [89](#)
- [148] Harrington, R. F. *Time-harmonic electromagnetic fields*. Wiley-IEEE Press, New York, (2001). [89](#)
- [149] Schmidt, D., Hofmann, T., Craig Herzinger, M., Schubert, E., and Schubert, M. *Appl. Phys. Lett.* **96**, 091906 (2010). [95](#)
- [150] Mok, K., Kovács, G. J., McCord, J., Li, L., Helm, M., and Schmidt, H. *Phys. Rev. B* **84**, 094413 (2011).
- [151] Mok, K., Du, N., and Schmidt, H. *Rev. Sci. Instrum.* **82**, 033112 (2011).

- [152] Schmidt, D., Briley, C., Schubert, E., and Schubert, M. *Appl. Phys. Lett.* **102**, 123109 (2013). [95](#)
- [153] Günes, S., Neugebauer, H., and Sariciftci, N. S. *Chem. Rev.* **107**, 1324 (2007). [96](#)